

A Fictitious Domain Approach to the Direct Numerical Simulation of Incompressible Viscous Flow past Moving Rigid Bodies: Application to Particulate Flow

R. Glowinski,* T. W. Pan,* T. I. Hesla,† D. D. Joseph,† and J. Périaux‡

**Department of Mathematics, University of Houston, Houston, Texas 77204-3476;* †*Aerospace Engineering and Mechanics, University of Minnesota, 107 Ackerman Hall, 110 Union Street, Minneapolis, Minnesota 55455;* and ‡*Dassault Aviation, 1 Rue Charles Blum, Cedex 300, 92552 Saint Cloud, France*

E-mail: roland@math.uh.edu, pan@math.uh.edu, hesla@aem.umn.edu,
joseph@aem.umn.edu, periaux@rascasse.inria.fr

Received December 16, 1999; revised April 26, 2000

In this article we discuss a methodology that allows the direct numerical simulation of incompressible viscous fluid flow past moving rigid bodies. The simulation methods rest essentially on the combination of:

- (a) Lagrange-multiplier-based fictitious domain methods which allow the fluid flow computations to be done in a fixed flow region.
- (b) Finite element approximations of the Navier–Stokes equations occurring in the global model.
- (c) Time discretizations by operator splitting schemes in order to treat optimally the various operators present in the model.

The above methodology is particularly well suited to the direct numerical simulation of particulate flow, such as the flow of mixtures of rigid solid particles and incompressible viscous fluids, possibly non-Newtonian. We conclude this article with the presentation of the results of various numerical experiments, including the simulation of store separation for rigid airfoils and of sedimentation and fluidization phenomena in two and three dimensions. © 2001 Academic Press

Key Words: fictitious domain methods; finite element methods; distributed Lagrange multipliers; Navier–Stokes equations; particulate flow; liquid–solid mixtures; store separation; sedimentation; fluidization; Rayleigh–Taylor instabilities.

1. INTRODUCTION

The main goal of this article is to discuss a methodology well suited to the direct numerical simulation of (possibly non-Newtonian) incompressible viscous flow past moving rigid bodies *when the motion of the bodies is not known in advance* but results from the hydrodynamical coupling and external forces such as gravity and collisions (or near collisions). The methodology discussed here relies on several ingredients, the pivotal ones being:

- A fictitious domain method which allows the flow computation to be done on a fixed space region which contains the moving rigid bodies.
- Lagrange multipliers defined on the regions occupied by the rigid bodies, to match over these regions the fluid flow and rigid body motion velocities.
- A simple but efficient strategy to take into account body/body and body/wall collisions (or near collisions).
- Finite element approximations taking advantage of a global variational formulation (of the virtual power principle type) of the coupled flow–rigid body motion.
- Time discretizations by operator splitting in order to treat separately and (in principle) optimally the various operators associated to the physics and numerics of the computational model.

In this article, the above methods will be applied to the direct numerical simulation of various incompressible Newtonian and non-Newtonian viscous flows past moving rigid bodies in two and three dimensions. These test problems will include the simulation of *store separation* for rigid airfoils and of *sedimentation* and *fluidization* phenomena for small and large ($>10^3$) populations of particles.

An alternative approach to the methodology discussed in this article can be found in Ref. [1], in the present issue of the *Journal of Computational Physics*; it is based on the *Arbitrary Lagrange–Euler* methodology with the flow computed, with a moving mesh on a time-varying region (see [1] and the references therein for details).

The present article reviews (and improves) methods and results discussed in Refs. [2]–[8].

2. MODELING OF THE FLUID–RIGID BODY INTERACTION

Let $\Omega \subset \mathbb{R}^d$ ($d = 2, 3$) be a space region; we suppose that Ω is filled with an *incompressible viscous fluid* of density ρ_f and that it contains J moving rigid bodies B_1, B_2, \dots, B_J (see Fig. 2.1 for a particular case where $d = 2$ and $J = 3$). We denote by \mathbf{n} the unit normal vector on the boundary of $\Omega \setminus \bigcup_{j=1}^J \overline{B_j}$, pointing outward to the flow region. Assuming that the only external force acting on the mixture is *gravity*, then, between *collisions* (assuming that collisions take place), the *fluid flow* is modeled by the *Navier–Stokes equations*

$$\begin{aligned} \rho_f \left[\frac{\partial \mathbf{u}}{\partial t} + (\mathbf{u} \cdot \nabla) \mathbf{u} \right] &= \rho_f \mathbf{g} + \nabla \cdot \boldsymbol{\sigma} \text{ in } \Omega \setminus \bigcup_{j=1}^J \overline{B_j(t)}, \\ \nabla \cdot \mathbf{u} &= 0 \text{ in } \Omega \setminus \bigcup_{j=1}^J \overline{B_j(t)}, \\ \mathbf{u}(\mathbf{x}, 0) &= \mathbf{u}_0(\mathbf{x}), \forall \mathbf{x} \in \Omega \setminus \bigcup_{j=1}^J \overline{B_j(0)}, \text{ with } \nabla \cdot \mathbf{u}_0 = 0, \end{aligned} \quad (2.1)$$

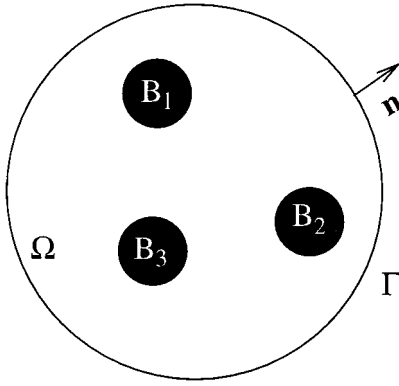


FIG. 2.1. An example of a two-dimensional flow region with three rigid bodies.

to be completed by

$$\mathbf{u} = \mathbf{g}_0 \text{ on } \Gamma \text{ with } \int_{\Gamma} \mathbf{g}_0 \cdot \mathbf{n} \, d\Gamma = 0 \tag{2.2}$$

and by the following *no-slip boundary condition* on the boundary ∂B_j of B_j ,

$$\mathbf{u}(\mathbf{x}, t) = \mathbf{V}_j(t) + \omega_j(t) \times \overrightarrow{\mathbf{G}_j(t)\mathbf{x}}, \forall \mathbf{x} \in \partial B_j(t), \tag{2.3}$$

where, in (2.3), \mathbf{V}_j (resp., ω_j) denotes the *velocity of the center of mass* \mathbf{G}_j (resp., the *angular velocity*) of the j th body, for $j = 1, \dots, J$. In (2.1), the *stress-tensor* σ verifies

$$\sigma = \tau - p\mathbf{I}, \tag{2.4}$$

typical situations for τ being

$$\tau = 2\nu\mathbf{D}(\mathbf{u}) = \nu(\nabla\mathbf{u} + \nabla\mathbf{u}^t) \text{ (Newtonian case)}, \tag{2.5}$$

$$\tau \text{ is a nonlinear function of } \nabla\mathbf{u} \text{ (non-Newtonian case)}. \tag{2.6}$$

The motion of the rigid bodies is modeled by the *Newton–Euler* equations

$$\begin{aligned} M_j \frac{d\mathbf{V}_j}{dt} &= M_j \mathbf{g} + \mathbf{F}_j, \\ \mathbf{I}_j \frac{d\omega_j}{dt} + \omega_j \times \mathbf{I}_j \omega_j &= \mathbf{T}_j, \end{aligned} \tag{2.7}$$

for $j = 1, \dots, J$, where in (2.7),

- M_j is the *mass* of the j th rigid body,
- \mathbf{I}_j is the *inertia tensor* of the j th rigid body,
- \mathbf{F}_j is the resultant of the *hydrodynamical forces* acting on the j th body, i.e.,

$$\mathbf{F}_j = (-1) \int_{\partial B_j} \sigma \mathbf{n} \, d(\partial B_j), \tag{2.8}$$

- \mathbf{T}_j is the torque at \mathbf{G}_j of the hydrodynamical forces acting on the j th body, i.e.,

$$\mathbf{T}_j = (-1) \int_{\partial B_j} \overrightarrow{\mathbf{G}_j\mathbf{x}} \times \sigma \mathbf{n} \, d(\partial B_j), \tag{2.9}$$

- and we have

$$\frac{d\mathbf{G}_j}{dt} = \mathbf{V}_j. \tag{2.10}$$

Equations (2.7) to (2.10) have to be completed by the following *initial conditions*:

$$B_j(0) = B_{0j}, \quad \mathbf{G}_j(0) = \mathbf{G}_{0j}, \quad \mathbf{V}_j(0) = \mathbf{V}_{0j}, \quad \boldsymbol{\omega}_j(0) = \boldsymbol{\omega}_{0j}, \quad \forall j = 1, \dots, J. \tag{2.11}$$

Remark 2.1. If B_j is made of a *homogeneous material* of density ρ_j , we have

$$M_j = \rho_j \int_{B_j} d\mathbf{x}, \quad \mathbf{I}_j = \begin{pmatrix} I_{11,j} & -I_{12,j} & -I_{13,j} \\ -I_{12,j} & I_{22,j} & -I_{23,j} \\ -I_{13,j} & -I_{23,j} & I_{33,j} \end{pmatrix}, \tag{2.12}$$

where, in (2.12), $d\mathbf{x} = dx_1 dx_2 dx_3$ and

$$\begin{aligned} I_{11,j} &= \rho_j \int_{B_j} (x_2^2 + x_3^2) d\mathbf{x}, & I_{22,j} &= \rho_j \int_{B_j} (x_3^2 + x_1^2) d\mathbf{x}, & I_{33,j} &= \rho_j \int_{B_j} (x_1^2 + x_2^2) d\mathbf{x}, \\ I_{12,j} &= \rho_j \int_{B_j} x_1 x_2 d\mathbf{x}, & I_{23,j} &= \rho_j \int_{B_j} x_2 x_3 d\mathbf{x}, & I_{13,j} &= \rho_j \int_{B_j} x_1 x_3 d\mathbf{x}. \end{aligned}$$

Remark 2.2. If the flow–rigid body motion is two-dimensional, or if B_j is a spherical body made of a *homogeneous material*, then the nonlinear term $\boldsymbol{\omega}_j \times \mathbf{I}_j \boldsymbol{\omega}_j$ vanishes in (2.7).

Remark 2.3. Suppose that the rigid bodies do not touch at $t = 0$; then it has been shown by B. Desjardins and M. Esteban (Ref. [9]) that the system of equations modeling the flow of the above fluid–rigid body mixture has a (weak) solution on the time interval $[0, t_*)$, $t_*(> 0)$ depending on the initial conditions; uniqueness is an open problem.

3. A GLOBAL VARIATIONAL FORMULATION OF THE FLUID–SOLID INTERACTION VIA THE VIRTUAL POWER PRINCIPLE

We suppose, in this section, that the fluid is *Newtonian* of viscosity ν . Let us denote by $B(t)$ the space region occupied at time t by the rigid bodies; we have thus $B(t) = \bigcup_{j=1}^J B_j(t)$. To obtain a *variational formulation* for the system of equations described in Section 2, we introduce the following *functional space of compatible test functions*:

$$\begin{aligned} W_0(t) &= \{ \{\mathbf{v}, \mathbf{Y}, \boldsymbol{\theta}\} \mid \mathbf{v} \in (H^1(\Omega \setminus \overline{B(t)}))^d, \quad \mathbf{v} = \mathbf{0} \text{ on } \Gamma, \\ \mathbf{Y} &= \{\mathbf{Y}_j\}_{j=1}^J, \quad \boldsymbol{\theta} = \{\boldsymbol{\theta}_j\}_{j=1}^J, \quad \text{with } \mathbf{Y}_j \in \mathbb{R}^d, \boldsymbol{\theta}_j \in \mathbb{R}^3, \\ \mathbf{v}(\mathbf{x}, t) &= \mathbf{Y}_j + \boldsymbol{\theta}_j \times \overrightarrow{\mathbf{G}_j(t)\mathbf{x}} \text{ on } \partial B_j(t), \quad \forall j = 1, \dots, J \}. \end{aligned} \tag{3.1}$$

In (3.1) we have $\boldsymbol{\theta}_j = \{0, 0, \theta_j\}$ if $d = 2$.

Applying the *virtual power principle* to the *whole mixture* (i.e., to the fluid *and* the rigid bodies) yields the *global variational formulation*

$$\begin{aligned} & \rho_f \int_{\Omega \setminus \overline{B(t)}} \left[\frac{\partial \mathbf{u}}{\partial t} + (\mathbf{u} \cdot \nabla) \mathbf{u} \right] \cdot \mathbf{v} \, d\mathbf{x} + 2\nu \int_{\Omega \setminus \overline{B(t)}} \mathbf{D}(\mathbf{u}) : \mathbf{D}(\mathbf{v}) \, d\mathbf{x} \\ & - \int_{\Omega \setminus \overline{B(t)}} p \nabla \cdot \mathbf{v} \, d\mathbf{x} + \sum_{j=1}^J M_j \dot{\mathbf{V}}_j \cdot \mathbf{Y}_j + \sum_{j=1}^J (\mathbf{I}_j \dot{\boldsymbol{\omega}}_j + \boldsymbol{\omega}_j \times \mathbf{I}_j \boldsymbol{\omega}_j) \cdot \boldsymbol{\theta}_j \end{aligned} \quad (3.2)$$

$$= \rho_f \int_{\Omega \setminus \overline{B(t)}} \mathbf{g} \cdot \mathbf{v} \, d\mathbf{x} + \sum_{j=1}^J M_j \mathbf{g} \cdot \mathbf{Y}_j, \quad \forall \{\mathbf{v}, \mathbf{Y}, \boldsymbol{\theta}\} \in W_0(t),$$

$$\int_{\Omega \setminus \overline{B(t)}} q \nabla \cdot \mathbf{u}(t) \, d\mathbf{x} = 0, \quad \forall q \in L^2(\Omega \setminus \overline{B(t)}), \quad (3.3)$$

$$\mathbf{u}(t) = \mathbf{g}_0(t) \text{ on } \Gamma, \quad (3.4)$$

$$\mathbf{u}(\mathbf{x}, t) = \mathbf{V}_j(t) + \boldsymbol{\omega}_j(t) \times \overrightarrow{\mathbf{G}_j(t)\mathbf{x}}, \quad \forall \mathbf{x} \in \partial B_j(t), \forall j = 1, \dots, J, \quad (3.5)$$

$$\frac{d\mathbf{G}_j}{dt} = \mathbf{V}_j, \quad (3.6)$$

to be completed by the *initial conditions*

$$\mathbf{u}(\mathbf{x}, 0) = \mathbf{u}_0(\mathbf{x}), \quad \forall \mathbf{x} \in \Omega \setminus \overline{B(0)}, \quad (3.7)$$

$$B_j(0) = B_{0j}, \quad \mathbf{G}_j(0) = \mathbf{G}_{0j}, \quad \mathbf{V}_j(0) = \mathbf{V}_{0j}, \quad \boldsymbol{\omega}_j(0) = \boldsymbol{\omega}_{0j}, \quad \forall j = 1, \dots, J. \quad (3.8)$$

In relations (3.2) to (3.8):

- We have denoted functions such as $\mathbf{x} \rightarrow \varphi(\mathbf{x}, t)$ by $\varphi(t)$.
- We have used the following notation:

$$\mathbf{a} \cdot \mathbf{b} = \sum_{k=1}^d a_k b_k, \quad \forall \mathbf{a} = \{a_k\}_{k=1}^d, \mathbf{b} = \{b_k\}_{k=1}^d,$$

$$\mathbf{A} : \mathbf{B} = \sum_{k=1}^d \sum_{l=1}^d a_{kl} b_{kl}, \quad \forall \mathbf{A} = (a_{kl})_{1 \leq k, l \leq d}, \mathbf{B} = (b_{kl})_{1 \leq k, l \leq d}.$$

- It is reasonable to assume that $\mathbf{u}(t) \in (H^1(\Omega \setminus \overline{B(t)}))^d$ and $p(t) \in L^2(\Omega \setminus \overline{B(t)})$.
- We have $\boldsymbol{\omega}_j(t) = \{0, 0, \omega_j(t)\}$ if $d = 2$.

Formulations such as (3.2)–(3.8) (or closely related ones) have been used by several authors (see, e.g., [1], [10]–[12]) to simulate particulate flow via *arbitrary Lagrange–Euler* (ALE) methods using moving meshes (actually, formulation (3.2)–(3.8) has been used in [9] to prove the existence of a local in time weak solution to problem (2.1)–(2.5), (2.7), (2.11)). Our goal in this article is to discuss an alternative based on *fictitious domain methods* (also called *domain embedding* methods). The main advantage of this new (in the context of particulate flow) approach is the possibility of achieving the flow-related computations on a *fixed* space region, allowing thus the use of a fixed (finite difference or finite element) mesh, which is a significant simplification.

4. A DISTRIBUTED LAGRANGE-MULTIPLIER-BASED FICTITIOUS DOMAIN FORMULATION

In general terms our goal is to find a methodology in which

- (a) a fixed mesh can be used for flow computations,
- (b) the rigid body positions are obtained from the solution of the Newton–Euler equations of motion, and
- (c) The time discretization is done by operator splitting methods in order to treat individually the various operators occurring in the mathematical model.

To achieve such a goal we proceed as follows:

- (i) We fill the rigid bodies with the surrounding fluid.
- (ii) We assume that the fluid inside each body has a rigid body motion.
- (iii) We use (i) and (ii) to modify the variational formulation (3.2)–(3.8).
- (iv) We force the rigid body motion inside each moving body via a Lagrange multiplier defined (distributed) over the body.
- (v) We combine (iii) and (iv) to derive a variational formulation involving Lagrange multipliers to force the rigid body motion inside the moving bodies.

We suppose (for simplicity) that each rigid body B_j is made of a *homogeneous material* of density ρ_j ; then, taking into account the fact that any rigid body motion velocity field \mathbf{v} verifies $\nabla \cdot \mathbf{v} = 0$ and $\mathbf{D}(\mathbf{v}) = \mathbf{0}$, steps (i) to (iii) yield the following variant of formulation (3.2)–(3.8):

For a.e. $t > 0$, find $\mathbf{u}(t)$, $p(t)$, $\{\mathbf{V}_j(t), \mathbf{G}_j(t), \boldsymbol{\omega}_j(t)\}_{j=1}^J$, such that

$$\begin{aligned} & \rho_f \int_{\Omega} \left[\frac{\partial \mathbf{u}}{\partial t} + (\mathbf{u} \cdot \nabla) \mathbf{u} \right] \cdot \mathbf{v} \, d\mathbf{x} - \int_{\Omega} p \nabla \cdot \mathbf{v} \, d\mathbf{x} + 2\nu \int_{\Omega} \mathbf{D}(\mathbf{u}) : \mathbf{D}(\mathbf{v}) \, d\mathbf{x} \\ & + \sum_{j=1}^J (1 - \rho_f / \rho_j) \left[M_j \frac{d\mathbf{v}_j}{dt} \cdot \mathbf{Y}_j + \left(\mathbf{I}_j \frac{d\boldsymbol{\omega}_j}{dt} + \boldsymbol{\omega}_j \times \mathbf{I}_j \boldsymbol{\omega}_j \right) \cdot \boldsymbol{\theta}_j \right] \end{aligned} \quad (4.1)$$

$$\begin{aligned} & = \rho_f \int_{\Omega} \mathbf{g} \cdot \mathbf{v} \, d\mathbf{x} + \sum_{j=1}^J (1 - \rho_f / \rho_j) M_j \mathbf{g} \cdot \mathbf{Y}_j, \quad \forall \{\mathbf{v}, \mathbf{Y}, \boldsymbol{\theta}\} \in \tilde{W}_0(t), \\ & \int_{\Omega} q \nabla \cdot \mathbf{u} \, d\mathbf{x} = 0, \quad \forall q \in L^2(\Omega), \end{aligned} \quad (4.2)$$

$$\mathbf{u} = \mathbf{g}_0 \text{ on } \Gamma, \quad (4.3)$$

$$\mathbf{u}(\mathbf{x}, t) = \mathbf{V}_j(t) + \boldsymbol{\omega}_j(t) \times \overrightarrow{\mathbf{G}_j(t)\mathbf{x}}, \quad \forall \mathbf{x} \in B_j(t), \forall j = 1, \dots, J, \quad (4.4)$$

$$\frac{d\mathbf{G}_j}{dt} = \mathbf{V}_j, \quad (4.5)$$

$$B_j(0) = B_{0j}, \quad \mathbf{V}_j(0) = \mathbf{V}_{0j}, \quad \boldsymbol{\omega}_j(0) = \boldsymbol{\omega}_{0j}, \quad \mathbf{G}_j(0) = \mathbf{G}_{0j}, \quad \forall j = 1, \dots, J, \quad (4.6)$$

$$\begin{aligned} \mathbf{u}(\mathbf{x}, 0) = \mathbf{u}_0(\mathbf{x}), \quad \forall \mathbf{x} \in \Omega \setminus \bigcup_{j=1}^J \overline{B_{0j}} \quad \text{and} \quad \mathbf{u}(\mathbf{x}, 0) = \mathbf{V}_{0j} + \boldsymbol{\omega}_{0j} \times \overrightarrow{\mathbf{G}_{0j}\mathbf{x}}, \\ \forall \mathbf{x} \in \overline{B_{0j}} \end{aligned} \quad (4.7)$$

with, in relation (4.1), space $\tilde{W}_0(t)$ defined by

$$\begin{aligned} \tilde{W}_0(t) = \{ \{\mathbf{v}, \mathbf{Y}, \boldsymbol{\theta}\} \mid \mathbf{v} \in (H_0^1(\Omega))^d, \quad \mathbf{Y} = \{\mathbf{Y}_j\}_{j=1}^J, \boldsymbol{\theta} = \{\boldsymbol{\theta}_j\}_{j=1}^J, \text{ with } \mathbf{Y}_j \in \mathbb{R}^d, \\ \boldsymbol{\theta}_j \in \mathbb{R}^3, \quad \mathbf{v}(\mathbf{x}, t) = \mathbf{Y}_j + \overrightarrow{\mathbf{G}_j(t)\mathbf{x}} \text{ in } B_j(t), \quad \forall j = 1, \dots, J \}. \end{aligned}$$

Concerning \mathbf{u} and p , it makes sense to assume that $\mathbf{u}(t) \in (H^1(\Omega))^d$ and $p(t) \in L^2(\Omega)$.

In order to relax the *rigid body motion constraint* (4.4), we are going to employ a family $\{\boldsymbol{\lambda}_j\}_{j=1}^J$ of *Lagrange multipliers* so that $\boldsymbol{\lambda}_j(t) \in \Lambda_j(t)$ with

$$\Lambda_j(t) = (H^1(B_j(t)))^d, \quad \forall j = 1, \dots, J. \quad (4.8)$$

We obtain, thus, the following *fictitious domain formulation with Lagrange multipliers*:

For a.e. $t > 0$, find $\mathbf{u}(t)$, $p(t)$, $\{\mathbf{V}_j(t), \mathbf{G}_j(t), \boldsymbol{\omega}_j(t), \boldsymbol{\lambda}_j(t)\}_{j=1}^J$, such that

$$\mathbf{u}(t) \in (H^1(\Omega))^d, \mathbf{u}(t) = \mathbf{g}_0(t) \text{ on } \Gamma, p(t) \in L^2(\Omega), \quad (4.9)$$

$$\mathbf{V}_j(t) \in \mathbb{R}^d, \mathbf{G}_j(t) \in \mathbb{R}^d, \boldsymbol{\omega}_j(t) \in \mathbb{R}^3, \boldsymbol{\lambda}_j(t) \in \Lambda_j(t), \quad \forall j = 1, \dots, J,$$

and

$$\begin{aligned} \rho_f \int_{\Omega} \left[\frac{\partial \mathbf{u}}{\partial t} + (\mathbf{u} \cdot \nabla) \mathbf{u} \right] \cdot \mathbf{v} \, d\mathbf{x} - \int_{\Omega} p \nabla \cdot \mathbf{v} \, d\mathbf{x} + 2\nu \int_{\Omega} \mathbf{D}(\mathbf{u}) : \mathbf{D}(\mathbf{v}) \, d\mathbf{x} \\ - \sum_{j=1}^J \langle \boldsymbol{\lambda}_j, \mathbf{v} - \mathbf{Y}_j - \boldsymbol{\theta}_j \times \overrightarrow{\mathbf{G}_j \mathbf{x}} \rangle_j + \sum_{j=1}^J (1 - \rho_f / \rho_j) M_j \frac{d\mathbf{V}_j}{dt} \cdot \mathbf{Y}_j \end{aligned} \quad (4.10)$$

$$+ \sum_{j=1}^J (1 - \rho_f / \rho_j) \left(\mathbf{I}_j \frac{d\boldsymbol{\omega}_j}{dt} + \boldsymbol{\omega}_j \times \mathbf{I}_j \boldsymbol{\omega}_j \right) \cdot \boldsymbol{\theta}_j = \rho_f \int_{\Omega} \mathbf{g} \cdot \mathbf{v} \, d\mathbf{x}$$

$$+ \sum_{j=1}^J (1 - \rho_f / \rho_j) M_j \mathbf{g} \cdot \mathbf{Y}_j, \quad \forall \mathbf{v} \in (H_0^1(\Omega))^d, \forall \mathbf{Y}_j \in \mathbb{R}^d, \forall \boldsymbol{\theta}_j \in \mathbb{R}^3,$$

$$\int_{\Omega} q \nabla \cdot \mathbf{u} \, d\mathbf{x} = 0, \quad \forall q \in L^2(\Omega), \quad (4.11)$$

$$\langle \boldsymbol{\mu}_j, \mathbf{u}(t) - \mathbf{V}_j(t) - \boldsymbol{\omega}_j(t) \times \overrightarrow{\mathbf{G}_j(t)\mathbf{x}} \rangle_j = 0, \quad \forall \boldsymbol{\mu}_j \in \Lambda_j(t), \forall j = 1, \dots, J, \quad (4.12)$$

$$\frac{d\mathbf{G}_j}{dt} = \mathbf{V}_j, \quad \forall j = 1, \dots, J, \quad (4.13)$$

$$\mathbf{V}_j(0) = \mathbf{V}_{0j}, \quad \mathbf{G}_j(0) = \mathbf{G}_{0j}, \quad \boldsymbol{\omega}_j(0) = \boldsymbol{\omega}_{0j}, \quad B_j(0) = B_{0j}, \quad \forall j = 1, \dots, J, \quad (4.14)$$

$$\mathbf{u}(\mathbf{x}, 0) = \mathbf{u}_0(\mathbf{x}), \quad \forall \mathbf{x} \in \Omega \setminus \bigcup_{j=1}^J \overline{B_{0j}} \quad \text{and} \quad \mathbf{u}(\mathbf{x}, 0) = \mathbf{V}_{0j} + \boldsymbol{\omega}_{0j} \times \overrightarrow{\mathbf{G}_{0j}\mathbf{x}}, \quad \forall \mathbf{x} \in \overline{B_{0j}}. \quad (4.15)$$

The two most natural choices for $\langle \cdot, \cdot \rangle_j$ are defined by

$$\langle \boldsymbol{\mu}, \mathbf{v} \rangle_j = \int_{B_j(t)} (\boldsymbol{\mu} \cdot \mathbf{v} + \delta_j^2 \nabla \boldsymbol{\mu} : \nabla \mathbf{v}) \, d\mathbf{x}, \quad \forall \boldsymbol{\mu} \text{ and } \mathbf{v} \in \Lambda_j(t), \quad (4.16)$$

$$\langle \boldsymbol{\mu}, \mathbf{v} \rangle_j = \int_{B_j(t)} (\boldsymbol{\mu} \cdot \mathbf{v} + \delta_j^2 \mathbf{D}(\boldsymbol{\mu}) : \mathbf{D}(\mathbf{v})) \, d\mathbf{x}, \quad \forall \boldsymbol{\mu} \text{ and } \mathbf{v} \in \Lambda_j(t), \quad (4.17)$$

with δ_j as a *characteristic length* (the diameter of B_j , for example). Other choices are possible, such as

$$\langle \boldsymbol{\mu}, \mathbf{v} \rangle_j = \int_{\partial B_j(t)} \boldsymbol{\mu} \cdot \mathbf{v} \, d(\partial B_j) + \delta_j \int_{B_j(t)} \nabla \boldsymbol{\mu} : \nabla \mathbf{v} \, d\mathbf{x}, \quad \forall \boldsymbol{\mu} \text{ and } \mathbf{v} \in \Lambda_j(t),$$

or

$$\langle \boldsymbol{\mu}, \mathbf{v} \rangle_j = \int_{\partial B_j(t)} \boldsymbol{\mu} \cdot \mathbf{v} \, d(\partial B_j) + \delta_j \int_{B_j(t)} \mathbf{D}(\boldsymbol{\mu}) : \mathbf{D}(\mathbf{v}) \, d\mathbf{x}, \quad \forall \boldsymbol{\mu} \text{ and } \mathbf{v} \in \Lambda_j(t).$$

Remark 4.1. The fictitious domain approach, described above, has clearly many similarities with the *immersed boundary* approach of C. Peskin (see Refs. [13]–[16]). However, the systematic use of *Lagrange multipliers* seems to be new in this context. Another major difference is the fact that in our approach the boundary of the moving rigid bodies does not play the fundamental role it plays in the Peskin’s approach.

Remark 4.2. An approach with some similarities to ours has been developed by S. Schwarzer *et al.* (see Ref. [17]) in a finite difference framework. In the above reference (dedicated to the simulation of particulate flow), the interaction between the rigid body and the fluid is forced via a *penalty method*, instead of the multiplier technique used in the present article; also, minor particle–particle penetration is allowed and no enforcement of the rigid body motion inside the region occupied by the particle is done.

Remark 4.3. In order to force the rigid body motion inside the moving rigid bodies we can use the fact that \mathbf{v} defined over Ω is a rigid body motion velocity field inside each moving rigid body if and only if $\mathbf{D}(\mathbf{v}) = \mathbf{0}$ in $B_j(t)$, $\forall j = 1, \dots, J$; i.e.,

$$\int_{B_j(t)} \mathbf{D}(\mathbf{v}) : \mathbf{D}(\boldsymbol{\mu}) \, d\mathbf{x} = 0, \quad \forall \boldsymbol{\mu} \in \Lambda_j(t), \forall j = 1, \dots, J. \quad (4.18)$$

A computational method based on this approach is discussed in [18].

Remark 4.4. Since, in (4.10), \mathbf{u} is *divergence free* and satisfies Dirichlet boundary conditions on Γ , we have

$$2 \int_{\Omega} \mathbf{D}(\mathbf{u}) : \mathbf{D}(\mathbf{v}) \, d\mathbf{x} = \int_{\Omega} \nabla \mathbf{u} : \nabla \mathbf{v} \, d\mathbf{x}, \quad \forall \mathbf{v} \in (H_0^1(\Omega))^d, \quad (4.19)$$

a substantial simplification indeed, from a *computational point of view*, which is another plus for the fictitious domain approach used here.

Remark 4.5. Using high-energy physics terminology, the multiplier $\boldsymbol{\lambda}_j$ can be viewed as a *gluon* whose role is to force the rigidity inside B_j by matching the velocity fields of two continua. More precisely, the multipliers $\boldsymbol{\lambda}_j$ are mathematical objects of the *mortar* type, very close to those used in *domain decomposition methods* to match local solutions at interfaces or on overlapping regions (see Ref. [19]). Indeed, the $\boldsymbol{\lambda}_j$ in the present article have genuine mortar properties since their role is to force a fluid to behave like a rigid solid inside the space region occupied by the moving bodies.

5. ON THE TREATMENT OF COLLISIONS

In the above sections, we have considered the motion of fluid/rigid body mixtures and have given various mathematical models of this phenomenon, assuming that there was no rigid body/rigid body or boundary/rigid body collisions. Actually, with the mathematical model that we have considered it is not known if collisions can take place in finite time (in fact several scientists strongly believe that lubrication forces prevent these collisions in the case of viscous fluids). However, collisions take place in nature and also in actual numerical simulations if special precautions are not taken. In the particular case of rigid bodies moving in a viscous fluid, under the effect of gravity and hydrodynamical forces, we shall assume that the collisions taking place are *smooth* ones in the sense that if two rigid bodies collide (resp., if a rigid body hits the boundary), the rigid body velocities (resp., the rigid body and boundary velocities) coincide at the points of contact. From the smooth nature of these collisions the only precaution to be taken will be to avoid overlapping of the regions occupied by the rigid bodies. To achieve this goal, we include in the right-hand sides of the *Newton–Euler equations* (2.7) modeling the rigid body motion a *short-range repulsive force*. If we consider the particular case of rigid bodies *circular* (in two-dimensions) or *spherical* (in three-dimensions), and if B_i and B_j are two such rigid bodies, with radii R_i and R_j and centers of mass G_i and G_j , we shall require the repulsion force F_{ij} between B_i and B_j to satisfy the following properties:

- (i) to be parallel to $\overrightarrow{G_i G_j}$,
- (ii) to verify

$$\begin{aligned}
 |\overrightarrow{F_{ij}}| &= 0 & \text{if } d_{ij} \geq R_i + R_j + \rho, \\
 |\overrightarrow{F_{ij}}| &= c_{ij}/\varepsilon & \text{if } d_{ij} = R_i + R_j,
 \end{aligned}
 \tag{5.1}$$

with $d_{ij} = |\overrightarrow{G_i G_j}|$, c_{ij} as a *scaling factor*, and ε as a “*small*” *positive number*, and

- (iii) $|\overrightarrow{F_{ij}}|$ has to behave as in Fig. 5.1 for

$$R_i + R_j \leq d_{ij} \leq R_i + R_j + \rho.$$

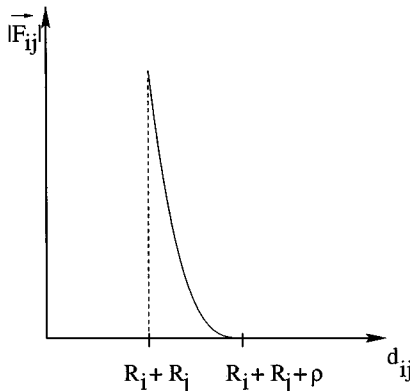


FIG. 5.1. Repulsion force behavior.

Parameter ρ is the *range* of the repulsion force; for the simulations discussed in the following sections, we have taken $\rho \simeq h_\Omega$ (h_Ω is the *space discretization step* used for approximating the *velocity*). Boundary/rigid body collisions can be treated in a similar way.

Remark 5.1. For those readers wondering how to adjust h_Ω and ε , we would like to make the following comments: clearly, the space discretization parameter h_Ω is adjusted so that the finite element approximation can resolve the boundary and shear layers occurring in the flow. Next, it is clear that ρ can be taken of the order of h_Ω . The choice of ε is more subtle; suppose that \vec{F}_{ij} is defined by

$$\vec{F}_{ij} = \frac{c_{ij}}{\varepsilon} \left(\left(\frac{d_{ij} - R_i - R_j - \rho}{\rho} \right)^- \right)^2 \frac{\vec{G}_i \vec{G}_j}{d_{ij}}, \quad (5.2)$$

where, in (5.2), we have used the notation $\xi^- = \max(0, -\xi)$. Denoting, as usual, the dimension of quantity X by $[X]$, ε will be a *dimensional* if and only if c_{ij} has the dimension of a force, i.e., $[c_{ij}] = \text{MLT}^{-2}$.

In order to link ε and ρ , we are going to consider the simple model problem where a material point of mass m is dropped from height $z = H$, without initial velocity, above a rigid obstacle located at $z = 0$ and falls under the effect of gravity. Assuming that the collision is treated as above by *penalty* and a natural choice for the scaling parameter c being mg , the motion of the point is described by

$$\begin{cases} m\ddot{z} - \frac{mg}{\varepsilon\rho^2}((z - \rho)^-)^2 = -mg, \\ z(0) = H, \quad \dot{z}(0) = 0. \end{cases} \quad (5.3)$$

As long as $z \geq \rho$ the equation of motion reduces to $\ddot{z} = -g$, which implies that the material point reaches $z = \rho$ for the first time at $t = t_\rho$, with

$$t_\rho = \sqrt{\frac{2(H - \rho)}{g}}, \quad (5.4)$$

the velocity $\dot{z}(t_\rho)$ being given by

$$\dot{z}(t_\rho) = -\sqrt{2g(H - \rho)}. \quad (5.5)$$

For $z \leq \rho$ the differential equation in (5.3) can also be written as

$$\ddot{z} - \frac{g}{\varepsilon\rho^2}(z - \rho)^2 + g = 0. \quad (5.6)$$

Multiplying both sides of the differential equation (5.6) by \dot{z} , and observing that $dz/dt = d(z - \rho)/dt$, yields

$$\frac{d}{dt} \left[\frac{1}{2} \dot{z}^2 - \frac{g}{3\varepsilon\rho^2} (z - \rho)^3 + g(z - \rho) \right] = 0. \quad (5.7)$$

It follows from (5.5) and (5.7) that as long as $z(t) \leq \rho$, we have

$$\frac{1}{2} \dot{z}(t)^2 - \frac{g}{3\varepsilon\rho^2} (z(t) - \rho)^3 + g(z(t) - \rho) = g(H - \rho). \quad (5.8)$$

The material point reaches its minimal height z_m for t_m such that $\dot{z}_m(t) = 0$. It follows thus from (5.8) that z_m verifies

$$z_m - \rho - (z_m - \rho)^3 / (3\varepsilon\rho^2) = H - \rho. \quad (5.9)$$

Let us denote the *maximal penetration distance* $\rho - z_m$ by δ ; we have then (from (5.9))

$$\delta^3 / (3\varepsilon\rho^2) - \delta = H - \rho. \quad (5.10)$$

We are going to use relation (5.10) to explore several scenarios:

(i) Suppose that $H = \rho$; it follows then from (5.10) that

$$\delta = \sqrt{3\varepsilon\rho}, \quad (5.11)$$

which implies in turn that to have $\delta/\rho \ll 1$ we need to take $\sqrt{\varepsilon} \ll 1$, i.e., δ/ρ “small” implies ε “very small.” Typically, $\delta/\rho \simeq 10^{-2}$ implies $\varepsilon \simeq 10^{-4}$.

(ii) Suppose now that $H \gg \rho$. Since we want $\delta/\rho \ll 1$, it follows from (5.10) that

$$\delta^3 / (3\varepsilon\rho^2) \simeq H,$$

i.e.,

$$\delta/\rho \simeq (3\varepsilon)^{1/3} (H/\rho)^{1/3}. \quad (5.12)$$

Suppose that, for example, $H/\rho = 10^2$ and that we want to take $\delta/\rho \simeq 10^{-2}$; it follows then from (5.11) that we need to take $\varepsilon \simeq 10^{-8}$, i.e., δ/ρ “small” implies ε “very very small.”

Returning to (5.2), let us say that scenario (ii) will be encountered (in some sense) if the fluid surrounding the rigid bodies is *inviscid*, implying possible violent collisions. Scenario (i) corresponds clearly to a soft collision since $\rho \simeq h_\Omega$, and we shall assume that it is the kind of situation which prevails if the fluid is sufficiently viscous and the ratio ρ_j/ρ_f is not too large, i.e., ρ_j/ρ_f of the order of 1, $\forall j = 1, \dots, J$. On the basis of these assumptions we have always taken $\varepsilon \simeq h_\Omega^2$ for the calculations to be presented in Section 8.

Remark 5.2. In order to treat the collisions, we can use repulsion forces derived by truncation of the *Lennard–Jones* potentials from *molecular dynamics* (see, e.g., [20] for these notions from molecular chemistry); this approach is commonly used by physico-chemists to treat collisions in solvents containing “large” particles (whose characteristic sizes are a few micrometers at least).

Remark 5.3. Penalty methods, closely related to those discussed just above, have been (and still are) used by mechanical engineers for the numerical treatment of contact problems. A fundamental reference on these topics is the book by Kikuchi and Oden (Ref. [21]; see also the references therein). The above reference contains comparisons between results obtained by application of the Hertz contact theory and results obtained by penalty methods. According to [21], penalty methods allow the solution of contact problems for which Hertz theory is no longer valid.

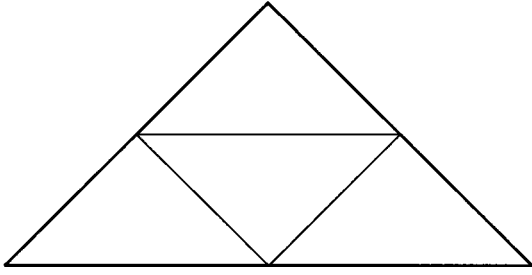


FIG. 6.1. Subdivision of a triangle of \mathcal{T}_{2h} .

6. FINITE ELEMENT APPROXIMATION

For simplicity, we assume that $\Omega \subset \mathbb{R}^2$ (i.e., $d = 2$) and is polygonal; we have then $\omega(t) = \{0, 0, \omega(t)\}$ and $\theta = \{0, 0, \theta\}$ with $\omega(t)$ and $\theta \in \mathbb{R}$. Concerning the *space approximation* of problem (4.9)–(4.15) by a *finite element method*, we shall proceed as follows:

With $h(=h_\Omega)$ as a *space discretization step*, we introduce a finite element triangulation \mathcal{T}_h of $\bar{\Omega}$ and a triangulation \mathcal{T}_{2h} twice coarser (in practice we should construct \mathcal{T}_{2h} first and then \mathcal{T}_h by joining the midpoints of the edges of \mathcal{T}_{2h} , dividing thus each triangle of \mathcal{T}_{2h} into four similar subtriangles, as shown in Fig. 6.1).

We approximate then $(H^1(\Omega))^2$, $(H_0^1(\Omega))^2$, and $L^2(\Omega)$ by the finite dimensional spaces

$$V_h = \{\mathbf{v}_h \mid \mathbf{v}_h \in (C^0(\bar{\Omega}))^2, \quad \mathbf{v}_h|_T \in P_1 \times P_1, \quad \forall T \in \mathcal{T}_h\}, \quad (6.1)$$

$$V_{0h} = \{\mathbf{v}_h \mid \mathbf{v}_h \in V_h, \mathbf{v}_h = \mathbf{0} \text{ on } \Gamma\}, \quad (6.2)$$

and

$$L_h^2 = \{q_h \mid q_h \in C^0(\bar{\Omega}), q_h|_T \in P_1, \forall T \in \mathcal{T}_{2h}\}, \quad (6.3)$$

respectively; in (6.1)–(6.3), P_1 is the space of the polynomials in two variables of degree ≤ 1 . Let $\bar{B}_{jh}(t)$ be a polygonal domain inscribed in $\bar{B}_j(t)$ and let $\mathcal{T}_h^j(t)$ be a finite element triangulation of $\bar{B}_{jh}(t)$, like the one shown in Fig. 6.2, where B_j is a disk.

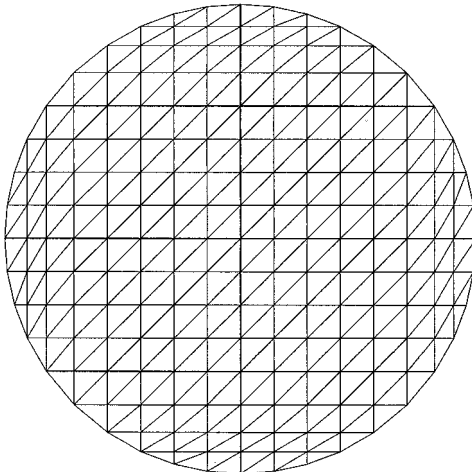


FIG. 6.2. Triangulation of a disk.

A finite dimensional space approximating $\Lambda_j(t)$ is

$$\Lambda_{jh}(t) = \{ \boldsymbol{\mu}_h \mid \boldsymbol{\mu}_h \in (C^0(\overline{B_{jh}(t)}))^2, \boldsymbol{\mu}_h|_T \in P_1 \times P_1, \forall T \in \mathcal{T}_h^j(t) \}. \quad (6.4)$$

An alternative to $\Lambda_{jh}(t)$ defined by (6.4) is as follows: let $\{\mathbf{x}_i\}_{i=1}^{N_j}$ be a set of points from $\overline{B_j(t)}$ which cover $B_j(t)$ (uniformly, for example); we define then

$$\Lambda_{jh}(t) = \left\{ \boldsymbol{\mu}_h \mid \boldsymbol{\mu}_h = \sum_{i=1}^{N_j} \boldsymbol{\mu}_i \delta(\mathbf{x} - \mathbf{x}_i), \boldsymbol{\mu}_i \in \mathbb{R}^2, \forall i = 1, \dots, N_j \right\}, \quad (6.5)$$

where $\delta(\cdot)$ is the Dirac measure at $\mathbf{x} = \mathbf{0}$. Then, instead of the scalar product of $(H^1(B_{jh}(t)))^2$, we shall use $\langle \cdot, \cdot \rangle_{jh}$ defined by

$$\langle \boldsymbol{\mu}_h, \mathbf{v}_h \rangle_{jh} = \sum_{i=1}^{N_j} \boldsymbol{\mu}_i \cdot \mathbf{v}_h(\mathbf{x}_i), \quad \forall \boldsymbol{\mu}_h \in \Lambda_{jh}(t), \mathbf{v}_h \in V_h. \quad (6.6)$$

The approach based on (6.5) and (6.6) makes little sense for the continuous problem, but it is meaningful for the discrete problem; it amounts to forcing the rigid body motion of $B_j(t)$ via a *collocation method*. A similar technique has been used to enforce Dirichlet boundary conditions, by F. Bertrand *et al.* (Ref. [22]).

Remark 6.1. The bilinear form in (6.6) has definitely the flavor of a *discrete* $L^2(B_j(t))$ -scalar product. Let us insist on the fact that taking $\Lambda_j(t) = (L^2(P_j(t)))^2$ and then

$$\langle \boldsymbol{\mu}, \mathbf{v} \rangle_j = \int_{B_j(t)} \boldsymbol{\mu} \cdot \mathbf{v} \, d\mathbf{x}, \quad \forall \boldsymbol{\mu} \text{ and } \mathbf{v} \in \Lambda_j(t)$$

makes no sense for the continuous problem. On the other hand, it makes sense for the finite element variants of (4.9)–(4.15), but do not expect $\lambda_{jh}(t)$ to converge to an L^2 -function as $h \rightarrow 0$ (it will converge to some element of the dual space $((H^1(B_j(t)))^2)'$ of $(H^1(B_j(t)))^2$).

Using the above finite dimensional spaces leads to the following approximation of problem (4.9)–(4.15):

For $t > 0$ find $\mathbf{u}_h(t)$, $p_h(t)$, $\{\mathbf{V}_j(t), \mathbf{G}_{jh}(t), \omega_j(t), \boldsymbol{\lambda}_{jh}(t)\}_{j=1}^J$ such that

$$\begin{cases} \mathbf{u}_h(t) \in V_h, & p_h(t) \in L_h^2, \\ \mathbf{V}_j(t) \in \mathbb{R}^2, & \mathbf{G}_{jh}(t) \in \mathbb{R}^2, \quad \omega_j(t) \in \mathbb{R}, \boldsymbol{\lambda}_{jh}(t) \in \Lambda_{jh}(t), \quad \forall j = 1, \dots, J, \end{cases} \quad (6.7)$$

and

$$\left\{ \begin{aligned} & \rho_f \int_{\Omega} \left[\frac{\partial \mathbf{u}_h}{\partial t} + (\mathbf{u}_h \cdot \nabla) \mathbf{u}_h \right] \cdot \mathbf{v} \, d\mathbf{x} - \int_{\Omega} p_h \nabla \cdot \mathbf{v} \, d\mathbf{x} + 2\nu \int_{\Omega} \mathbf{D}(\mathbf{u}_h) : \mathbf{D}(\mathbf{v}) \, d\mathbf{x} \\ & + \sum_{j=1}^J (1 - \rho_f / \rho_j) M_j \frac{d\mathbf{V}_j}{dt} \cdot \mathbf{Y}_j + \sum_{j=1}^J (1 - \rho_f / \rho_j) I_j \frac{d\omega_j}{dt} \theta_j \\ & - \sum_{j=1}^J \langle \boldsymbol{\lambda}_{jh}, \mathbf{v} - \mathbf{Y}_j - \theta_j \times \overrightarrow{\mathbf{G}_{jh}\mathbf{x}} \rangle_{jh} = \rho_f \int_{\Omega} \mathbf{g} \cdot \mathbf{v} \, d\mathbf{x} \\ & + \sum_{j=1}^J (1 - \rho_f / \rho_j) M_j \mathbf{g} \cdot \mathbf{Y}_j, \quad \forall \mathbf{v} \in V_{0h}, \forall \mathbf{Y}_j \in \mathbb{R}^2, \forall \theta_j \in \mathbb{R}, \end{aligned} \right. \quad (6.8)$$

$$\int_{\Omega} q \nabla \cdot \mathbf{u}_h(t) \, d\mathbf{x} = 0, \quad \forall q \in L_h^2, \tag{6.9}$$

$$\mathbf{u}_h = \mathbf{g}_{0h} \text{ on } \Gamma, \tag{6.10}$$

$$\langle \boldsymbol{\mu}_{jh}, \mathbf{u}_h(t) - \mathbf{V}_j(t) - \overrightarrow{\boldsymbol{\omega}_j(t) \times \mathbf{G}_{jh}(t)\mathbf{x}} \rangle_{jh} = 0, \quad \forall \boldsymbol{\mu}_{jh} \in \Lambda_{jh}(t), \forall j = 1, \dots, J, \tag{6.11}$$

$$\frac{d\mathbf{G}_{jh}}{dt} = \mathbf{V}_j, \quad \forall j = 1, \dots, J, \tag{6.12}$$

$$\mathbf{V}_j(0) = \mathbf{V}_{0j}, \quad \mathbf{G}_{jh}(0) = \mathbf{G}_{0jh}, \quad \omega_j(0) = \omega_{0j}, \quad B_{jh}(0) = B_{0jh}, \tag{6.13}$$

$$\forall j = 1, \dots, J,$$

$$\mathbf{u}_h(\mathbf{x}, 0) = \mathbf{u}_{0h}(\mathbf{x}), \quad \forall \mathbf{x} \in \Omega \setminus \bigcup_{j=1}^J \overline{B_{0jh}}, \quad \mathbf{u}_h(\mathbf{x}, 0) = \mathbf{V}_{0j} + \overrightarrow{\omega_{0j} \times \mathbf{G}_{0jh}\mathbf{x}}, \tag{6.14}$$

$$\forall \mathbf{x} \in \overline{B_{0jh}}.$$

In (6.10), \mathbf{g}_{0h} is an approximation of \mathbf{g}_0 belonging to

$$\gamma V_h = \{ \mathbf{z}_h \mid \mathbf{z}_h \in (C^0(\Gamma))^2, \mathbf{z}_h = \tilde{\mathbf{z}}_h|_{\Gamma} \text{ with } \tilde{\mathbf{z}}_h \in V_h \}$$

and verifying $\int_{\Gamma} \mathbf{g}_{0h} \cdot \mathbf{n} \, d\Gamma = 0$.

Remark 6.2. The discrete pressure in (6.7)–(6.14) is defined within to an additive constant. In order to “fix” the pressure, we shall require it to verify

$$\int_{\Omega} p_h(t) \, d\mathbf{x} = 0, \quad \forall t > 0,$$

i.e., $p_h(t) \in L_{0h}^2$ with L_{0h}^2 defined by

$$L_{0h}^2 = \left\{ q_h \mid q_h \in L_h^2, \int_{\Omega} q_h \, d\mathbf{x} = 0 \right\}.$$

Remark 6.3. From a practical point of view, the semidiscrete model (6.7)–(6.14) is incomplete since we still have to include the virtual power associated to the collision forces. Assuming that the rigid bodies are circular ($d = 2$) or spherical ($d = 3$), we shall add to the right-hand side of Eq. (6.8) the term

$$\sum_{j=1}^J \mathbf{F}_j^r \cdot \mathbf{Y}_j, \tag{6.15}$$

where the repulsion force \mathbf{F}_j^r is defined as in Section 5. If the rigid bodies are noncircular or nonspherical we shall have to take into account the virtual power associated to the torque of the collision forces.

Remark 6.4. Concerning the definition of the multiplier space $\Lambda_{jh}(t)$, several options are possible:

(i) If B_j is rotationally invariant (this will be the case for a circular or a spherical rigid body) we define $\Lambda_{jh}(t)$ from the triangulation $\mathcal{T}_h^j(t)$ obtained from $\mathcal{T}_h^j(0)$ by translation.

(ii) If B_j is not rotationally invariant we can define $\Lambda_{jh}(t)$ from a triangulation $\mathcal{T}_h^j(t)$ rigidly attached to B_j .

(iii) We can also define $\Lambda_{jh}(t)$ from the set of points

$$\Sigma_{jh}(t) = \Sigma_{jh}^v(t) \cup \Sigma_{jh}^\sigma(t), \quad (6.16)$$

where, in (6.16), $\Sigma_{jh}^v(t)$ is the set of vertices of the velocity grid \mathcal{T}_h which are contained in $B_j(t)$, and where $\Sigma_{jh}^\sigma(t)$ is a set of control points located $\partial B_j(t)$. This “hybrid” approach is (relatively) easy to implement and is particularly well suited to those situations where the boundary ∂B_j has corners or edges.

Remark 6.5. In relation (6.8), we can replace $2 \int_{\Omega} \mathbf{D}(\mathbf{u}_h) : \mathbf{D}(\mathbf{v}) \, d\mathbf{x}$ by $\int_{\Omega} \nabla \mathbf{u}_h : \nabla \mathbf{v} \, d\mathbf{x}$, by taking Remark 4.4 into account.

Remark 6.6. Let h_Ω (resp., h_j) be the mesh size associated to the velocity mesh \mathcal{T}_h (resp., to the rigid body mesh \mathcal{T}_h^j); then a relation such as

$$h_\Omega < \chi_j h_j < h_j < 2h_\Omega, \quad (6.17)$$

with $0 < \chi_j < 1$, seems to be needed, from a theoretical point of view, in order to satisfy some kind of *stability condition* of the *Brezzi–Babuska* type (for generalities on the approximation of mixed variational problems, such as (4.9)–(4.15), involving *Lagrange multipliers*, see, for example, the publications by F. Brezzi and M. Fortin (Ref. [23]) and J. E. Roberts and J. M. Thomas (Ref. [24])), actually, taking $h_j = h_\Omega$ seems to work fine in practice.

Remark 6.7. In order to avoid the solution at each time step of complicated *triangulation intersection problems*, we advocate the use of

$$\langle \lambda_{jh}, \Pi_j \mathbf{v} - \mathbf{Y}_j - \boldsymbol{\theta}_j \times \overrightarrow{\mathbf{G}_{jh}(t)\mathbf{x}}_{jh} \rangle \quad (6.18)$$

(resp.,

$$\langle \mu_{jh}, \Pi_j \mathbf{u}_h(t) - \mathbf{V}_j(t) - \boldsymbol{\omega}_j(t) \times \overrightarrow{\mathbf{G}_{jh}(t)\mathbf{x}}_{jh} \rangle \quad (6.19)$$

in (6.8) (resp., (6.11)), instead of

$$\langle \lambda_{jh}, \mathbf{v} - \mathbf{Y}_j - \boldsymbol{\theta}_j \times \overrightarrow{\mathbf{G}_{jh}(t)\mathbf{x}}_{jh} \rangle \quad (6.20)$$

(resp.,

$$\langle \mu_{jh}, \mathbf{u}_h(t) - \mathbf{V}_j(t) - \boldsymbol{\omega}_j(t) \times \overrightarrow{\mathbf{G}_{jh}(t)\mathbf{x}}_{jh} \rangle,$$

where, in (6.18) and (6.19), $\Pi_j : (C^0(\bar{\Omega}))^2 \rightarrow \Lambda_{jh}(t)$ is the *piecewise linear interpolation operator* which to each function \mathbf{w} belonging to $(C^0(\bar{\Omega}))^2$ associates the unique element of $\Lambda_{jh}(t)$ defined from the values taken by \mathbf{w} at the vertices of $\mathcal{T}_h^j(t)$.

Remark 6.8. In general, the function $\mathbf{u}(t)$ has no more than the $(H^{3/2}(\Omega))^2$ -regularity. This low regularity implies that we can not expect more than $O(h^{3/2})$ for the approximation error $\|\mathbf{u}_h(t) - \mathbf{u}(t)\|_{(L^2(\Omega))^2}$ and $O(h^{1/2})$ for the approximation error $|\mathbf{u}_h(t) - \mathbf{u}(t)|_{(H^1(\Omega))^2}$ (see Ref. [25]).

7. TIME DISCRETIZATION BY OPERATOR SPLITTING

7.1. Generalities

Following A. Chorin (Refs. [26]–[28]), most “modern” Navier–Stokes solvers are based on *operator splitting* schemes (see, e.g., Refs. [29], [30]) in order to force the incompressibility condition via a Stokes solver or a L^2 -projection method. This approach still applies to the initial value problem (6.7)–(6.14), which contains four numerical difficulties to each of which can be associated a specific operator, namely,

- (a) the incompressibility condition and the related unknown pressure,
- (b) an advection–diffusion term,
- (c) the rigid-body motion of $B_j(t)$ and the related multiplier $\lambda_j(t)$, and
- (d) the collision terms \mathbf{F}_j^r .

The operators in (a) and (c) are essentially *projection operators*. From an abstract point of view, problem (6.7)–(6.14) is a particular case of the class of initial value problems

$$\frac{d\varphi}{dt} + \sum_{i=1}^4 A_i(\varphi, t) = f, \quad \varphi(0) = \varphi_0, \quad (7.1)$$

where the operators A_i can be *multivalued*. Among the many operator-splitting methods which can be employed to solve problem (7.1) we advocate (following, e.g., [31]) the very simple one below; it is only *first-order accurate*, but its low-order accuracy is compensated by good stability and robustness properties. Actually, this scheme can be made *second-order accurate by symmetrization* (see, e.g., [32]–[34] for the application of *symmetrized splitting schemes* to the solution of the Navier–Stokes equations).

A fractional step scheme à la Marchuk–Yanenko. With $\Delta t (>0)$ as a *time discretization step*, applying the *Marchuk–Yanenko scheme* to the initial value problem (7.1) leads to

$$\varphi^0 = \varphi_0, \quad (7.2)$$

and for $n \geq 0$, compute φ^{n+1} from φ^n via

$$\frac{\varphi^{n+i/4} - \varphi^{n+(i-1)/4}}{\Delta t} + A_i(\varphi^{n+i/4}, (n+1)\Delta t) = f_i^{n+1}, \quad (7.3)$$

for $i = 1, 2, 3, 4$ with $\sum_{i=1}^4 f_i^{n+1} = f^{n+1}$.

Remark 7.1. Recently, we have introduced a five-operator decomposition obtained by treating separately *diffusion* and *advection*. Some of the numerical results presented in this article have been obtained with this new approach, which is briefly discussed in Section 7.3 (see Remark 7.2).

7.2. Application of the Marchuk–Yanenko Scheme to the Solution of Problem (6.7)–(6.14)

Applying scheme (7.2), (7.3) to problem (6.7)–(6.14), we obtain (after inclusion of the collision terms and dropping some of the subscripts h)

$$\mathbf{u}^0 = \mathbf{u}_{0h}, \{ \mathbf{V}_j^0 \}_{j=1}^J, \{ \omega_j^0 \}_{j=1}^J, \{ \mathbf{B}_j^0 \}_{j=1}^J, \text{ and } \mathbf{G}^0 = \{ \mathbf{G}_j^0 \}_{j=1}^J \text{ are given.} \quad (7.4)$$

For $n \geq 0$, knowing \mathbf{u}^n , $\{ \mathbf{V}_j^n \}_{j=1}^J$, $\{ \omega_j^n \}_{j=1}^J$, $\{ \mathbf{B}_j^n \}_{j=1}^J$, and $\mathbf{G}^n = \{ \mathbf{G}_j^n \}_{j=1}^J$, we compute $\mathbf{u}^{n+1/4}$, $p^{n+1/4}$ via the solution of

$$\begin{cases} \rho_f \int_{\Omega} \frac{\mathbf{u}^{n+1/4} - \mathbf{u}^n}{\Delta t} \cdot \mathbf{v} \, d\mathbf{x} - \int_{\Omega} p^{n+1/4} \nabla \cdot \mathbf{v} \, d\mathbf{x} = 0, & \forall \mathbf{v} \in V_{0h}, \\ \int_{\Omega} q \nabla \cdot \mathbf{u}^{n+1/4} \, d\mathbf{x} = 0, & \forall q \in L_h^2, \\ \mathbf{u}^{n+1/4} \in V_h, \quad \mathbf{u}^{n+1/4} = \mathbf{g}_{0h}^{n+1} \text{ on } \Gamma, & p^{n+1/4} \in L_{0h}^2. \end{cases} \quad (7.5)$$

Next, we compute $\mathbf{u}^{n+2/4}$ via the solution of

$$\begin{cases} \rho_f \int_{\Omega} \frac{\mathbf{u}^{n+2/4} - \mathbf{u}^{n+1/4}}{\Delta t} \cdot \mathbf{v} \, d\mathbf{x} + \nu \int_{\Omega} \nabla \mathbf{u}^{n+2/4} : \nabla \mathbf{v} \, d\mathbf{x} \\ + \rho_f \int_{\Omega} (\mathbf{u}^{n+1/4} \cdot \nabla) \mathbf{u}^{n+2/4} \cdot \mathbf{v} \, d\mathbf{x} = \rho_f \int_{\Omega} \mathbf{g} \cdot \mathbf{v} \, d\mathbf{x}, & \forall \mathbf{v} \in V_{0h}, \\ \mathbf{u}^{n+2/4} \in V_h, \mathbf{u}^{n+2/4} = \mathbf{g}_{0h}^{n+1} \text{ on } \Gamma, \end{cases} \quad (7.6)$$

and then, predict the position and the translation velocity of the center of mass as follows, for $j = 1, \dots, J$:

Take $\mathbf{V}_j^{n+2/4,0} = \mathbf{V}_j^n$ and $\mathbf{G}_j^{n+2/4,0} = \mathbf{G}_j^n$; then predict the new position and translation velocity of B_j via the following subcyclng (with the local time step $\Delta t/N$) and predicting–correcting technique:

For $k = 1, \dots, N$, compute

$$\begin{cases} \hat{\mathbf{V}}_j^{n+2/4,k} = \mathbf{V}_j^{n+2/4,k-1} + (\Delta t/N) \mathbf{g} \\ + (\Delta t/2N)(1 - \rho_f/\rho_j)^{-1} M_j^{-1} \mathbf{F}_j^r(\mathbf{G}^{n+2/4,k-1}), \end{cases} \quad (7.7)$$

$$\hat{\mathbf{G}}_j^{n+2/4,k} = \mathbf{G}_j^{n+2/4,k-1} + (\Delta t/4N)(\hat{\mathbf{V}}_j^{n+2/4,k} + \mathbf{V}_j^{n+2/4,k-1}), \quad (7.8)$$

$$\begin{cases} \mathbf{V}_j^{n+2/4,k} = \mathbf{V}_j^{n+2/4,k-1} + (\Delta t/N) \mathbf{g} \\ + (\Delta t/4N)(1 - \rho_f/\rho_j)^{-1} M_j^{-1} (\mathbf{F}_j^r(\hat{\mathbf{G}}_j^{n+2/4,k}) + \mathbf{F}_j^r(\mathbf{G}_j^{n+2/4,k-1})), \end{cases} \quad (7.9)$$

$$\mathbf{G}_j^{n+2/4,k} = \mathbf{G}_j^{n+2/4,k-1} + (\Delta t/4N)(\mathbf{V}_j^{n+2/4,k} + \mathbf{V}_j^{n+2/4,k-1}), \quad (7.10)$$

enddo; let

$$\mathbf{V}_j^{n+2/4} = \mathbf{V}_j^{n+2/4,N}, \quad \mathbf{G}_j^{n+2/4} = \mathbf{G}_j^{n+2/4,N}. \quad (7.11)$$

Now, we compute $\mathbf{u}^{n+3/4}$, $\{\boldsymbol{\lambda}_j^{n+3/4}, \mathbf{V}_j^{n+3/4}, \boldsymbol{\omega}_j^{n+3/4}\}_{j=1}^J$ via the solution of

$$\left\{ \begin{aligned} & \rho_f \int_{\Omega} \frac{\mathbf{u}^{n+3/4} - \mathbf{u}^{n+2/4}}{\Delta t} \cdot \mathbf{v} \, d\mathbf{x} + \sum_{j=1}^J (1 - \rho_f / \rho_j) M_j \frac{\mathbf{V}_j^{n+3/4} - \mathbf{V}_j^{n+2/4}}{\Delta t} \cdot \mathbf{Y}_j \\ & + \sum_{j=1}^J (1 - \rho_f / \rho_j) I_j \frac{\boldsymbol{\omega}_j^{n+3/4} - \boldsymbol{\omega}_j^n}{\Delta t} \boldsymbol{\theta}_j \end{aligned} \right. \quad (7.12)$$

$$= \sum_{j=1}^J \langle \boldsymbol{\lambda}_j^{n+3/4}, \mathbf{v} - \mathbf{Y}_j - \boldsymbol{\theta}_j \times \overrightarrow{\mathbf{G}_j^{n+2/4} \mathbf{x}} \rangle_{jh}, \quad \forall \mathbf{v} \in V_{0h}, \mathbf{Y}_j \in \mathbb{R}^2, \boldsymbol{\theta}_j \in \mathbb{R},$$

$$\mathbf{u}^{n+3/4} \in V_h, \mathbf{u}^{n+3/4} = \mathbf{g}_{0h}^{n+1} \text{ on } \Gamma, \boldsymbol{\lambda}_j^{n+3/4} \in \Lambda_{jh}^{n+2/4}, \mathbf{V}_j^{n+3/4} \in \mathbb{R}^2, \boldsymbol{\omega}_j^{n+3/4} \in \mathbb{R},$$

$$\langle \boldsymbol{\mu}_j, \mathbf{u}^{n+3/4} - \mathbf{V}_j^{n+3/4} - \boldsymbol{\omega}_j^{n+3/4} \times \overrightarrow{\mathbf{G}_j^{n+2/4} \mathbf{x}} \rangle_{jh} = 0, \quad \forall \boldsymbol{\mu}_j \in \Lambda_{jh}^{n+2/4}. \quad (7.13)$$

Finally, take $\mathbf{V}_j^{n+1,0} = \mathbf{V}_j^{n+3/4}$ and $\mathbf{G}_j^{n+1,0} = \mathbf{G}_j^{n+2/4}$; then predict the final position and translation velocity of B_j as follows, for $j = 1, \dots, J$:

For $k = 1, \dots, N$, compute

$$\hat{\mathbf{V}}_j^{n+1,k} = \mathbf{V}_j^{n+1,k-1} + (\Delta t / 2N) (1 - \rho_f / \rho_j)^{-1} M_j^{-1} \mathbf{F}_j^r(\mathbf{G}_j^{n+1,k-1}), \quad (7.14)$$

$$\hat{\mathbf{G}}_j^{n+1,k} = \mathbf{G}_j^{n+1,k-1} + (\Delta t / 4N) (\hat{\mathbf{V}}_j^{n+1,k} + \mathbf{V}_j^{n+1,k-1}), \quad (7.15)$$

$$\mathbf{V}_j^{n+1,k} = \mathbf{V}_j^{n+1,k-1} + (\Delta t / 4N) (1 - \rho_f / \rho_j)^{-1} M_j^{-1} (\mathbf{F}_j^r(\hat{\mathbf{G}}_j^{n+1,k}) + \mathbf{F}_j^r(\mathbf{G}_j^{n+1,k-1})), \quad (7.16)$$

$$\mathbf{G}_j^{n+1,k} = \mathbf{G}_j^{n+1,k-1} + (\Delta t / 4N) (\mathbf{V}_j^{n+1,k} + \mathbf{V}_j^{n+1,k-1}), \quad (7.17)$$

enddo; let

$$\mathbf{V}_j^{n+1} = \mathbf{V}_j^{n+1,N}, \mathbf{G}_j^{n+1} = \mathbf{G}_j^{n+1,N}. \quad (7.18)$$

We complete the final step by setting

$$\mathbf{u}^{n+1} = \mathbf{u}^{n+3/4}, \quad \{\boldsymbol{\omega}_j^{n+1}\}_{j=1}^J = \{\boldsymbol{\omega}_j^{n+3/4}\}_{j=1}^J. \quad (7.19)$$

As shown above, one of the main advantages of the operator-splitting methodology is that it allows the use of time steps much smaller than Δt to predict and correct the position and velocity of the centers of mass. For our calculations we have taken $N = 10$ or 20 in relations (7.7)–(7.10) and (7.14)–(7.17); thus the local time step used to moved the particles is $\Delta t / N$.

7.3. On the Solution of Subproblems (7.5), (7.6) and (7.12), (7.13): Further Remarks

Problems (7.5) and (7.12), (7.13) are finite dimensional linear problems with the structure

$$\begin{cases} \mathbf{A}\mathbf{x} + \mathbf{B}^t\mathbf{y} = \mathbf{b}, \\ \mathbf{B}\mathbf{x} = \mathbf{c}, \end{cases} \quad (7.20)$$

where, in (7.20), matrix \mathbf{A} is symmetric; actually, the matrix \mathbf{A} associated to problem (7.5) (resp., (7.12), (7.13)) is positive definite (resp., positive definite if $\rho_j > \rho_f, \forall j = 1, \dots, J$).

Problems such as (7.20) are known as *saddle-point systems* and their *iterative solution* by *Uzawa/conjugate gradient algorithms* is discussed, with many details, in, e.g., Refs. [35], [36]. The solution of problems (7.5) and (7.12), (7.13) by the algorithms in [35] and [36] is discussed, again with many details, in Refs. [2], [3], [6], and [7]. The linear problem (7.6) (of the *advection–diffusion* type) can be solved by the *least-squares/conjugate gradient algorithms* discussed in, e.g., Chapter 7 of Ref. [37].

We are now going to use this section for additional comments.

Remark 7.2. We are going to complete Remark 7.1 by observing that, via *further splitting*, we can replace the *advection–diffusion* step (7.6) by

$$\begin{cases} \int_{\Omega} \frac{\partial \mathbf{u}}{\partial t} \cdot \mathbf{v} \, d\mathbf{x} + \int_{\Omega} (\mathbf{u}^{n+1/5} \cdot \nabla) \mathbf{u} \cdot \mathbf{v} \, d\mathbf{x} = 0, \\ \forall \mathbf{v} \in V_{0h}^{n+1,-}, \text{ a.e. on } (n\Delta t, (n+1)\Delta t), \\ \mathbf{u}(n\Delta t) = \mathbf{u}^{n+1/5}, \\ \mathbf{u}(t) \in V_h, \quad \mathbf{u}(t) = \mathbf{g}_{0h}^{n+1} \text{ on } \Gamma_-^{n+1} \times (n\Delta t, (n+1)\Delta t), \end{cases} \quad (7.21)$$

$$\mathbf{u}^{n+2/5} = \mathbf{u}((n+1)\Delta t), \quad (7.22)$$

$$\begin{cases} \rho_f \int_{\Omega} \frac{\mathbf{u}^{n+3/5} - \mathbf{u}^{n+2/5}}{\Delta t} \cdot \mathbf{v} \, d\mathbf{x} + \nu \int_{\Omega} \nabla \mathbf{u}^{n+3/5} : \nabla \mathbf{v} \, d\mathbf{x} = \rho_f \int_{\Omega} \mathbf{g} \cdot \mathbf{v} \, d\mathbf{x}, \\ \forall \mathbf{v} \in V_{0h}; \mathbf{u}^{n+3/5} \in V_h, \mathbf{u}^{n+3/5} = \mathbf{g}_{0h}^{n+1} \text{ on } \Gamma, \end{cases} \quad (7.23)$$

with

- (a) $\mathbf{u}^{n+1/5}$ obtained from \mathbf{u}^n via the “incompressibility” step (7.5),
- (b) $\Gamma_-^{n+1} = \{\mathbf{x} \mid \mathbf{x} \in \Gamma, \mathbf{g}_{0h}^{n+1}(\mathbf{x}) \cdot \mathbf{n}(\mathbf{x}) < 0\}$,
- (c) $V_{0h}^{n+1,-} = \{\mathbf{v} \mid \mathbf{v} \in V_h, \mathbf{v} = 0 \text{ on } \Gamma_-^{n+1}\}$.

Problem (7.23) is a *discrete elliptic system* whose iterative or direct solution is a quite classical problem. On the other hand, solving the *pure advection problem* (7.21) is a more delicate issue. Clearly, problem (7.21) can be solved by a *method of characteristics* (see, e.g., Refs. [29] and [38] and the references therein). An easy-to-implement alternative to the method of characteristics is provided by the *wave-like equation* method briefly discussed below (see [33] and [34] for more details):

Returning to (7.21), observe that this problem is the semidiscrete analogue of

$$\begin{cases} \frac{\partial \mathbf{u}}{\partial t} + (\mathbf{u}^{n+1/5} \cdot \nabla) \mathbf{u} = \mathbf{0} \text{ in } \Omega \times (n\Delta t, (n+1)\Delta t), \\ \mathbf{u}(n\Delta t) = \mathbf{u}^{n+1/5}, \\ \mathbf{u} = \mathbf{g}_0^{n+1} (= \mathbf{u}^{n+1/5}) \text{ on } \Gamma_-^{n+1} \times (n\Delta t, (n+1)\Delta t). \end{cases} \quad (7.24)$$

It follows from (7.24) that, after translation and dilation on the time axis, each component of \mathbf{u} is solution of a transport problem of the type

$$\begin{cases} \frac{\partial \varphi}{\partial t} + \mathbf{V} \cdot \nabla \varphi = 0 \text{ in } \Omega \times (0, 1), \\ \varphi(0) = \varphi_0, \\ \varphi = g \text{ on } \Gamma_- \times (0, 1), \end{cases} \quad (7.25)$$

with $\Gamma_- = \{\mathbf{x} \mid \mathbf{x} \in \Gamma, \mathbf{V}(\mathbf{x}) \cdot \mathbf{n}(\mathbf{x}) < 0\}$ and $\nabla \cdot \mathbf{V} = 0$, $(\partial \mathbf{V} / \partial t) = \mathbf{0}$ and $(\partial g / \partial t) = 0$. We can easily see that problem (7.25) is “equivalent” to the (formally) well-posed problem

$$\begin{cases} \frac{\partial^2 \varphi}{\partial t^2} - \nabla \cdot ((\mathbf{V} \cdot \nabla \varphi) \mathbf{V}) = 0 \text{ in } \Omega \times (0, 1), \\ \varphi(0) = \varphi_0, \quad \frac{\partial \varphi}{\partial t}(0) = -\mathbf{V} \cdot \nabla \varphi_0, \\ \varphi = g \text{ on } \Gamma_- \times (0, 1), \quad \mathbf{V} \cdot \mathbf{n} \left(\frac{\partial \varphi}{\partial t} + \mathbf{V} \cdot \nabla \varphi \right) = 0 \text{ on } (\Gamma \setminus \bar{\Gamma}_-) \times (0, 1). \end{cases} \tag{7.26}$$

Solving the *wave-like equation* (7.26) by a classical finite element/time stepping method is quite easy since a *variational formulation* of (7.26) is given by

$$\begin{cases} \int_{\Omega} \frac{\partial^2 \varphi}{\partial t^2} v \, d\mathbf{x} + \int_{\Omega} (\mathbf{V} \cdot \nabla \varphi)(\mathbf{V} \cdot \nabla v) \, d\mathbf{x} + \int_{\Gamma \setminus \Gamma_-} \mathbf{V} \cdot \mathbf{n} \frac{\partial \varphi}{\partial t} v \, d\Gamma = 0, \quad \forall v \in W_0, \\ \varphi(0) = \varphi_0, \quad \frac{\partial \varphi}{\partial t}(0) = -\mathbf{V} \cdot \nabla \varphi_0, \\ \varphi = g \text{ on } \Gamma_- \times (0, 1), \end{cases} \tag{7.27}$$

with

$$W_0 = \{v \mid v \in H^1(\Omega), v = 0 \text{ on } \Gamma_-\}.$$

Of course when time stepping methods are used to solve subproblem (7.27), a CFL condition has to be satisfied. This can be done easily by choosing as local time step $\Delta t / Q$ with integer Q sufficiently large. Solution methods for the Navier–Stokes equations, taking advantage of the “equivalence” between (7.25) and (7.26), (7.27) are discussed in [33], [34]; see also [39], [40] (and Section 8.6) for further applications, including the simulation of *viscoelastic fluid flow* à la Oldroyd-B.

Remark 7.3. System (7.12), (7.13) is the discrete analogue of

$$\begin{cases} \rho_f \int_{\Omega} \frac{\mathbf{u}^{n+3/4} - \mathbf{u}^{n+2/4}}{\Delta t} \cdot \mathbf{v} \, d\mathbf{x} + \sum_{j=1}^J (1 - \rho_f / \rho_j) M_j \frac{\mathbf{V}_j^{n+3/4} - \mathbf{V}_j^{n+2/4}}{\Delta t} \cdot \mathbf{Y}_j \\ + \sum_{j=1}^J (1 - \rho_f / \rho_j) I_j \frac{\omega_j^{n+3/4} - \omega_j^n}{\Delta t} \theta_j \\ = \sum_{j=1}^J \langle \lambda_j^{n+3/4}, \mathbf{v} - \mathbf{Y}_j - \theta_j \times \overrightarrow{\mathbf{G}_j^{n+2/4} \mathbf{x}} \rangle_j, \quad \forall \mathbf{v} \in (H_0^1(\Omega))^2, \\ \mathbf{Y}_j \in \mathbb{R}^2, \theta_j \in \mathbb{R}; \mathbf{u}^{n+3/4} \in (H^1(\Omega))^2, \\ \mathbf{u}^{n+3/4} = \mathbf{g}_0^{n+1} \text{ on } \Gamma, \lambda_j^{n+3/4} \in \Lambda_j^{n+2/4}, \mathbf{V}_j^{n+3/4} \in \mathbb{R}^2, \omega_j^{n+3/4} \in \mathbb{R}, \end{cases} \tag{7.28}$$

$$\langle \mu_j, \mathbf{u}^{n+3/4} - \mathbf{V}_j^{n+3/4} - \omega_j^{n+3/4} \times \overrightarrow{\mathbf{G}_j^{n+2/4} \mathbf{x}} \rangle_j = 0, \quad \forall \mu_j \in \Lambda_j^{n+2/4}. \tag{7.29}$$

Actually, the analogy between (7.12), (7.13) and (7.28), (7.29) is formal due to the lack of $(H^1(\Omega))^2$ -ellipticity of the bilinear functional $\{\mathbf{v}, \mathbf{w}\} \rightarrow \int_{\Omega} \mathbf{v} \cdot \mathbf{w} \, d\mathbf{x}$ occurring in the left-hand side of (7.28), implying that problem (7.28), (7.29) has no solution, in general, unlike its discrete counterpart (7.12), (7.13). Suppose nevertheless that problem (7.28), (7.29)

has a solution. Taking $\mathbf{v} \in (\mathcal{D}(\Omega \setminus \bigcup_{j=1}^J \bar{B}_j^{n+2/4}))^2$ and $\{Y_j, \theta_j\} = \{\mathbf{0}, 0\}$, $\forall j = 1, \dots, J$, in (7.28) yields

$$\int_{\Omega \setminus \bigcup_{j=1}^J \bar{B}_j^{n+2/4}} (\mathbf{u}^{n+3/4} - \mathbf{u}^{n+2/4}) \cdot \mathbf{v} \, d\mathbf{x} = 0, \quad \forall \mathbf{v} \in \left(\mathcal{D} \left(\Omega \setminus \bigcup_{j=1}^J \bar{B}_j^{n+2/4} \right) \right)^2,$$

which implies in turn that

$$\mathbf{u}^{n+3/4} = \mathbf{u}^{n+2/4} \text{ on } \Omega \setminus \bigcup_{j=1}^J \bar{B}_j^{n+2/4}, \quad (7.30)$$

above (see, e.g., [41] for details)

$$\mathcal{D}(\mathcal{O}) = \{\phi \mid \phi \in C^\infty(\bar{\mathcal{O}}), \phi \text{ has a compact support in } \mathcal{O}\},$$

where \mathcal{O} is an open connected set of \mathbb{R}^d , $d \geq 1$.

We have then from (7.28), (7.29) and (7.30) that $\forall j = 1, \dots, J$,

$$\mathbf{u}^{n+3/4}|_{B_j^{n+2/4}}(\mathbf{x}) = \mathbf{V}_j^{n+3/4} + \boldsymbol{\omega}_j^{n+3/4} \times \overrightarrow{\mathbf{G}_j^{n+2/4} \mathbf{x}}, \quad \forall \mathbf{x} \in B_j^{n+2/4}, \quad (7.31)$$

$$\begin{cases} \rho_f \int_{B_j^{n+2/4}} (\mathbf{u}^{n+3/4} - \mathbf{u}^{n+2/4}) \cdot (\mathbf{Y}_j + \boldsymbol{\theta}_j \times \overrightarrow{\mathbf{G}_j^{n+2/4} \mathbf{x}}) \, d\mathbf{x} \\ + (1 - \rho_f/\rho_j) M_j (\mathbf{V}_j^{n+3/4} - \mathbf{V}_j^{n+2/4}) \cdot \mathbf{Y}_j \\ + (1 - \rho_f/\rho_j) I_j (\boldsymbol{\omega}_j^{n+3/4} - \boldsymbol{\omega}_j^n) \boldsymbol{\theta}_j = 0, \quad \forall \mathbf{Y}_j \in \mathbb{R}^2, \boldsymbol{\theta}_j \in \mathbb{R}. \end{cases} \quad (7.32)$$

Combining (7.31) with (7.32) yields, $\forall j = 1, \dots, J$,

$$\mathbf{V}_j^{n+3/4} = (2 - \rho_f/\rho_j)^{-1} \left[(1 - \rho_f/\rho_j) \mathbf{V}_j^{n+2/4} + \frac{\rho_j}{M_j} \int_{B_j^{n+2/4}} \mathbf{u}^{n+2/4} \, d\mathbf{x} \right], \quad (7.33)$$

and

$$\boldsymbol{\omega}_j^{n+3/4} = (2 - \rho_f/\rho_j)^{-1} \left[(1 - \rho_f/\rho_j) \boldsymbol{\omega}_j^n + \frac{\rho_j}{I_j} \int_{B_j^{n+2/4}} \overrightarrow{\mathbf{G}_j^{n+2/4} \mathbf{x}} \times \mathbf{u}^{n+2/4} \, d\mathbf{x} \right]. \quad (7.34)$$

The practical implementation of (7.33) and (7.34)—via numerical integration methods—is quite easy, and we observe that the *neutrally buoyant* case ($\rho_j = \rho_f$) does not present any particular difficulty. After obtaining $\{\mathbf{V}_j^{n+3/4}, \boldsymbol{\omega}_j^{n+3/4}\}_{j=1}^J$, we enforce the rigid body motion inside the particle region by interpolation. However, one has to realize that $\mathbf{u}^{n+3/4}$ and $\{\mathbf{V}_j^{n+3/4}, \boldsymbol{\omega}_j^{n+3/4}\}_{j=1}^J$ computed via (7.30), (7.31), (7.33), and (7.34) are *not solutions* of system (7.12), (7.13), in general, particularly if control points located on $\partial B_j^{n+2/4}$ are used to enforce the rigid body motion. Moreover, numerical results show that the results obtained from the solution of the system (7.12), (7.13) are of better qualities than those provided by (7.33), (7.34) (which is of course much cheaper and easier to implement).

Remark 7.4. There is nothing mysterious about relations (7.7)–(7.11) and (7.14)–(7.18). Relations (7.7)–(7.11) (resp., (7.14)–(7.18)) follow from the time discretization, *after operator splitting*, of

$$\begin{cases} (1 - \rho_f/\rho_j) M_j \frac{d\mathbf{V}_j}{dt} = (1 - \rho_f/\rho_j) M_j \mathbf{g} + (1/2) \mathbf{F}_j^r, \\ \frac{d\mathbf{G}_j}{dt} = \mathbf{V}_j/2 \end{cases}$$

(resp.,

$$\begin{cases} (1 - \rho_f/\rho_j)M_j \frac{d\mathbf{V}_j}{dt} = (1/2)\mathbf{F}_j^r, \\ \frac{d\mathbf{G}_j}{dt} = \mathbf{V}_j/2. \end{cases}$$

That is, the right-hand-side terms \mathbf{F}_j^r and \mathbf{V}_j have been equally distributed “over” the second and forth fractional steps; other decompositions are possible.

8. NUMERICAL EXPERIMENTS

8.1. Synopsis

In this section, we are going to apply the computational methods discussed in Sections 4 to 7 to the numerical simulation of various two- and three-dimensional fluid/solid interaction phenomena, including sedimentation and fluidization for particulate flow and store separation. Schematically, these numerical experiments can be divided in two families: the first family concerns situations where the number of rigid bodies is small (from 1 to 3), while the second family is concerned with fluid/solid interactions involving more than 10^3 particles; actually, we will present results concerning the direct numerical simulation of a Rayleigh–Taylor instability for particulate flow, the number of particles being 6,400.

More numerical results obtained by the methods discussed in this article can be found in Refs. [2–8].

8.2. Numerical Simulation of the Motion of a Ball Falling in an Incompressible Viscous Fluid

8.2.1. Generalities and Motivation

In this section we consider the numerical simulation of the *motion of a ball falling in an incompressible Newtonian viscous fluid* by the methods discussed in Sections 4 to 7. Among the reasons to consider the above test problem let us mention its simplicity when compared to some of the test problems to follow, and also the fact that it will give us the possibility of validating our methods by comparing the computed terminal velocities with the measured ones reported in Ref. [42].

8.2.2. Description of the Test Problem

The phenomenon that we intend to simulate is the following: a rigid ball of diameter d and density ρ_s is located, at time $t = 0$, on the axis (assumed vertical, i.e., parallel to the gravity vector \mathbf{g}) of an infinitely long circular cylinder of diameter 1. We suppose that the cylinder is filled with a Newtonian incompressible viscous fluid of density $\rho_f = 1$ and viscosity ν ; we suppose also that the ball and the fluid are at rest initially (i.e., $\mathbf{V}_G(0) = \mathbf{0}$, $\boldsymbol{\omega}(0) = \mathbf{0}$ and $\mathbf{u}(0)(=\mathbf{u}_0) = \mathbf{0}$) and that $\mathbf{u}(t) = \mathbf{0}$, $\forall t \geq 0$, on the boundary of the cylinder. Under the effect of gravity the ball is going to fall and slowed down by the fluid viscosity will reach a constant falling velocity (the terminal velocity); this supposes that the Reynolds number is small enough so that the falling ball will stay close enough to the axis not to touch the wall of the cylinder. The related experiment is well documented in Ref. [42].

TABLE 8.1
Comparison between Computed and Experimental
Terminal Velocities ($\rho_s = 1.02$ and $d = 0.2$)

ν	U_c	U_{exp}	Relative error (%)	Re
0.20	0.1354	0.1317	2.8	0.135
0.15	0.1762	0.1750	0.7	0.234
0.10	0.2567	0.2571	0.2	0.513
0.05	0.4844	0.4603	5.2	1.93
0.02	0.9480	0.9129	3.8	9.48
0.01	1.310	1.411	7.1	26.2

8.2.3. *A Short Description of the Computational Methodology*

The initial computational domain is $\Omega(0) = (0, 1) \times (0, 1) \times (0, 2.5)$; then it moves with the center of the ball (we shall call $\Omega(t)$ the corresponding position at time t). The truncated circular cylinder is contained (embedded) in the computational domain and we force the velocity field outside the cylinder to be zero by another distributed Lagrange multiplier. To approximate the velocity we divide $\Omega(t)$ into elementary cubes of length h_Ω , then divide each elementary cube into six tetrahedra of height h_Ω and base area $h_\Omega^2/2$; the set of these elementary tetrahedra will be the “triangulation” $\mathcal{T}_h(t)$ used to approximate the velocity. The pressure will be approximated using a twice coarser similar “triangulation.”

The resulting discrete problem has been solved using the techniques discussed in Section 4 to 7 with $h_\Omega = 1/64$ and $\Delta t = 5 \times 10^{-4}$, implying that the number of velocity (resp., pressure) grid points is of the order of 650,000 (resp. 82,000). To approximate the multiplier space $\Lambda_h(t)$ we have used the “hybrid” approach defined by (6.16) in Remark 6.4, and on that space used $\langle \cdot, \cdot \rangle_{jh}$ defined by (6.6). Finally, the linear advection–diffusion problems (7.6) have been solved using the least-squares/conjugate gradient algorithms discussed in [34, Chap. 7] (see also [43]).

8.2.4. *Description of the Numerical Results and Comparison with Experimental Data*

The fall of the ball in the viscous fluid has been simulated for $d = 0.2, 0.3, 0.4, \rho_s = 1.02, 1.14$, and $\nu = 0.2, 0.15, 0.1, 0.05, 0.02, 0.01$. Assuming that at $t = 0$ the ball is located at $\mathbf{G}(0) = \{.5, .5, .5\}$ we obtain the computed terminal velocities (U_c) reported in Tables 8.1 to 8.6; we have also reported in these tables the corresponding experimental

TABLE 8.2
Comparison between Computed and Experimental Terminal
Velocities ($\rho_s = 1.02$ and $d = 0.3$)

ν	U_c	U_{exp}	Relative error (%)	Re
0.20	0.2144	0.2164	0.9	0.321
0.15	0.2794	0.2840	1.6	0.558
0.10	0.4072	0.4047	0.6	1.22
0.05	0.7599	0.7493	1.4	4.56
0.02	1.392	1.4359	3.0	20.85
0.01	1.831	2.107	13.1	54.9

TABLE 8.3
Comparison between Computed and Experimental
Terminal Velocities ($\rho_s = 1.02$ and $d = 0.4$)

ν	U_c	U_{exp}	Relative error (%)	Re
0.20	0.2536	0.2487	2	0.507
0.15	0.3299	0.3362	1.9	0.88
0.10	0.4799	0.4977	3.6	1.92
0.05	0.8930	0.8600	3.8	7.14
0.02	1.625	1.695	4.2	32.5
0.01	2.098	2.422	13.4	84

TABLE 8.4
Comparison between Computed and Experimental
Terminal Velocities ($\rho_s = 1.14$ and $d = 0.2$)

ν	U_c	U_{exp}	Relative error (%)	Re
0.20	0.9367	0.8707	7.6	0.937
0.15	1.203	1.102	9.2	1.60
0.10	1.672	1.552	7.7	3.34
0.05	2.617	2.489	5.1	10.5
0.02	3.812	4.334	12	38.1

TABLE 8.5
Comparison between Computed and Experimental
Terminal Velocities ($\rho_s = 1.14$ and $d = 0.3$)

ν	U_c	U_{exp}	Relative error (%)	Re
0.20	1.478	1.401	5.5	2.22
0.15	1.888	1.786	5.7	3.78
0.10	2.574	2.426	6.1	7.71
0.05	3.823	3.972	3.7	22.9
0.02	5.216	6.283	17	78.3

TABLE 8.6
Comparison between Computed and Experimental
Terminal Velocities ($\rho_s = 1.14$ and $d = 0.4$)

ν	U_c	U_{exp}	Relative error (%)	Re
0.20	1.746	1.673	4.3	3.49
0.15	2.226	2.057	8.2	5.93
0.10	3.031	2.868	5.7	12.1
0.05	4.448	4.573	2.7	35.6
0.02	5.892	6.946	15.2	118

terminal velocities (U_{exp}) (obtained from [42]), the associated relative errors, and the corresponding Reynolds number (based on the formula $\text{Re} = U_c d / \nu$).

It is our opinion that the agreement between computed and experimental terminal velocities is quite good, particularly if one takes into consideration that the experimental terminal velocities taken from Ref. [42] are obtained, in fact, by multiplying the terminal velocities of a ball falling in an unbounded flow region (in practice a region very large compared to the size of the ball) by a wall correction factor. This explains the large number of digits in the experimental data and suggests, also, that these data contain other errors than those due to measurement. Actually, the large discrepancies observed for $\nu = 0.01$, $\rho_s = 1.02$ and $\nu = 0.02$, $\rho_s = 1.14$ are very likely caused by the fact that when the falling velocity becomes sufficiently large a *symmetry breaking* takes place, and the ball “leaves” the axis of the cylinder and falls along a spiraling trajectory. For more details about the test case discussed in this section and further comparisons with experimental data see Ref. [44].

8.3. Numerical Simulation of the Sedimentation of a Circular Disk

8.3.1. Description of the Test Problem

The objective of this test problem is to simulate the fall of a rigid circular disk in a bounded cavity Ω filled with an incompressible Newtonian viscous fluid. Simulating the impact of the cylinder with the bottom boundary of the cavity is part of the computational experiment.

8.3.2. On the Computational Methodology

The computational techniques used for the simulations are those discussed in Sections 4 to 7. To construct the triangulations \mathcal{T}_h used to approximate the velocity, we have first divided the cavity Ω into elementary squares of length h_Ω and then each square into two triangles as shown in Fig. 8.1.

We proceed similarly to construct the (twice coarser) pressure grid. The multiplier space $\Lambda(t)$ and the pairing $\langle \cdot, \cdot \rangle$ have been approximated as in Section 8.2.3. Concerning now the treatment of the advection–diffusion two approaches have been implemented, namely the

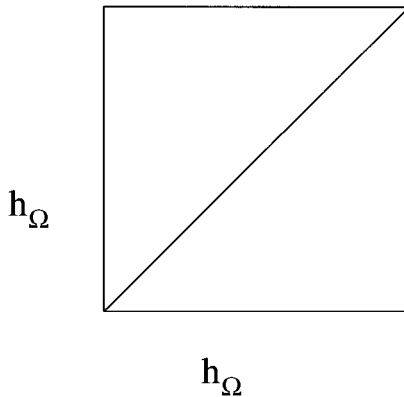


FIG. 8.1. Division of an elementary square.

global approach where advection and diffusion are treated at once as in Section 8.2.3 and the approach advocated in Remark 7.2 where a wave-like equation method is used to treat the advection after decoupling from diffusion via an additional fractional step in scheme (7.4)–(7.19) (see Remark 7.2 for details). Actually, we have used these two approaches in order to cross-validate our computational methods.

8.3.3. On the Geometry, Initial and Boundary Conditions, and Other Parameters

- The computational domain is $\Omega = (0, 2) \times (0, 6)$.
- The diameter of the disk is $d = 0.25$.
- The center \mathbf{G} of the disk is located at $\{1, 4\}$ at time $t = 0$.
- The fluid and the disk are initially at rest, i.e., $\mathbf{u}(0)(=\mathbf{u}_0) = \mathbf{0}$, $\dot{\mathbf{G}}(0) = \boldsymbol{\omega}(0) = \mathbf{0}$.
- The fluid velocity is $\mathbf{0}$, $\forall t \geq 0$, on the boundary of Ω .
- The fluid density is $\rho_f = 1$.
- The disk density ρ_s is either 1.25 or 1.5.
- The fluid viscosity ν is either 0.1 or 0.01.
- The velocity mesh size h_Ω is either 1/192 or 1/256 or 1/384; the pressure mesh size is $h_p = 2h_\Omega$.
- The time discretization step Δt is either 10^{-3} or 7.5×10^{-4} or 5×10^{-4} .
- The parameter ε used in the collision model is of the order of 10^{-5} .

From the above characteristics we can see that we have (approximately) 440,000, 786,000, and 1.77×10^6 (resp., 110,000, 196,000, and 442,000) vertices for the three velocity (resp., pressure) triangulations used for the simulations.

8.3.4. Description of the Numerical Results

In Fig. 8.2 we have visualized the flow and the particle position at $t = 0.3$ for $\rho_s = 1.25$ and $\nu = 0.1$. The figures associated to $h_\Omega = 1/192$, $\Delta t = 10^{-3}$ are practically indiscernible of those obtained with $h_\Omega = 1/256$, $\Delta t = 7.5 \times 10^{-4}$, and $h_\Omega = 1/384$, $\Delta t = 5 \times 10^{-4}$. Similarly, the figures associated to the least-squares/conjugate gradient treatment of the advection–diffusion and those obtained from the wave-like equation treatment of the advection are essentially identical. Further results and comparisons are shown in Figs. 8.3 to 8.5.

The above figures show that, in practice, the cylinder quickly reaches a uniform falling velocity until it hits the bottom of the cavity. A careful examination of Fig. 8.3 shows that a symmetry breaking of small amplitude is taking place with the disk moving slightly on the right, away from the vertical symmetry axis of the cavity. Figure 8.5 shows that the rotational component of the kinetic energy is small compared to the translational one. The maximal computed disk Reynolds numbers are 17.27 for $h_\Omega = 1/192$, $\Delta t = 10^{-3}$ and 17.31 for $h_\Omega = 1/256$, $\Delta t = 7.5 \times 10^{-3}$.

The results obtained using the wave-like equation approach to treat advection (once decoupled from diffusion) are very close to those which have been reported above. An evidence of this very good agreement is provided by Fig. 8.6 where we have compared the kinetic energies obtained by both approaches.

Another evidence of the good agreement between both approaches is that the maximum disk Reynolds numbers obtained via the wave-like equation method are 17.44 for $h_\Omega = 1/192$, $\Delta t = 10^{-3}$ and 17.51 for $h_\Omega = 1/256$, $\Delta t = 7.5 \times 10^{-4}$, to be compared to 17.27 and 17.31.

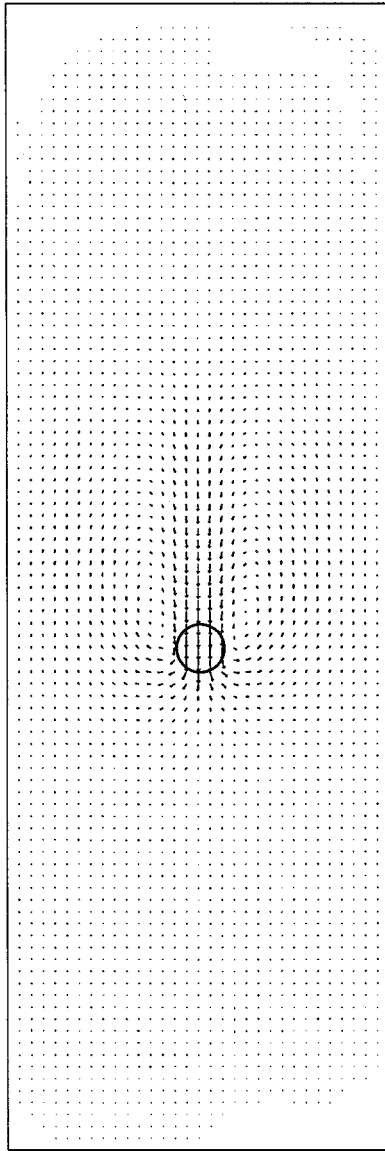


FIG. 8.2. Particle position and flow field visualization at $t = 0.3$ ($\rho_s = 1.25$, $\nu = 0.1$, $h_\Omega = 1/256$, $\Delta t = 7.5 \times 10^{-4}$).

From the good agreement between both approaches and since the wave-like equation approach is computationally faster (see Section 8.3.5 for precise comparisons) and easier to implement, it has been selected as the method of choice for most of the two-dimensional test problems which follow (its 3-D implementation is currently in progress). This applies in particular to the variant of the above test problem where, this time, $\rho_s = 1.5$ and $\nu = 0.01$, everything else remaining the same. From the increased density of the disk and reduced viscosity of the fluid we can expect the disk motion to be much faster and the symmetry breaking to be more pronounced than in the previous experiment. These predictions are confirmed by the results shown in Figs. 8.7–8.11.

With the exception of the rotational kinetic energy (for which we still have “qualitative” agreement) the computed results are in good quantitative agreement for the various values

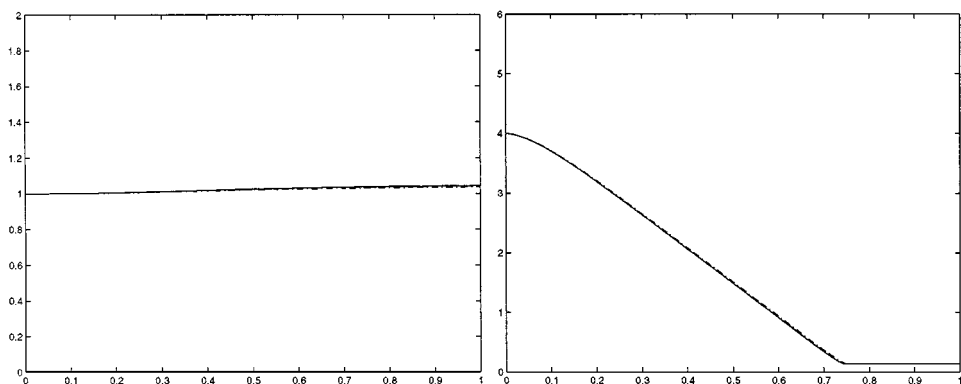


FIG. 8.3. Histories of the x -coordinate (left) and y -coordinate (right) of the center of the disk for $\rho_s = 1.25$ and $\nu = 0.1$ ($h_\Omega = 1/192$ and $\Delta t = 10^{-3}$, solid lines; $h_\Omega = 1/256$ and $\Delta t = 7.5 \times 10^{-4}$, dashed-dotted lines). Least-squares/conjugate gradient treatment of advection-diffusion.

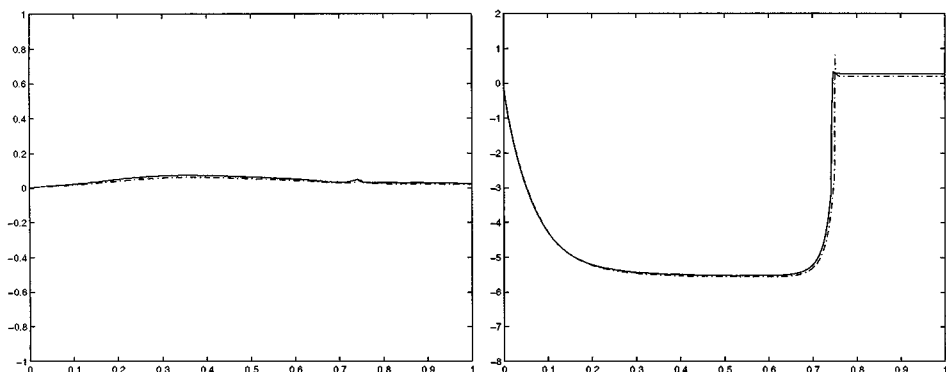


FIG. 8.4. Histories of the x -component (left) and y -component (right) of the translation velocity of the disk for $\rho_s = 1.25$ and $\nu = 0.1$ ($h_\Omega = 1/192$ and $\Delta t = 10^{-3}$, solid lines; $h_\Omega = 1/256$ and $\Delta t = 7.5 \times 10^{-4}$, dashed-dotted lines). Least-squares/conjugate gradient treatment of advection-diffusion.

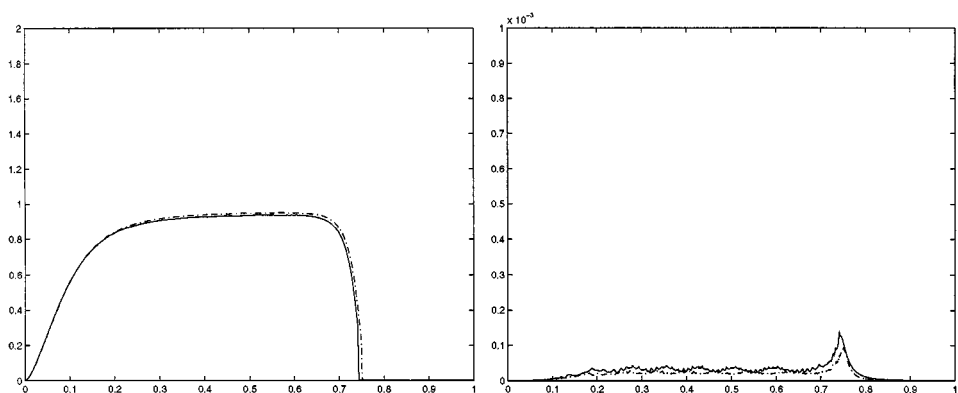


FIG. 8.5. Histories of translational (left) and rotational (right) kinetic energies of the disk for $\rho_s = 1.25$ and $\nu = 0.1$ ($h_\Omega = 1/192$ and $\Delta t = 10^{-3}$, solid lines; $h_\Omega = 1/256$ and $\Delta t = 7.5 \times 10^{-4}$, dashed-dotted lines). Least-squares/conjugate gradient treatment of advection-diffusion.

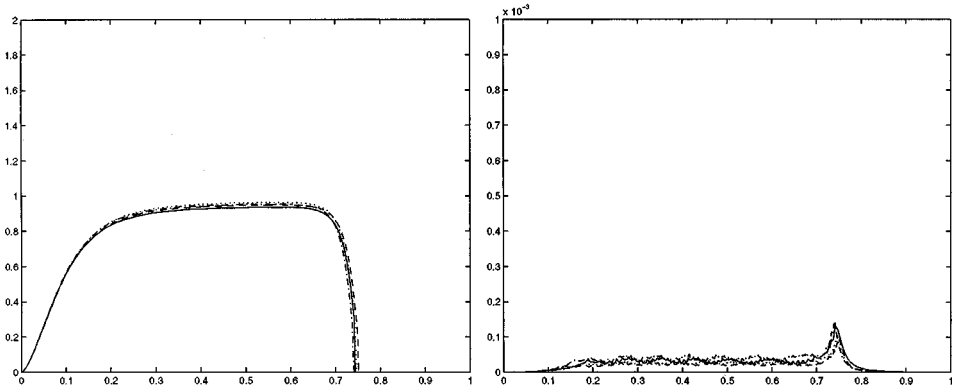


FIG. 8.6. Histories of translational (left) and rotational (right) kinetic energies of the disk for $\rho_s = 1.25$ and $\nu = 0.1$. Least-squares/conjugate gradient treatment of advection–diffusion with $h_\Omega = 1/192$ and $\Delta t = 10^{-3}$ (solid line) and with $h_\Omega = 1/256$ and $\Delta t = 7.5 \times 10^{-4}$ (dashed line). Wave-like equation treatment of advection with $h_\Omega = 1/192$ and $\Delta t = 10^{-3}$ (dashed-dotted line) and with $h_\Omega = 1/256$ and $\Delta t = 7.5 \times 10^{-4}$ (dotted line).

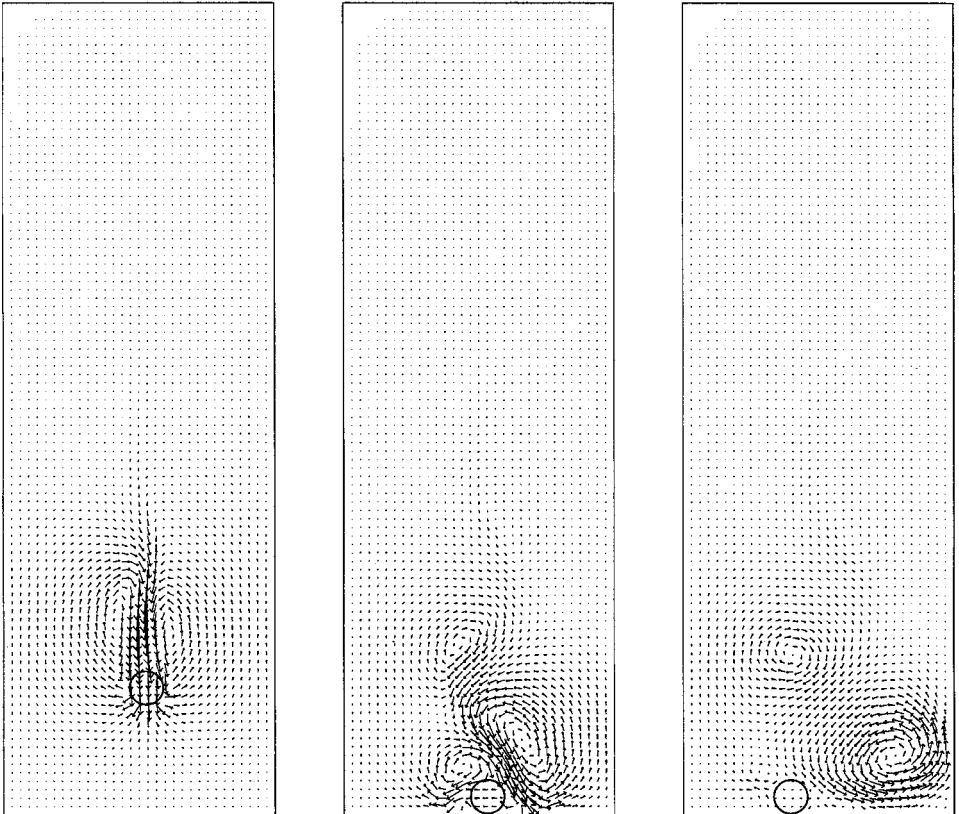


FIG. 8.7. Particle position and flow field visualization at $t = 0.3$ (left), $t = 0.4$ (center), and $t = 0.5$ (right) ($\rho_s = 1.5$, $\nu = 0.01$, $h_\Omega = 1/384$, $\Delta t = 5 \times 10^{-4}$; wave-like equation treatment of the advection).

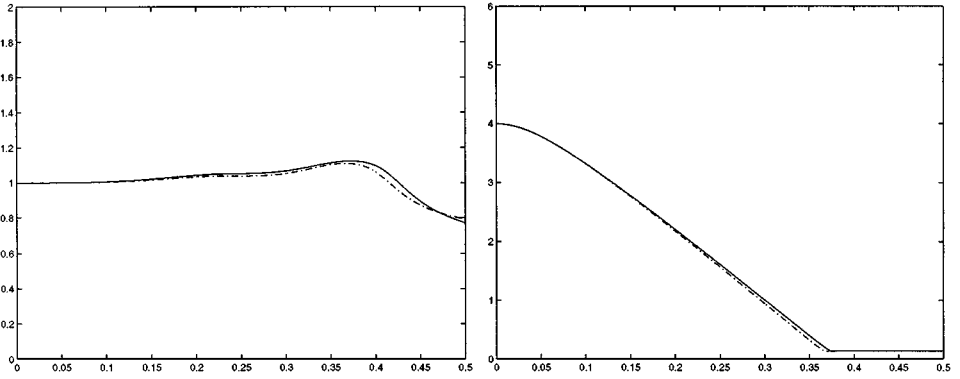


FIG. 8.8. Histories of the x -coordinate (left) and y -coordinate (right) of the center of the disk for $\rho_s = 1.5$ and $\nu = 0.01$ ($h_\Omega = 1/256$ and $\Delta t = 7.5 \times 10^{-4}$, solid lines; $h_\Omega = 1/384$ and $\Delta t = 5 \times 10^{-4}$, dashed-dotted lines; wave-like equation treatment of the advection).

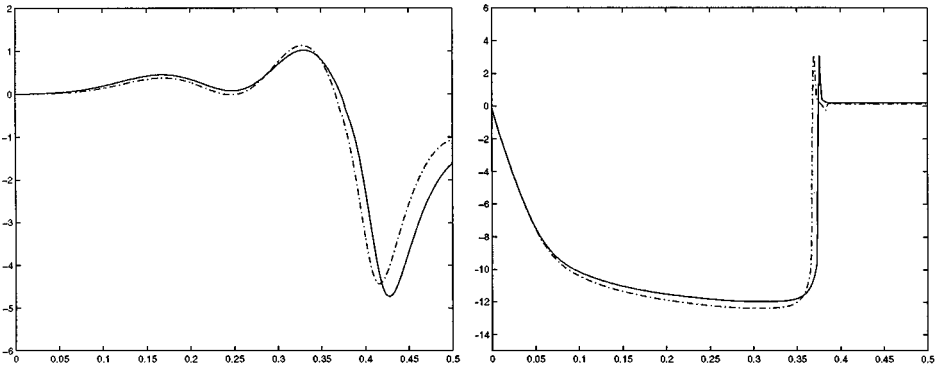


FIG. 8.9. Histories of the translation velocity of the disk for $\rho_s = 1.5$ and $\nu = 0.01$ ($h_\Omega = 1/256$ and $\Delta t = 7.5 \times 10^{-4}$, solid lines; $h_\Omega = 1/384$ and $\Delta t = 5 \times 10^{-4}$, dashed-dotted lines; wave-like equation treatment of the advection).

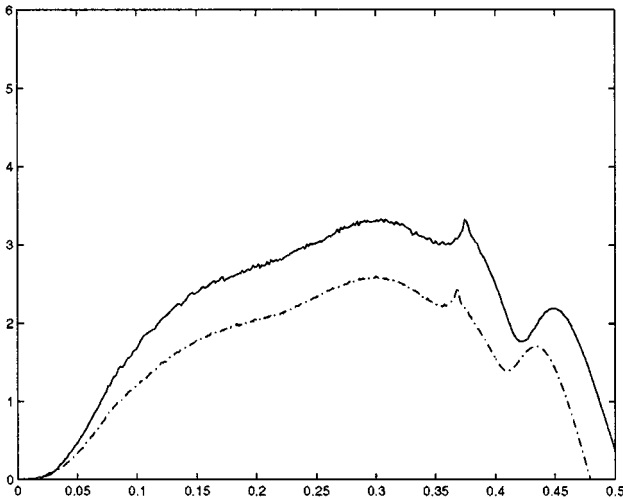


FIG. 8.10. History of the angular velocity of the disk for $\rho_s = 1.5$ and $\nu = 0.01$ ($h_\Omega = 1/256$ and $\Delta t = 7.5 \times 10^{-4}$, solid line; $h_\Omega = 1/384$ and $\Delta t = 5 \times 10^{-4}$, dashed-dotted line; wave-like equation treatment of the advection).

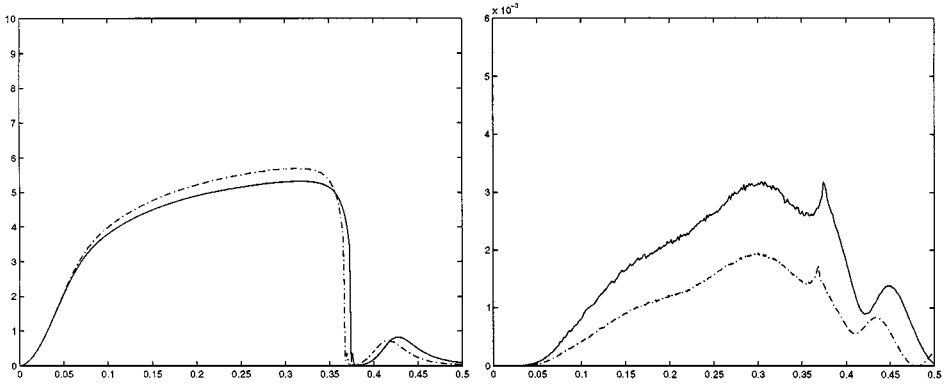


FIG. 8.11. Histories of the translational (left) and rotational (right) kinetic energies of the disk for $\rho_s = 1.5$ and $\nu = 0.01$ ($h_\Omega = 1/256$ and $\Delta t = 7.5 \times 10^{-4}$, solid lines; $h_\Omega = 1/384$ and $\Delta t = 5 \times 10^{-4}$, dashed-dotted lines; wave-like equation treatment of the advection).

of h_Ω and Δt . In particular, the maximum computed disk Reynolds numbers are 438.6 for $h_\Omega = 1/192$ and $\Delta t = 10^{-3}$, 450.7 for $h_\Omega = 1/256$ and $\Delta t = 7.5 \times 10^{-4}$, and 466 for $h_\Omega = 1/384$ and $\Delta t = 5 \times 10^{-4}$; this is quite good agreement if one considers that one is dealing with a highly nonlinear phenomenon involving symmetry breaking. Actually, the above figures show that the symmetry breaking weakens as h and Δt decrease. This is not surprising since the above symmetry breaking is triggered by the (non-symmetric) perturbations associated to our numerical methods (our triangulations, for example, are not symmetric with respect to the cavity axis (i.e., the line $x_1 = 3$)); as h decreases the quality of the approximation increases implying that the level of perturbation decreases, leading to symmetry breakings of smaller amplitude. Let us observe that for $h_\Omega = 1/384$ the velocity (resp., pressure) triangulation has approximately 1.77×10^6 (resp., 442,000) vertices, respectable numbers indeed.

8.3.5. Further Details on Implementation

Let us provide some further information concerning the computer implementation of the methods discussed in Sections 3 to 7, when applied to the test problem described in Sections 8.3.1 and 8.3.3. Without going into excruciating detail, let us say that:

- We have taken ε ranging from 5×10^{-5} to 5×10^{-6} in the collision model associated to relation (5.2). The parameter ρ in (5.2) (the thickness of the safety zone) has been taken of the order of $2.5 h_\Omega$.
- The number of conjugate gradient iterations necessary to force the discrete incompressibility is of the order of 12.
- If the least-squares/conjugate gradient methodology advocated in [37] and [43] is used to treat the advection–diffusion it requires two (preconditioned) iterations at most.
- If one uses the wave-like equation approach to treat the advection the number of sub-time steps used to integrate the wave-like equation (7.26) is of the order of five.
- The number of iterations necessary to force the rigidity inside the disk varies from 70 to 100 (it increases with the maximal Reynolds number). This may seem quite large, but things have to be put in perspective for the following reasons:

(i) The dimension of the discrete multiplier space Λ_h is small compared to the dimensions of the velocity space V_h and pressure space P_h . We have indeed

TABLE 8.7
CPU per Time Step (in Seconds)

ρ_s	ν	h	Δt	Adv. treat.	CPU/timestep(s)
1.25	0.1	1/192	10^{-3}	l.s./c.g.	29.7
1.25	0.1	1/192	10^{-3}	w.-l. eq.	25.6
1.25	0.1	1/256	7.5×10^{-4}	l.s./c.g.	60.8
1.25	0.1	1/256	7.5×10^{-4}	w.-l. eq.	60.6
1.5	10^{-2}	1/192	10^{-3}	w.-l. eq.	31
1.5	10^{-2}	1/256	7.5×10^{-4}	w.-l. eq.	54.8
1.5	10^{-2}	1/384	5×10^{-4}	w.-l. eq.	140.8

$$\begin{aligned} \dim V_h &\simeq 880,000, & \dim P_h &\simeq 110,000, & \text{and } \dim \Lambda_h &\simeq 3,700 & \text{if } h = 1/192, \\ \dim V_h &\simeq 1.57 \times 10^6, & \dim P_h &\simeq 196,000, & \text{and } \dim \Lambda_h &\simeq 6,400 & \text{if } h = 1/256, \\ \dim V_h &\simeq 3.54 \times 10^6, & \dim P_h &\simeq 42,000, & \text{and } \dim \Lambda_h &\simeq 14,600 & \text{if } h = 1/384. \end{aligned}$$

(ii) The problems of type (7.20) encountered in this application have been solved by a diagonally preconditioned conjugate gradient algorithm implying that each iteration is quite inexpensive.

From the above reasons, most of the CPU time is spent in solving the Navier–Stokes equations. Of course for those situations with many particles, where the ratio solid volume/fluid volume is of order 1 it may be worthwhile to precondition the conjugate gradient algorithm, used to compute the multipliers, by the symmetric and positive definite matrices associated to the scalar products (4.16) or (4.17) restricted to Λ_{jh} .

- The discrete Poisson problems encountered in computing the discrete pressure and forcing the discrete incompressibility condition “take place” on a regular grid; we can therefore use *fast Poisson Solvers* based on *cyclic reduction* to solve these problems (see, e.g., Ref. [45] for a discussion of cyclic reduction methods). Similarly, the elliptic problems encountered when treating diffusion (with or without advection) can be solved by fast direct solvers based on cyclic reduction.

- The wave-like equation-based methodology (w.-l. eq.) seems to be 20% faster than the one based on the least-squares/conjugate gradient treatment (l.s./c.g.) of advection–diffusion; it is also easier to implement.

- The computational times per time step on a one-processor DEC Alpha 500-au workstation are given in Table 8.7 (where the notation is self-explanatory). These figures can be substantially reduced via parallelization since the good potential for parallelization of the fictitious domain methods has not been taken advantage of in these simulations (see, e.g., ref. [46] for the parallelization of the fictitious domain methods discussed in this article).

8.4. Numerical Simulation of the Motion and Interaction of Two Circular Disks Sedimenting in an Incompressible Newtonian Viscous Fluid

8.4.1. Description of the Test Problem

The objective of this test problem is to simulate the motion and the interaction of two identical rigid circular disks sedimenting in a vertical channel. The two disks are initially at rest on the axis of the channel, the distance between their centers being one disk diameter.

We expect the simulations to reproduce the well documented *drafting, kissing, and tumbling* phenomenon; this phenomenon has been observed in laboratory experiments and also via simulations based on computational methods different of the ones discussed in this article (see, for example, [47, 48], and the references therein).

The computational methods used for this test problem are those already employed for the test problems of Section 8.3.

8.4.2. On the Geometry, Initial and Boundary Conditions, and Other Parameters

- The computational domain at time $t = 0$ is $\Omega(0) = (0, 2) \times (0, 6)$ and is moving with the disks.
- The diameter of the disks is $d = 0.25$.
- The initial positions of the disk centers are $\{1, 4.5\}$ and $\{1, 5\}$.
- The fluid and the disks are initially at rest.
- The fluid velocity is $\mathbf{0}$, $\forall t \geq 0$, on the boundary of the channel.
- The fluid density is $\rho_f = 1$.
- The disk density is $\rho_s = 1.5$.
- The fluid viscosity is $\nu = 0.01$.
- The discretization parameters are $\{h_\Omega, \Delta t\} = \{1/192, 10^{-3}\}, \{1/256, 7.5 \times 10^{-4}\}, \{1/384, 5 \times 10^{-4}\}$.
- The collision parameter is $\varepsilon = 5 \times 10^{-6}$.
- The safety zone thickness ρ in the collision model ranges from $2h_\Omega$ to $4h_\Omega$.

8.4.3. Description of the Numerical Results

The results shown below have been obtained using the wave-like equation approach of Section 7.3, Remark 7.2, to treat the advection.

The drafting, kissing, and tumbling phenomenon mentioned above is clearly observed in Fig. 8.12. The accepted explanation of this phenomenon is as follows:

The lower disk, when falling, creates a pressure drop in its wake. This implies that—if initially close enough—the upper disk encounters less resistance from the fluid than the lower one and falls faster. Falling faster, the upper disk touches (or almost touches) the lower one. Once in contact (or quasi-contact), the two disks act as an elongated body falling in an incompressible viscous fluid. As is well known, elongated bodies falling sufficiently fast in a Newtonian incompressible viscous fluid have a tendency to rotate so that their broad sides become perpendicular to the flow direction. Indeed rotation takes place, as seen in Fig. 8.12 at $t = 0.2$, but the two-disks assemblage is unstable and the two disks separate. The maximum computed *disk Reynolds number* is 664 (resp., 680 and 689) for $\{h_\Omega, \Delta t\} = \{1/192, 10^{-3}\}$ (resp., $\{1/256, 7.5 \times 10^{-4}\}$ and $\{1/384, 5 \times 10^{-4}\}$). The computed *minimal distance* between the two disks is $1.26h_\Omega$, $1.03h_\Omega$, and $2.1h_\Omega$ for $\{h_\Omega, \Delta t\} = \{1/192, 10^{-3}\}, \{1/256, 7.5 \times 10^{-4}\}$ and $\{1/394, 5 \times 10^{-4}\}$; it occurs at $t = 0.157, 0.161, \text{ and } 0.163$, respectively. Considering that drafting, kissing, and tumbling is a violent phenomenon (see Fig. 8.14 for evidence of this violence) the agreement between the computed results for the various values of h_Ω and Δt is quite good. Calculations done with $\rho_s = 1.25$ confirm the above results; actually, the agreement is even better since the disk motions and fluid flow are slower due to the smaller value of $\rho_s - \rho_f$.

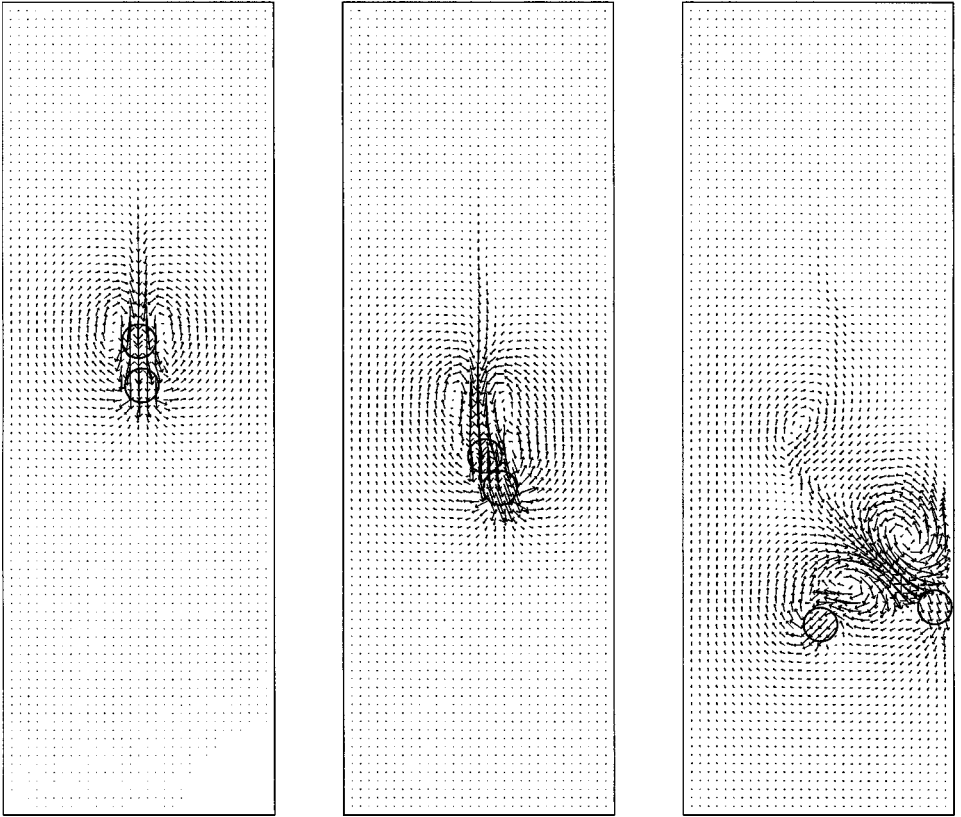


FIG. 8.12. Disks positions and flow field visualization at $t = 0.15, 0.2$, and 0.3 ($\rho_s = 1.5$, $\nu = 10^{-2}$, $h_\Omega = 1/384$, $\Delta t = 5 \times 10^{-4}$). Wave-like equation treatment of the advection.

The various observations and comments done in Section 8.3.3 (for the sedimentation of one disk) still apply to the present test problem (see Figs. 8.13–8.15). Actually, the costs and numbers of iterations associated to the solution of the various subproblems are close, although the two-disk simulation is a bit more expensive than the one-disk one, since it

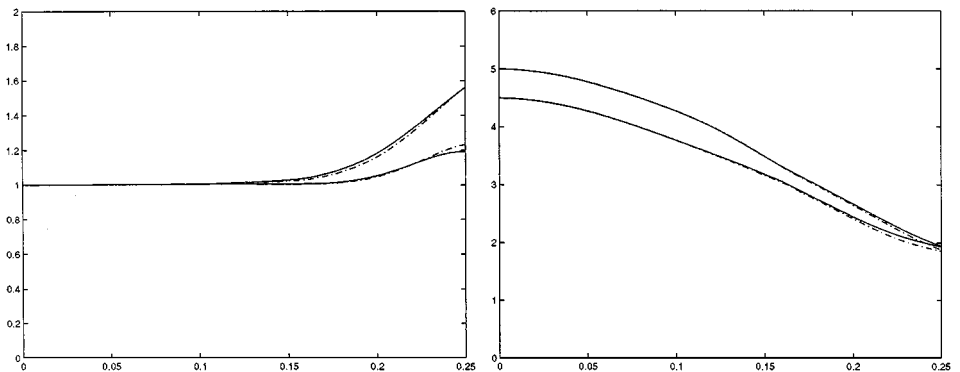


FIG. 8.13. Histories of the x -coordinate (left) and y -coordinate (right) of the centers of the disks for $\rho_s = 1.5$ and $\nu = 10^{-2}$ ($h_\Omega = 1/256$, $\Delta t = 7.5 \times 10^{-4}$, solid lines; $h_\Omega = 1/384$, $\Delta t = 5 \times 10^{-4}$, dashed-dotted lines). Wave-like equation treatment of the advection.

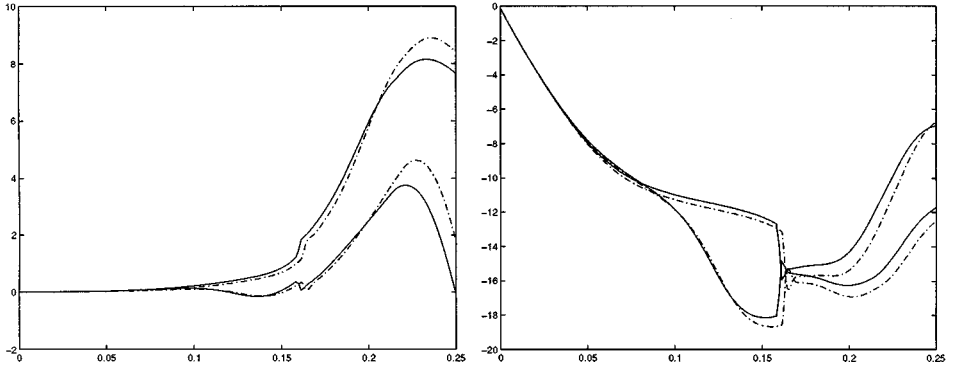


FIG. 8.14. Histories of the x -coordinate (left) and y -coordinate (right) of the translational velocity of the disks for $\rho_s = 1.5$ and $\nu = 10^{-2}$ ($h_\Omega = 1/256$, $\Delta t = 7.5 \times 10^{-4}$, solid lines; and $h_\Omega = 1/384$, $\Delta t = 5 \times 10^{-4}$, dashed-dotted lines). Wave-like equation treatment of the advection.

leads to higher Reynolds numbers for the same values of ρ_s , ρ_f , and ν . For example, the CPU times per time-step on the same DEC Alpha 500-au workstation are 44, 79, and 200 s for $\{h_\Omega, \Delta t\} = \{1/192, 10^{-3}\}$, $\{1/256, 7.5 \times 10^{-4}\}$, and $\{1/384, 5 \times 10^{-4}\}$, respectively (compared to 31, 55, and 141 s for the one-disk problem).

8.5. Numerical Simulation of the Motions and Interaction of Two Balls Sedimenting in an Incompressible Viscous Fluid

The fourth test problem considered here concerns the simulation of the motions and interaction of two sedimenting identical balls in a vertical cylinder with square cross-section. The computational domain is $\Omega = (0, 1) \times (0, 1) \times (0, 4)$. The diameter d of the two balls is $1/6$ and at time $t = 0$, the centers of the two balls are located on the axis of the cylinder at $\{0.5, 0.5, 3.5\}$ and $\{0.5, 0.5, 3.1\bar{6}\}$. The initial translational and angular velocities of the balls are zero. The density of the fluid is $\rho_f = 1.0$ and the density of the balls is $\rho_s = 1.14$. The viscosity of the fluid is $\nu_f = 0.01$. The initial condition for the fluid flow is $\mathbf{u}(0) (= \mathbf{u}_0) = \mathbf{0}$ while the boundary condition is $\mathbf{u}(t) = \mathbf{0}$ on the boundary of the cylinder, $\forall t \geq 0$. The simulation

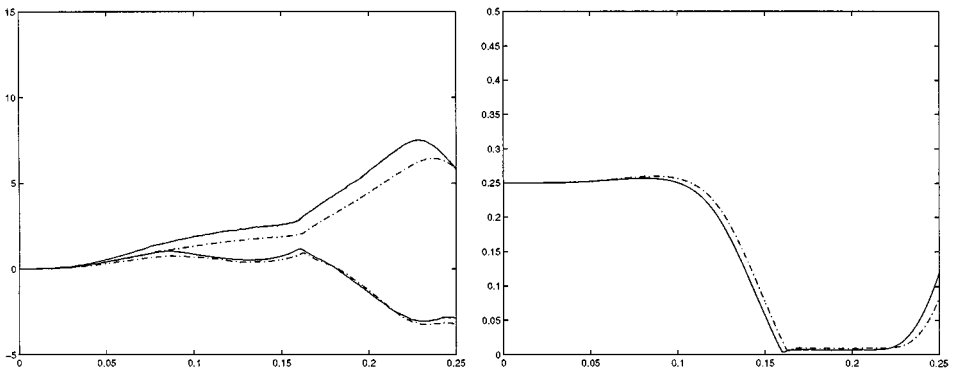


FIG. 8.15. Histories of the angular velocities of the disks (left) and of their distance (right) for $\rho_s = 1.5$ and $\nu = 10^{-2}$ ($h_\Omega = 1/256$, $\Delta t = 7.5 \times 10^{-4}$, solid lines; $h_\Omega = 1/384$, $\Delta t = 5 \times 10^{-4}$, dashed-dotted lines). Wave-like equation treatment of the advection.

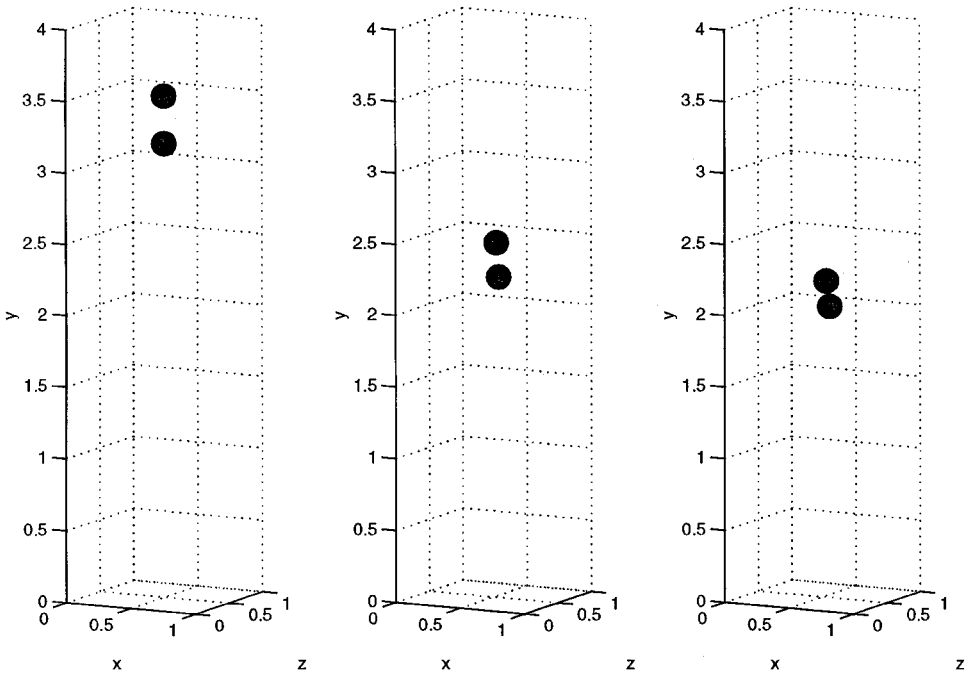


FIG. 8.16. Ball positions at $t = 0, 0.27075,$ and 0.31425 ($\rho_s = 1.14, \rho_f = 1, \nu = 10^{-2}, h_\Omega = 1/80, \Delta t = 7.5 \times 10^{-4}$).

has been done with $\{h_\Omega, \Delta t\} = \{1/60, 10^{-3}\}$ and $\{1/80, 7.5 \times 10^{-4}\}$, and $h_p = 2h_\Omega$, implying that the corresponding velocity meshes (resp., pressure meshes) have, approximately, 897,000 and 2.1×10^6 vertices (resp., 116,000 and 271,000 vertices). The advection–diffusion step has been treated by the least squares/conjugate gradient method discussed in Refs. [37, 43], while the various elliptic problems involved in our methodology have been treated by fast elliptic solvers based on cyclic reduction. Concerning the collision model, we have taken $\varepsilon = 10^{-4}$ and $\rho = 1/60$ as thickness of the safety zone. The simulation takes about 120 (resp., 304) s per time step on a DEC Alpha 500-au workstation for $\{h_\Omega, \Delta t\} = \{1/60, 10^{-3}\}$ (resp., $\{1/80, 7.5 \times 10^{-4}\}$). The maximum particle Reynolds number during the entire evolution is 111.46 (resp., 117.28) for $\{h_\Omega, \Delta t\} = \{1/60, 10^{-3}\}$ (resp., $\{1/80, 7.5 \times 10^{-4}\}$). In Figs. 8.16 and 8.17 we have visualized the positions of the balls at $t = 0, 0.27075, 0.31425, 0.45075, 0.53475,$ and 0.72975 , obtained with $\{h_\Omega, \Delta t\} = \{1/80, 7.5 \times 10^{-4}\}$; on these figures we clearly observe that the anticipated drafting, kissing, and tumbling phenomenon (Ref. [49]) is indeed taking place.

On the following Figs. 8.18 to 8.21 we have reported comparisons between quantities computed with $\{h_\Omega, \Delta t\} = \{1/60, 10^{-3}\}$ and $\{1/80, 7.5 \times 10^{-4}\}$; these figures show good agreement considering, once again, that the kissing, drafting, and tumbling phenomenon is a non-smooth one, involving several symmetry breakings.

8.6. Sedimentation of Two Disks in an Oldroyd-B Visco-elastic Fluid

8.6.1. Generalities and Synopsis

The test problem considered now is singular in the sense that it is the only one, in this article, related to fluid/rigid solid interaction when the fluid is non-Newtonian. Since we intend

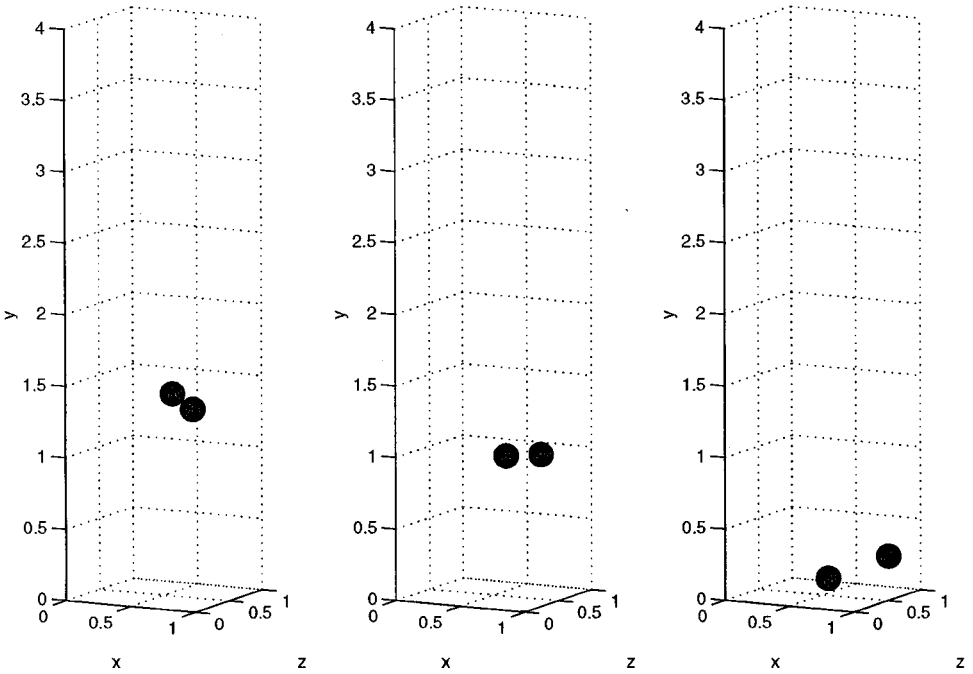


FIG. 8.17. Ball positions at $t=0.45075$, 0.53475 , and 0.72925 ($\rho_s = 1.14$, $\rho_f = 1$, $\nu = 10^{-2}$, $h_\Omega = 1/80$, $\Delta t = 7.5 \times 10^{-4}$).

to publish, in the not too far future, an article specifically dedicated to the direct numerical simulation of visco-elastic particulate flow, our “visit” to the non-Newtonian realm will be rather brief; actually, our main intention is to show some fundamental differences between the behavior of Newtonian and visco-elastic fluids when sedimentation is concerned. We consider thus the simulation of two rigid disks sedimenting in a two-dimensional cavity filled with an *Oldroyd-B visco-elastic fluid*. The equations describing the rigid body motions are as in Section 2; concerning the flow model we have to complete Equations (2.1)–(2.4)

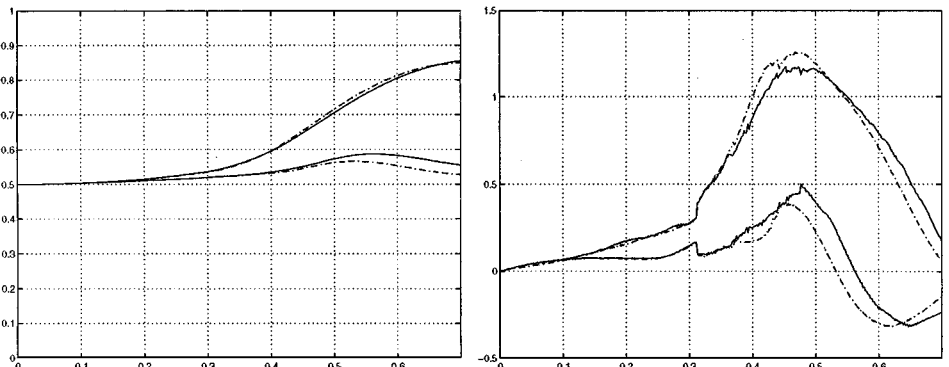


FIG. 8.18. Histories of the x -component of the ball centers (left) and of the x -component of the ball translation velocity (right) for $\rho_s = 1.14$, $\rho_f = 1$, and $\nu = 10^{-2}$ ($h_\Omega = 1/60$, $\Delta t = 10^{-3}$, solid lines; $h_\Omega = 1/80$, $\Delta t = 7.5 \times 10^{-4}$, dashed-dotted lines).

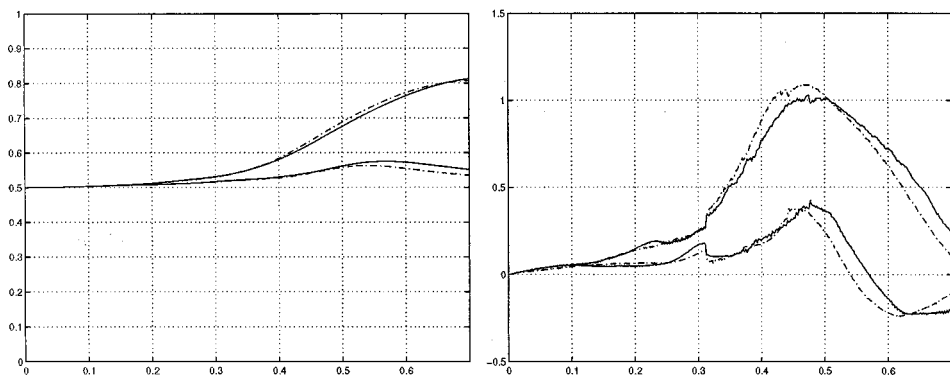


FIG. 8.19. Histories of the y -component of the ball centers (left) and of the y -component of the ball translation velocity (right) for $\rho_s = 1.14$, $\rho_f = 1$, and $\nu = 10^{-2}$ ($h_\Omega = 1/60$, $\Delta t = 10^{-3}$, solid lines; $h_\Omega = 1/80$, $\Delta t = 7.5 \times 10^{-4}$, dashed-dotted lines).

with (see [45, pp. 185–187])

$$\tau + \lambda_1 \overset{\nabla}{\tau} = 2\eta(\tau + \lambda_2 \overset{\nabla}{\mathbf{D}}(\mathbf{u})), \quad (8.1)$$

where in (8.1):

• \mathbf{A} a $d \times d$ tensor \mathbf{A} being given, $\overset{\nabla}{\mathbf{A}}$ denotes the upper convected derivative of \mathbf{A} , defined by

$$\overset{\nabla}{\mathbf{A}} = \frac{\partial \mathbf{A}}{\partial t} + (\mathbf{u} \cdot \nabla) \mathbf{A} - (\nabla \mathbf{u}) \mathbf{A} - \mathbf{A} (\nabla \mathbf{u})^t; \quad (8.2)$$

- λ_1 is the relaxation time;
- λ_2 is the retardation time;
- $\eta = (\lambda_1/\lambda_2)\nu_f$, where ν_f is the fluid viscosity,
- $\mathbf{D}(\mathbf{u}) = (\nabla \mathbf{u} + \nabla \mathbf{u}^t)/2$.

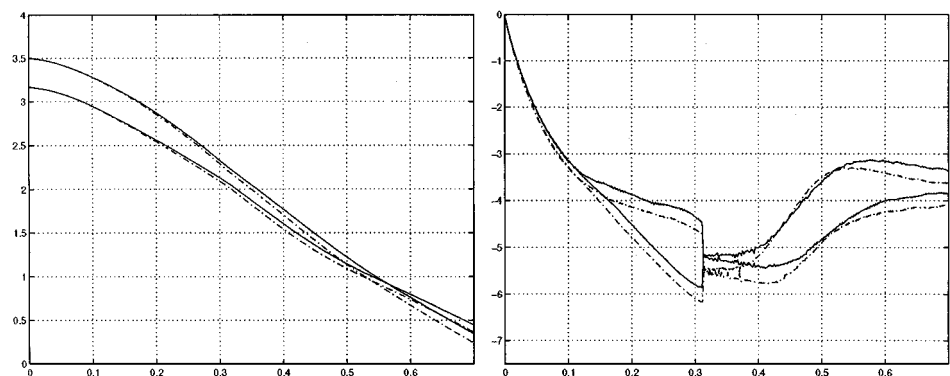


FIG. 8.20. Histories of the z -component of the ball centers (left) and of the z -component of the ball translation velocity (right) for $\rho_s = 1.14$, $\rho_f = 1$, and $\nu = 10^{-2}$ ($h_\Omega = 1/60$, $\Delta t = 10^{-3}$, solid lines; $h_\Omega = 1/80$, $\Delta t = 7.5 \times 10^{-4}$, dashed-dotted lines).

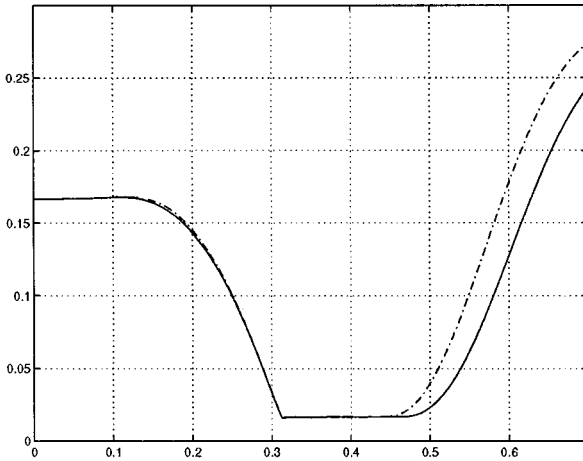


FIG. 8.21. History of the distance between the two balls for $\rho_s = 1.14$, $\rho_f = 1$, and $\nu = 10^{-2}$ ($h_\Omega = 1/60$, $\Delta t = 10^{-3}$, solid lines; $h_\Omega = 1/80$, $\Delta t = 7.5 \times 10^{-4}$, dashed-dotted lines).

Generalizing the splitting scheme (7.4)–(7.19) to accommodate the additional relation (8.1) is not difficult; we can, in particular, use the wave-like equation approach discussed in Section 7.3 to treat the advection term $\partial\tau/\partial t + (\mathbf{u} \cdot \nabla)\tau$ occurring in (8.1) (from (8.2)) and apply a time stepping method to the resulting problem (this approach was followed in Ref. [39]).

Remark 8.1. Detailed discussions on the modeling and simulation of the *flow of visco-elastic liquids* can be found in Refs. [50, 51]; see also the many references therein.

8.6.2. Formulation of the Test Problem and Numerical Results

As already mentioned, this fifth test problem is concerned with the direct simulation of the sedimentation of two rigid disks in a two-dimensional cavity filled with an Oldroyd-*B* visco-elastic fluid. The computational domain is $\Omega = (0, 2) \times (0, 6)$. The initial condition for the fluid velocity field is $\mathbf{u}(0)(=\mathbf{u}_0) = \mathbf{0}$. The boundary condition for the velocity is $\mathbf{u}(t) = \mathbf{0}$ on Γ , $\forall t \geq 0$. The density of the fluid is $\rho_f = 1$ and the viscosity is $\nu_f = 0.25$. The relaxation time is $\lambda_1 = 1.4$, while the retardation time is $\lambda_2 = 0.7$. The diameter of the disks is $d = 0.25$, while their density is $\rho_s = 1.01$. The initial translation and angular velocities of the disks are zeros. At time $t = 0$, the centers of the two disks are located on the vertical symmetry axis of the cavity at $\{1, 5.25\}$ and $\{1, 4.75\}$. In the simulation, the mesh size for the velocity field $h_\Omega = 1/128$; it is $h_p = 2h_\Omega = 1/64$ for the pressure and $h_\tau = h_\Omega = 1/128$ for the stress tensor τ . The time step is $\Delta t = 10^{-3}$. We let the two disks fall in the cavity. Before touching the bottom, we can see in Fig. 8.22 the fundamental features of a pair of identical disks sedimenting in an Oldroyd-*B* viscoelastic fluid, namely a drafting, kissing, and chaining phenomenon (see [52] for more details). The averaged terminal velocity is 0.29 in this simulation, implying that the corresponding

- Deborah number is $De = 1.624$
- Reynolds number is $Re = 0.29$
- Visco-elastic Mach number is $M = 0.686$
- Elasticity number is $E = 5.6$

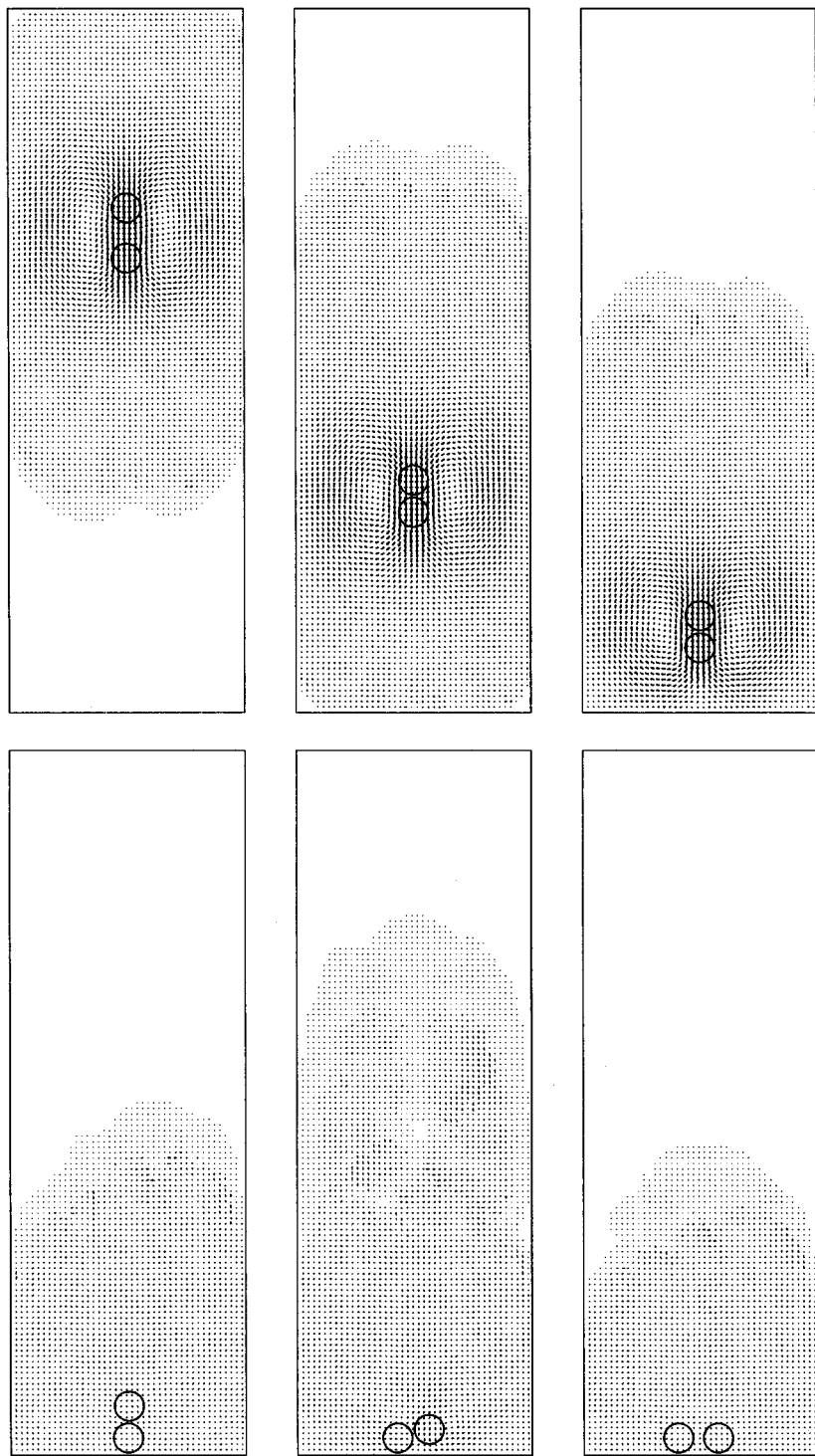


FIG. 8.22. Sedimentation and chaining of two disks in an Oldroyd-B viscoelastic fluid at $t = 3, 11, 15, 18, 22.5,$ and 27 (from left to right and from top to bottom).

(see, e.g., Ref. [51] for a precise definition of De , M , and E). The simulation has been done using the wave-like equation approach, discussed in Section 7.3, to treat the advection of \mathbf{u} and τ .

8.7. Direct Numerical Simulation of Incompressible Viscous Flow around Moving Airfoils

8.7.1. Motivation and Synopsis

The rigid bodies considered so far have been circular disks or spherical balls. Another salient feature of the previous test problems and simulations has been that the rotational kinetic energy was always small compared to the translational kinetic energy. The main goals of the following two test problems are:

(i) To show that the computational methods discussed in Sections 4 to 7 apply (at least in 2-D) to rigid bodies of shape more complicated than disks and balls.

(ii) To show that the above methods apply when the rotational kinetic energy is comparable, or even larger, to the translational one and still can bring accurate results.

The following test problems concern flow around one or several NACA0012 airfoils.

8.7.2. Flow around a NACA0012 Airfoil with Fixed Center of Mass

We consider here an incompressible viscous flow around a NACA0012 airfoil that has a *fixed* center of mass and is *free to rotate* due to hydrodynamical forces; the surrounding region Ω is the rectangle $(-4, 16) \times (-2, 2)$. The characteristic length, namely the airfoil length, is 1.009 and the fixed center of mass of the airfoil is at $(0.42, 0)$. Initial angular velocity and incident angle are zero. The density of the fluid is $\rho_f = 1$ and the density of the airfoil is $\rho_s = 1.1$. The viscosity of the fluid is $\nu_f = 10^{-2}$. The initial condition for the fluid flow is $\mathbf{u}(0)(=\mathbf{u}_0) = 0$ and the boundary data \mathbf{g}_0 is given by

$$\mathbf{g}_0(\mathbf{x}, t) = \begin{cases} \mathbf{0} & \text{if } x_2 = -2 \text{ or } 2, \\ (1 - e^{-50t}) \begin{pmatrix} 1 \\ 0 \end{pmatrix} & \text{if } x_1 = -4 \text{ or } 16, \end{cases}$$

for $t \geq 0$. Hence the Reynolds number is about 101 with respect to the length of the airfoil and the maximum inflow speed. For this test problem we have chosen two sets $\{h_\Omega, \Delta t\}$ of discretization parameters, namely $\{1/64, 1.5 \times 10^{-3}\}$ and $\{1/96, 10^{-3}\}$, to validate the simulation results; the mesh size for pressure is, again, $h_p = 2h_\Omega$. We have thus, approximately, 330,00 and 740,000 velocity vertices for the triangulations used to approximate the velocity.

To enforce the rigid body motion inside the airfoil at each time step, using the multiplier space defined by (6.16), we have taken all the grid points from the velocity mesh contained in the airfoil at that time completed by a selected set of points belonging to the boundary of the airfoil (and containing the trailing edge; see Fig. 8.23) and then used as scalar product over $\Lambda_h(t)$ the one defined by (6.6).

For these rotating airfoil simulations, we have used the previously mentioned least squares/conjugate gradient technique to solve the advection-diffusion subproblems. The NACA0012 airfoil is fixed up to $t = 1$. A steady flow around it is obtained. After $t = 1$, we allow the NACA0012 airfoil to rotate freely. In Fig. 8.24, we observe that the histories

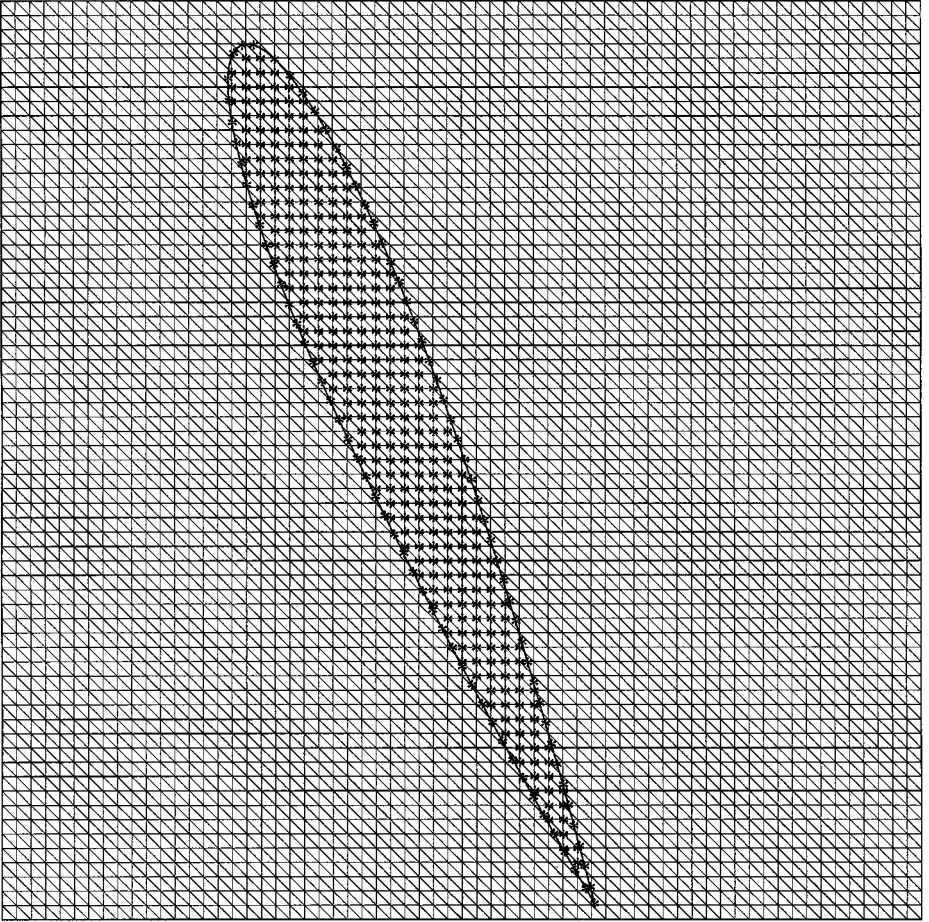


FIG. 8.23. Part of the velocity mesh and example of mesh points used in (6.16) to enforce the rigid body motion inside the NACA0012 airfoil.

corresponding to the two sets $\{h_\Omega, \Delta t\}$ are in very good agreement. The airfoil intends to keep its broadside perpendicular to the in-flow direction which is a stable position for non-circular particles settling in a channel at small Reynolds numbers (cf. Ref. [53]) and it quickly reaches a periodic motion.

The CPU/time step is 53 s (resp., 107 s if $\{h_\Omega, \Delta t\} = \{1/64, 1.5 \times 10^{-3}\}$ (resp., $\{1/96, 10^{-3}\}$) on one node of an IBM SP2. The same methodology has been (successfully) applied to the more challenging case where $v_f = 1.25 \times 10^{-3}$ (i.e., $\text{Re} = 807$) the other data and parameters staying the same. The corresponding results are discussed in [6, Sect. 6].

Remark 8.2. For the test case discussed here the fact that we used a fine uniform mesh may appear as a drawback. Actually, this test problem was considered for validation purposes and also to show that our methodology can handle non-circular bodies. Also, when simulating the flow of mixtures with over 100 particles highly dispersed in the flow region (see the test problems in Sections 8.8 and 8.9), which is the main goal of the distributed Lagrange multiplier method discussed here, using a fine uniform mesh everywhere is not a drawback

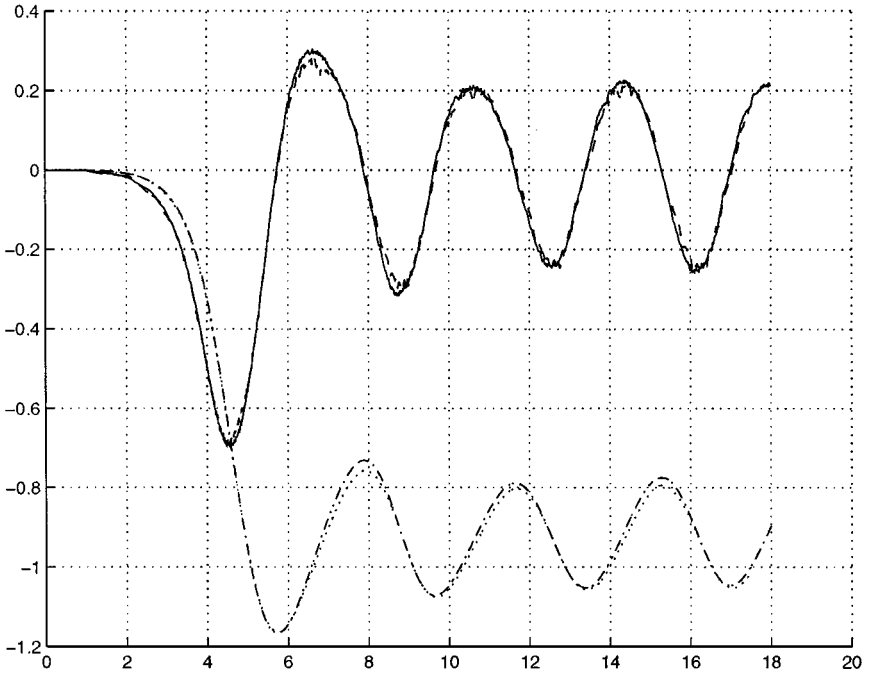


FIG. 8.24. Histories of the angle ($h_{\Omega} = 1/64$, $\Delta t = 1.5 \times 10^{-3}$, dotted line; $h_{\Omega} = 1/96$, $\Delta t = 10^{-3}$, dashed-dotted line) and of the angular velocity ($h_{\Omega} = 1/64$, $\Delta t = 1.5 \times 10^{-3}$, dashed line; $h_{\Omega} = 1/96$, $\Delta t = 10^{-3}$, solid line). The measures are in rad and rad/s.

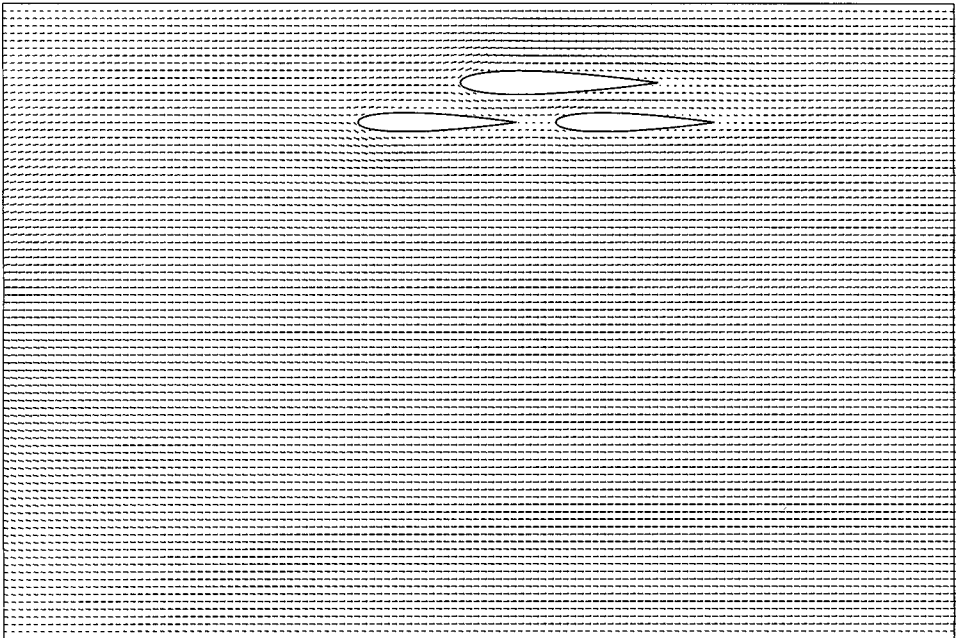


FIG. 8.25. Flow visualization at $t = 1$.

anymore (particularly for a flow where the ratio *solid volume/fluid volume* is of the order of one or more).

Of course—as in [54]—one can combine locally adapted mesh with boundary Lagrange multiplier in order to avoid using fine mesh everywhere. One can also use unstructured meshes and force the rigid body motion by collocation like the one done in [22].

Remark 8.3. For the above test problem, we have imposed $\mathbf{u} = 0$ on the top and bottom boundaries of Ω . Actually, with the methodology discussed in this article, there would

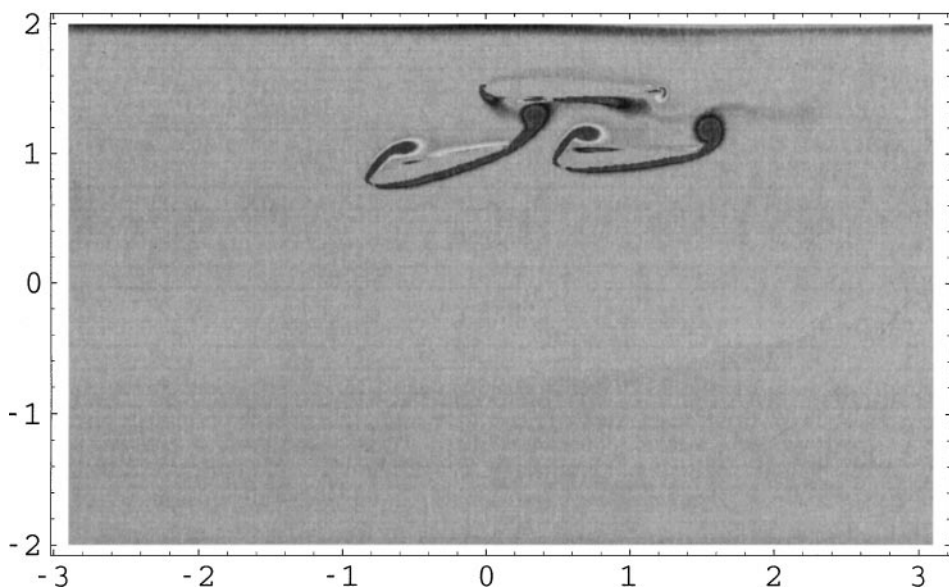
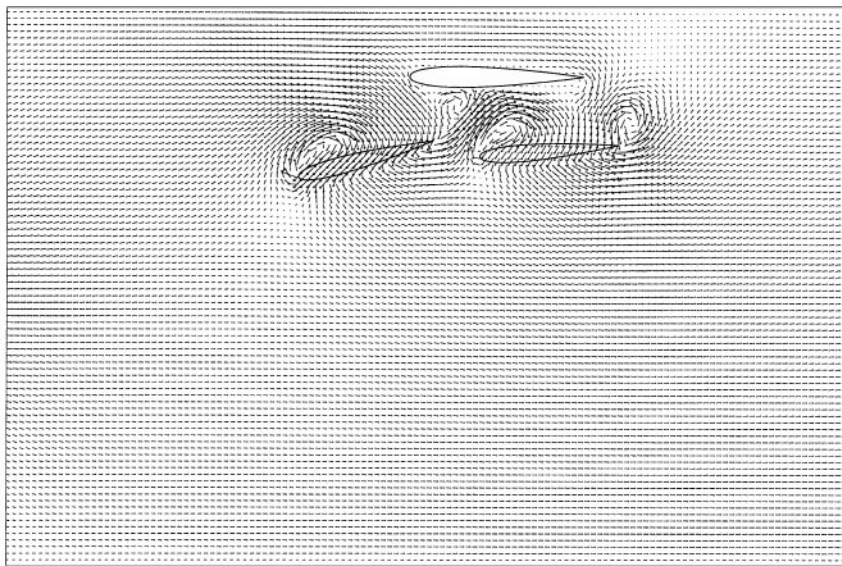


FIG. 8.26. Flow visualization (top) and vorticity density (bottom) at $t = 1.3$.

have been no problem imposing $\mathbf{u} = \mathbf{u}_\infty (\neq \mathbf{0})$ on the inflow, top and bottom boundaries of Ω and $\nu_f(\partial\mathbf{u}/\partial n) - \mathbf{n}p = \mathbf{0}$ (or $\sigma\mathbf{n} = \mathbf{0}$) on the outflow boundary. We can justify the boundary conditions used here by the fact that the experimental results concerning flow around cylinders are obtained by putting the cylinders in channels where they are fixed or free to rotate, the boundary conditions on the boundary of the channel being close to those used in this article.

Remark 8.4. Using the parallelization techniques discussed in [46], the computational times given above have been divided by factors of the order of 10 (see [46] for details).

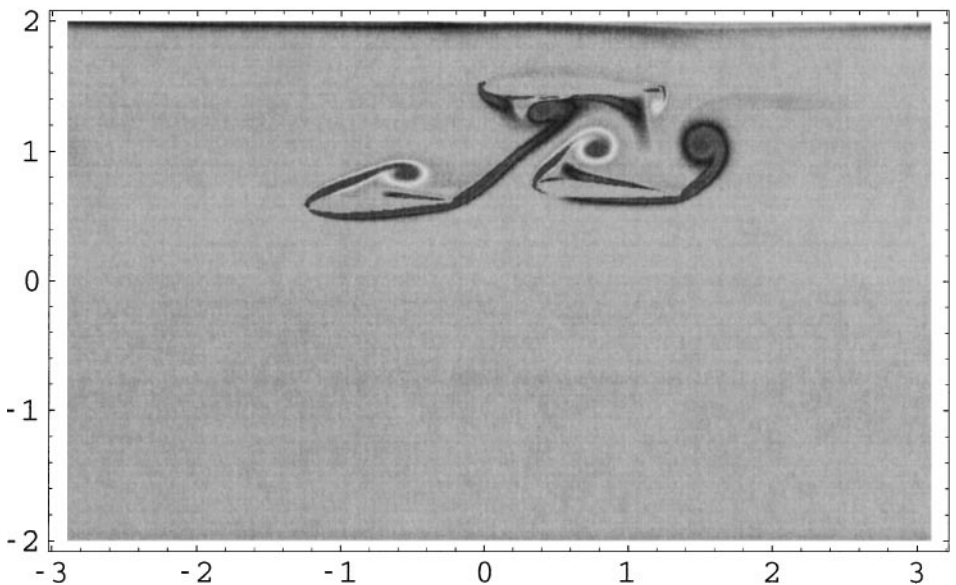
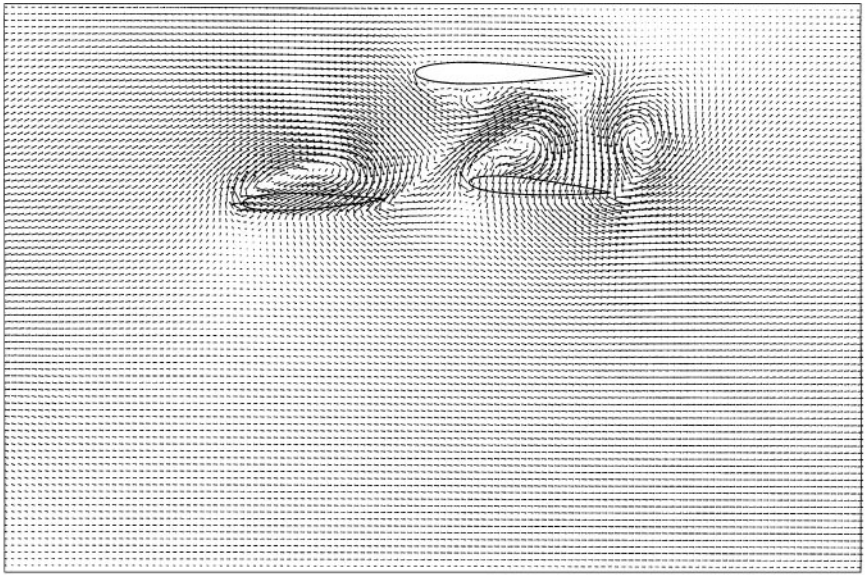


FIG. 8.27. Flow visualization (top) and vorticity density (bottom) at $t = 1.5$.

8.7.3. Simulation of a Two-Dimensional Multi-store Separation Phenomenon

The main goal of this test problem is the direct numerical simulation of a multi-store separation phenomenon in two-dimensions. A more precise description of the problem is as follows: several bodies, rigidly attached up to some time t_* , are located in a space region containing an incompressibly Newtonian viscous fluid; at time $t = t_*$, some of the bodies are released and are going to fall under the effect of gravity. Our goal is to simulate the motion of the various bodies and the flow they induce when moving down. The computational domain is $\Omega = (-4, 12.047) \times (-2, 2)$. The boundary conditions verified by $\mathbf{u}(t)$ on the

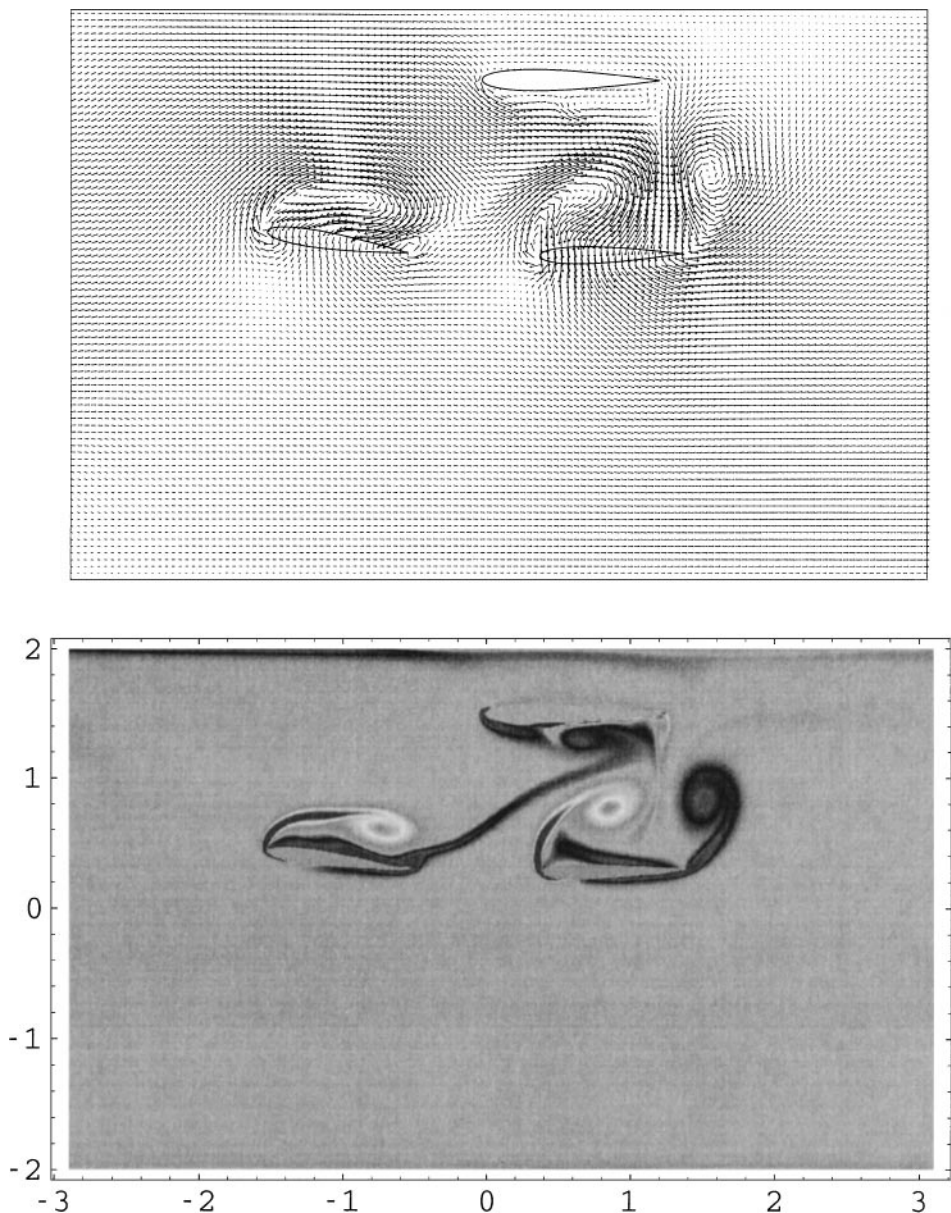


FIG. 8.28. Flow visualization (top) and vorticity density (bottom) at $t = 1.75$.

boundary Γ of Ω are defined by

$$\mathbf{u}(x, t) = \begin{cases} \mathbf{0} & \text{for } x_2 = \pm 2, x_1 \in [-4, 12.047], \\ (1 - e^{-50t})(1 - x_2^2/4) \begin{pmatrix} 1 \\ 0 \end{pmatrix} & \text{for } x_1 = -4 \text{ or } 12.047 \text{ and } |x_2| \leq 2. \end{cases}$$

The initial condition for the velocity is $\mathbf{u}(0)(=\mathbf{u}_0) = \mathbf{0}$. We suppose that the rigid bodies are three NACA0012 airfoils, two of them of length 1 and the third of length 1.25. At time $t = 0$ the centers of mass of the airfoils are located at $\{0.5, 1.5\}$ for the large one and at $\{-0.25, 1.25\}$ and $\{1, 1.25\}$ for the two smaller ones (see Fig. 8.25). The airfoils

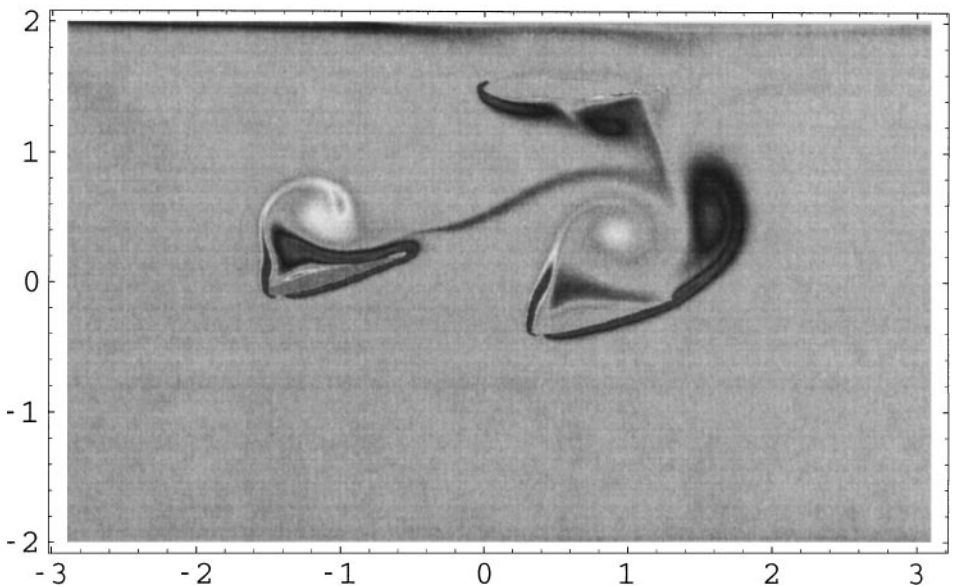


FIG. 8.29. Flow visualization (top) and vorticity density (bottom) at $t = 2$.

are at rest at $t = 0$. The two smaller airfoils are released at $t = t_* = 1$ and start moving down under the effect of gravity; the largest one is supposed fixed. The fluid density is $\rho_f = 1$ while the fluid viscosity is $\nu_f = 10^{-3}$, implying that the moving airfoils' Reynolds number is 10^3 . The moving airfoils' density is $\rho_s = 1.1$. The methods of Sections 4 to 7 have been applied (without collision model) to the simulation of the above separation phenomenon. We have used $h_\Omega = 2/225$ to discretize the velocity, $h_p = 2h_\Omega$ to discretize the pressure, and $\Delta t = 5 \times 10^{-4}$ for the time discretization. We have thus about 10^6 velocity grid points and 250,000 pressure grid points. The advection–diffusion has been treated by a least-squares/conjugate gradient method.

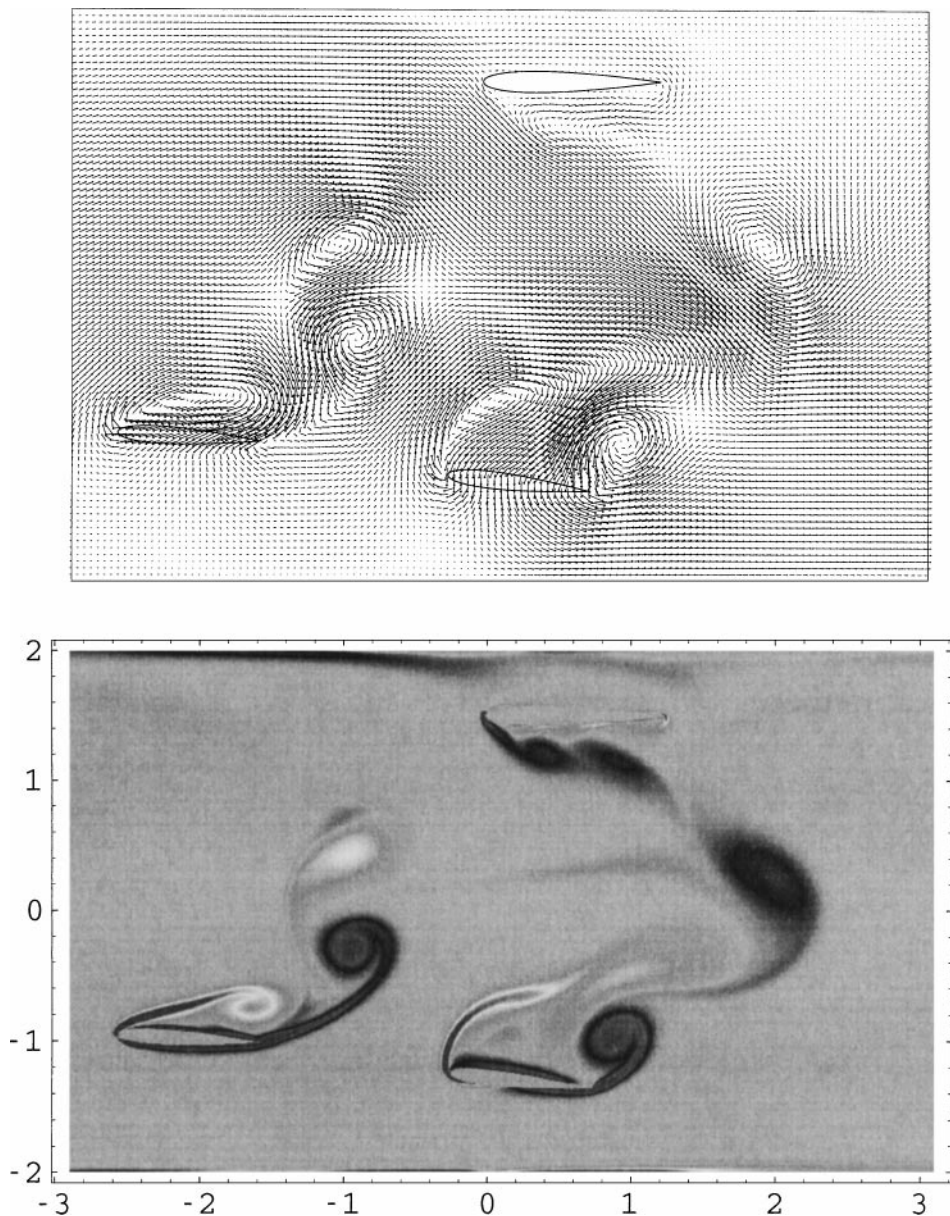


FIG. 8.30. Flow visualization (top) and vorticity density (bottom) at $t = 2.5$.

In Fig. 8.25 we have visualized the flow at $t = 1$ (just before the release of the two small airfoils), while in Figs. 8.26 to 8.30 we have visualized the flow velocity and the vorticity distribution at $t = 1.3, 1.5, 1.75, 2$ and 2.5 .

The computational time for this test problem is 51 sec./time step on 4 nodes of an SGI Origin 2000 parallel computer.

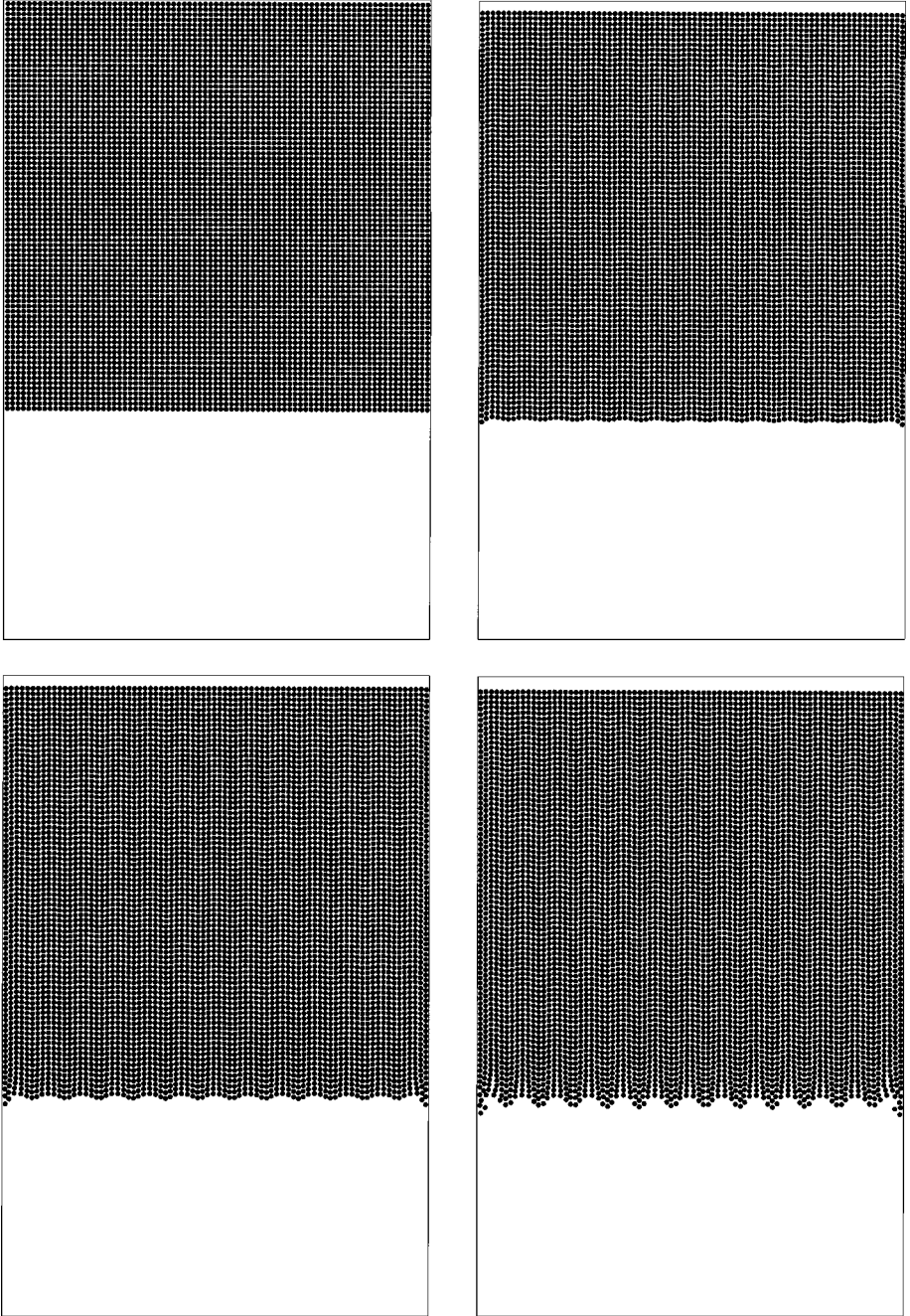


FIG. 8.31. Sedimentation of 6400 particles: positions at $t = 0, 0.4, 0.5, 0.6$ (from left to right and from top to bottom), and visualization of the Rayleigh–Taylor instability.

8.8. Sedimentation of 6,400 Circular Particles in a Two-Dimensional Cavity: Rayleigh–Taylor Instability for Particulate Flow

8.8.1. Generalities and Synopsis

The test problems discussed in this section, and in the following Section 8.9, differ significantly from the ones considered so far. The main difference lies with the much larger

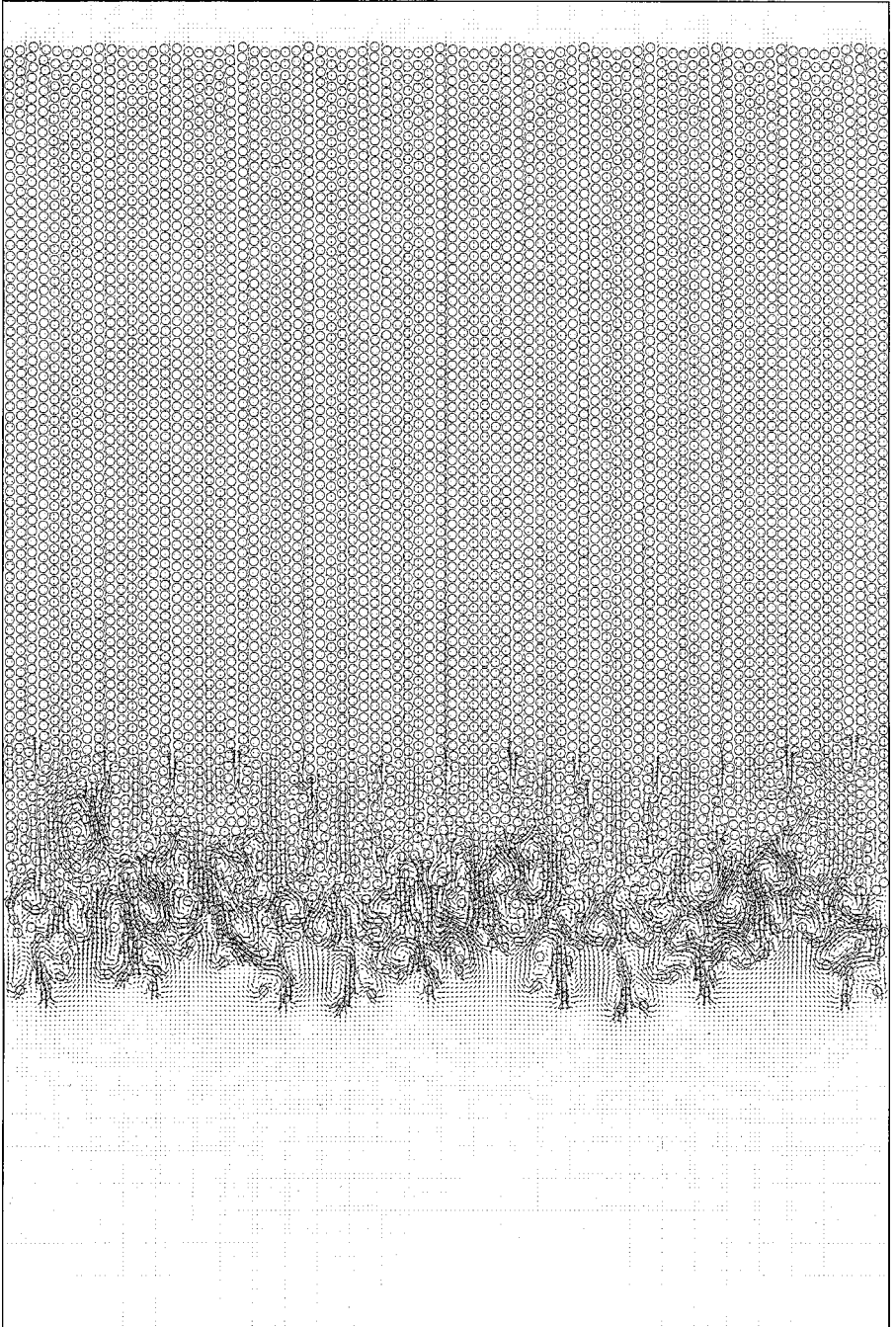


FIG. 8.32. Sedimentation of 6400 particles: $t = 1$.

numbers of rigid bodies (particles, indeed) that we are going to consider, these numbers being over 10^3 . Indeed, these test problems can be viewed as particulate flow problems and we shall see that the computational methods discussed in Sections 4 to 7 apply to those more challenging situations.



FIG. 8.33. Sedimentation of 6400 particles: $t = 2.6$.

The specific problem discussed in this section concerns the sedimentation of 6,400 disks settling down in a rectangular cavity filled with an incompressible Newtonian viscous fluid. In Section 8.9 we shall discuss the fluidization of 1,204 spherical particles in a three-dimensional tube (bed). Since several articles specifically dedicated to the above test



FIG. 8.34. Sedimentation of 6400 particles: $t = 3$.

problems are in preparation, their discussion in this review article will be shorter than the one they really deserve.

For a review of the many aspects of particulate flow we refer to [55] (and to the many references therein).

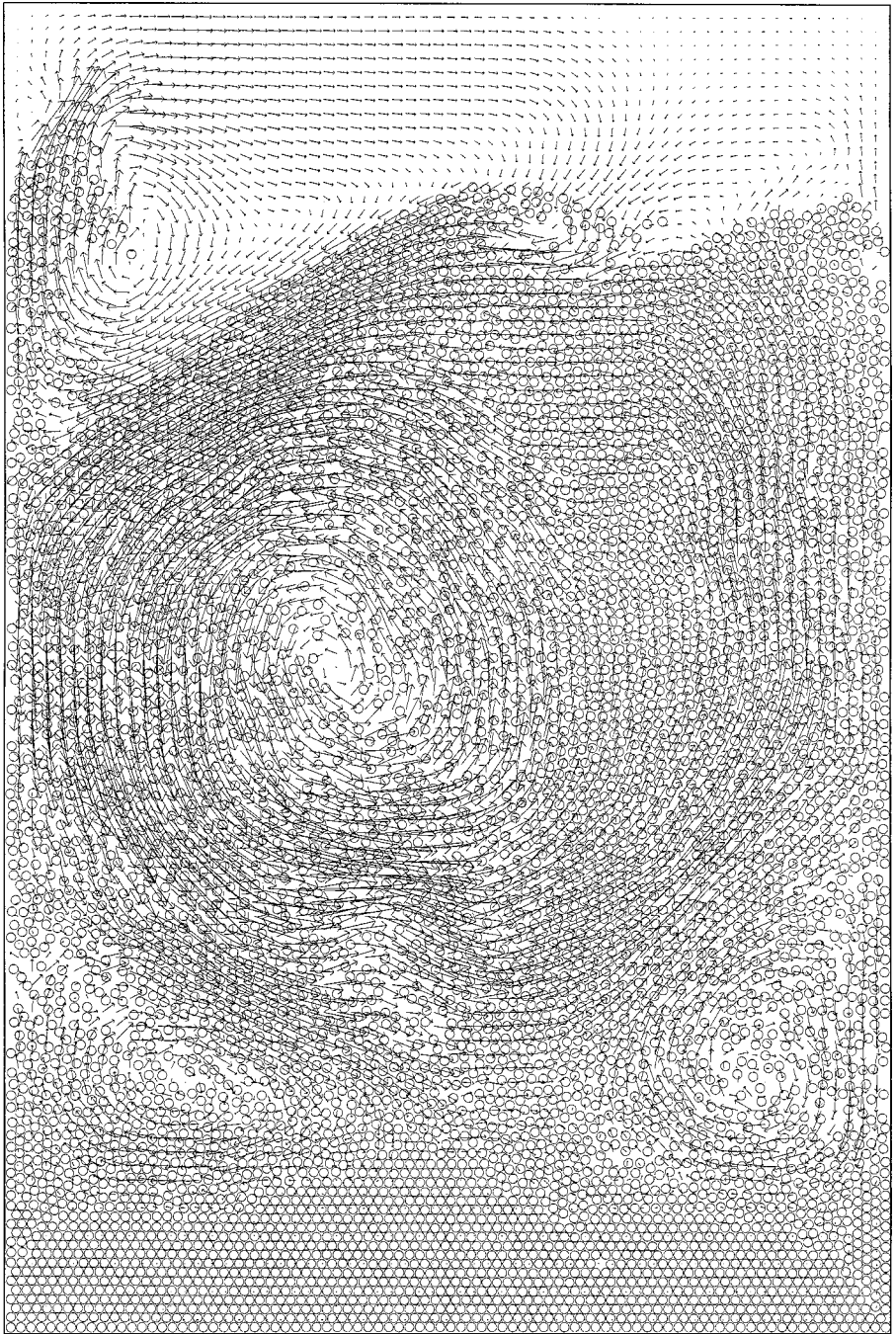


FIG. 8.35. Sedimentation of 6400 particles: $t = 5$.

8.8.2. Formulation of the Test Problem and Numerical Results

The test problem that we consider now concerns the simulation of the motion of 6,400 sedimenting circular disks in the closed cavity $\Omega = (0, 8) \times (0, 12)$. The diameter d of the disks is $1/12$ and the position of the disks at time $t = 0$ is shown in Fig. 8.31. The solid

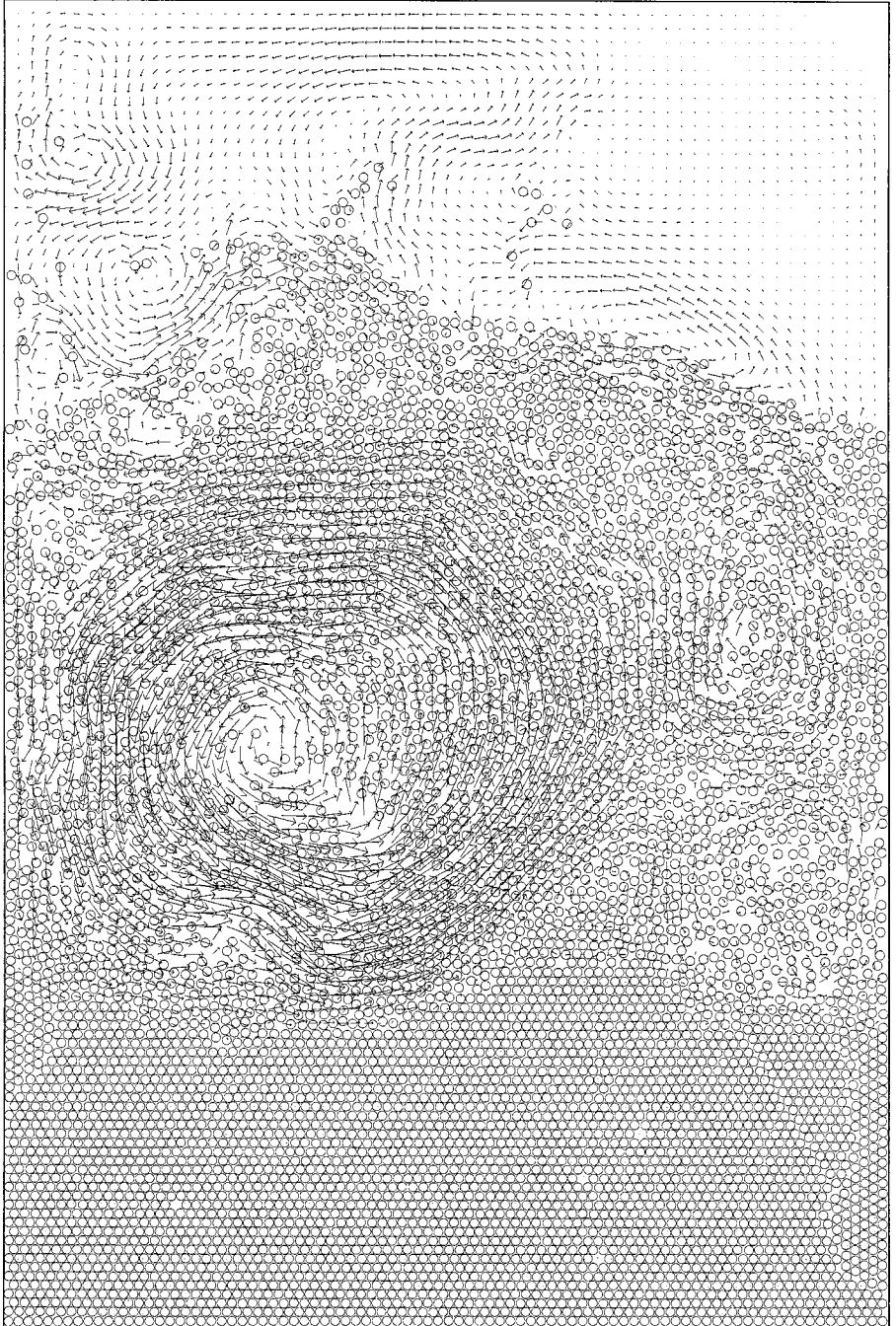


FIG. 8.36. Sedimentation of 6400 particles: $t = 7$.

fraction in this test case is 34.9%. The disks and the fluid are at rest a time $t = 0$. The density of the fluid is $\rho_f = 1$ and the density of the disks is $\rho_s = 1.1$. The viscosity of the fluid is $\nu_f = 10^{-2}$. The time step is 10^{-3} . The mesh size for the velocity field is $h_\Omega = 1/192$ (the velocity triangulation has thus about 3.5×10^6 vertices) while the pressure mesh size is $h_p = 2h_\Omega$, implying approximately 885,000 vertices for the pressure triangulation. For

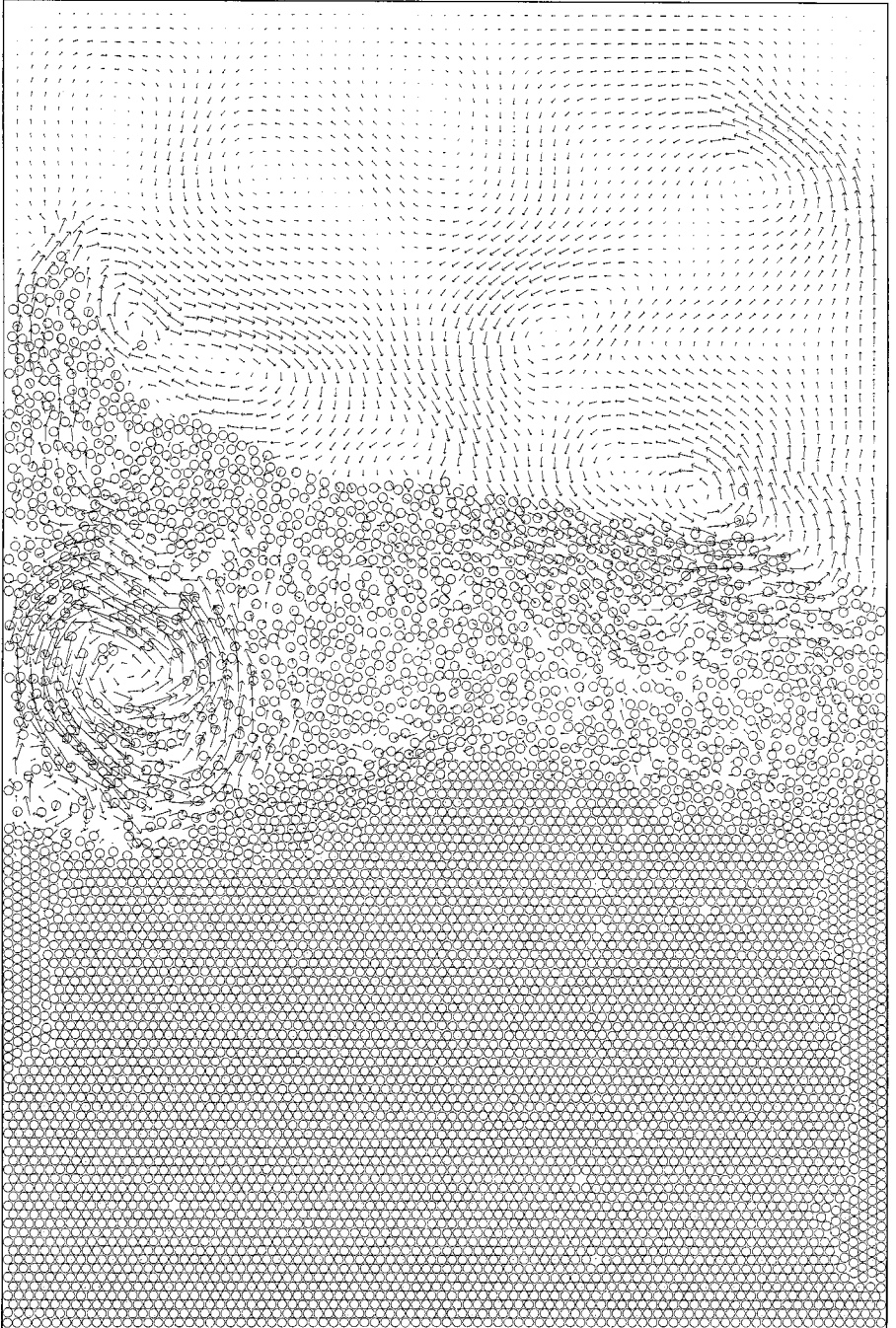


FIG. 8.37. Sedimentation of 6400 particles: $t = 9$.

this test problem where many particles “move around” a fine mesh is required essentially everywhere. The wave-like equation approach has been chosen to treat the advection, the parameter ε occurring in the collision model has been taken equal to 10^{-6} , while for the thickness ρ of the safety zone we have used $\rho = 2h_{\Omega}$. The computational time per time step is approximately 10 min on a DEC Alpha 500-au workstation, implying that to simulate



FIG. 8.38. Sedimentation of 6400 particles: $t = 11$.

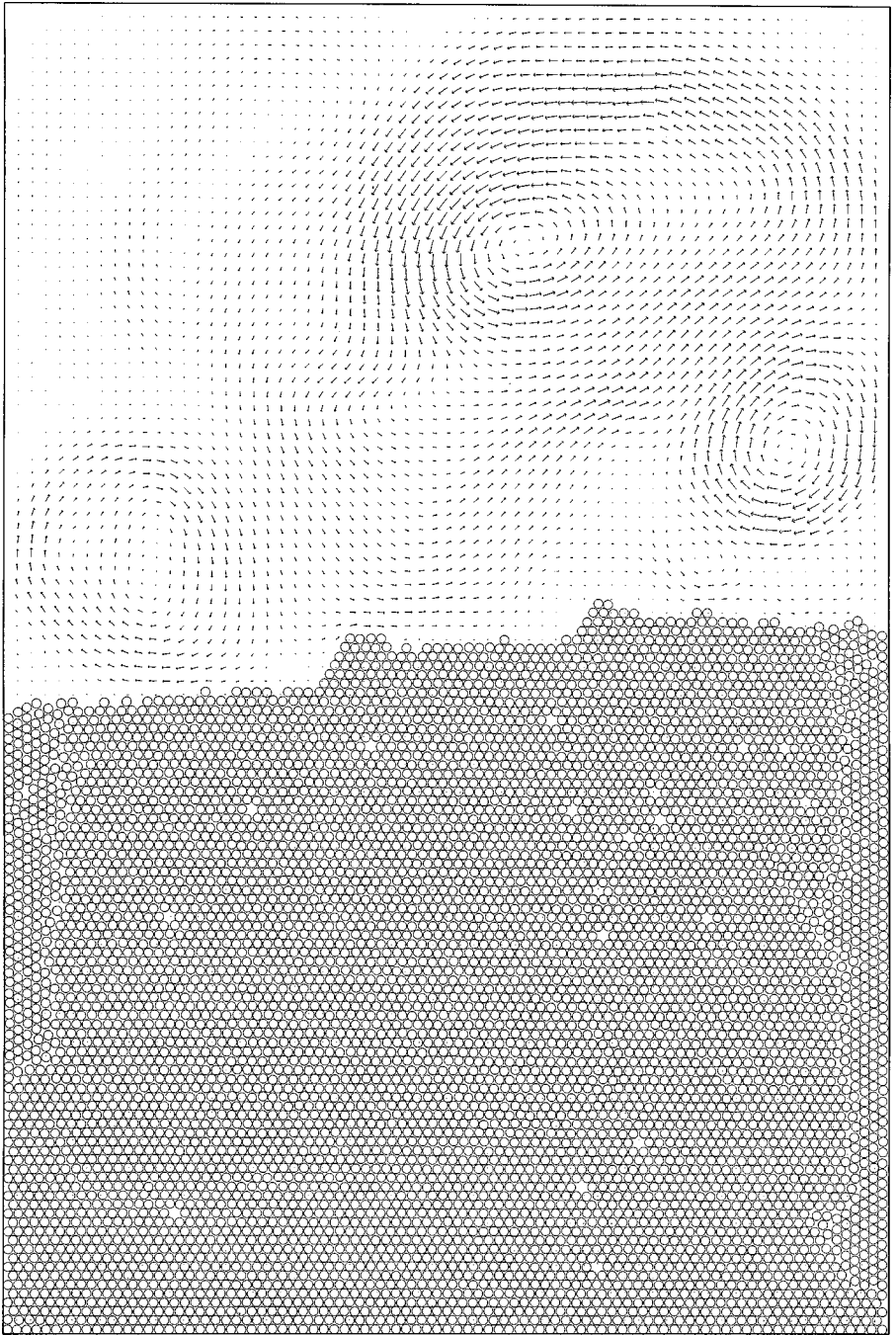


FIG. 8.39. Sedimentation of 6400 particles: $t = 13$.

one time unit of the phenomenon under consideration *we need, practically, a full week*. The evolution of the 6,400 disks sedimenting in Ω is shown in Figs. 8.31 to 8.39. The maximum particle Reynolds number in the entire evolution is 72.64. Figure 8.31 clearly shows the development of a “text-book” *Rayleigh–Taylor instability*. This instability develops into a fingering phenomenon and many symmetry breaking and other bifurcation phenomena,

including drafting, kissing, and tumbling, take place at various scales and times; similarly vortices of various scales develop and for a while the phenomenon is clearly chaotic, which is not surprising after all for a 6400-body problem. Finally, the particles settle at the bottom of the cavity and the fluid returns to rest.

Actually, the authors of the present article are currently preparing another one where it will be shown that the analytical theory of Rayleigh–Taylor instabilities, when applied to the situation prevailing here at $t = 0$, predicts a behavior of the mixture for $0 \leq t \leq 1$ very close, quantitatively, to that directly simulated via the computational techniques discussed in this article.

Remark 8.5. In the above calculation we have assumed that the disks have identical diameter d and density ρ_s ; in fact the methods discussed in this article can handle those situations where diameters and densities (and even shapes) differ.

8.9. Fluidization of a Bed of 1,204 Spherical Particles

We consider here the simulation of fluidization in a bed of 1204 spherical particles. The computational domain is $\Omega = (0, 0.6858) \times (0, 20.3997) \times (0, 44.577)$. The thickness of

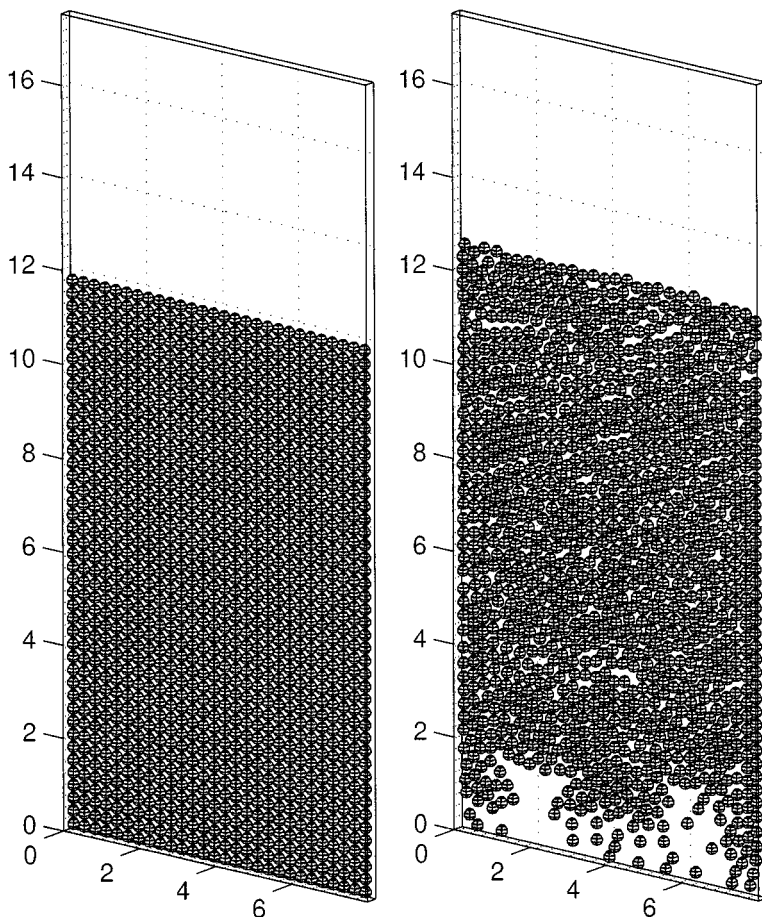


FIG. 8.40. Fluidization of 1204 spherical particles: positions of the particles at $t = 0$ and 1.5.

this bed is slightly larger than the diameter of the particles, which is $d = 0.635$, so there is only one layer of balls in the $0x_2$ direction. In [49] many experimental results related to this type of “almost two-dimensional” beds are presented. The fluid is incompressible, viscous, and Newtonian; its density is $\rho_f = 1$ and its viscosity is $\nu_f = 10^{-2}$. We suppose that at $t = 0$ the fluid and the particles are at rest. The boundary condition for the velocity field is

$$\mathbf{u}(t) = \begin{cases} 0 & \text{on the four vertical walls,} \\ 5 \begin{pmatrix} 0 \\ 0 \\ 1 - e^{-50t} \end{pmatrix} & \text{on the two horizontal walls.} \end{cases}$$

The density of the balls is $\rho_s = 1.14$. We suppose that the fluid can enter and leave the bed but that the balls have to stay in it; i.e., they cannot cross $\Gamma (= \partial\Omega)$ to leave the bed. The mesh size for the velocity field is $h_\Omega = 0.06858$ (corresponding to 2×10^6 vertices for the velocity mesh), while it is $h_p = 2h_\Omega$ for the pressure (corresponding to 2.9×10^5 vertices for the pressure mesh). The time step is $\Delta t = 10^{-3}$. The parameter ε used in the collision model is 5×10^{-7} and we take $\rho = h_\Omega$ as the thickness of the safety zone

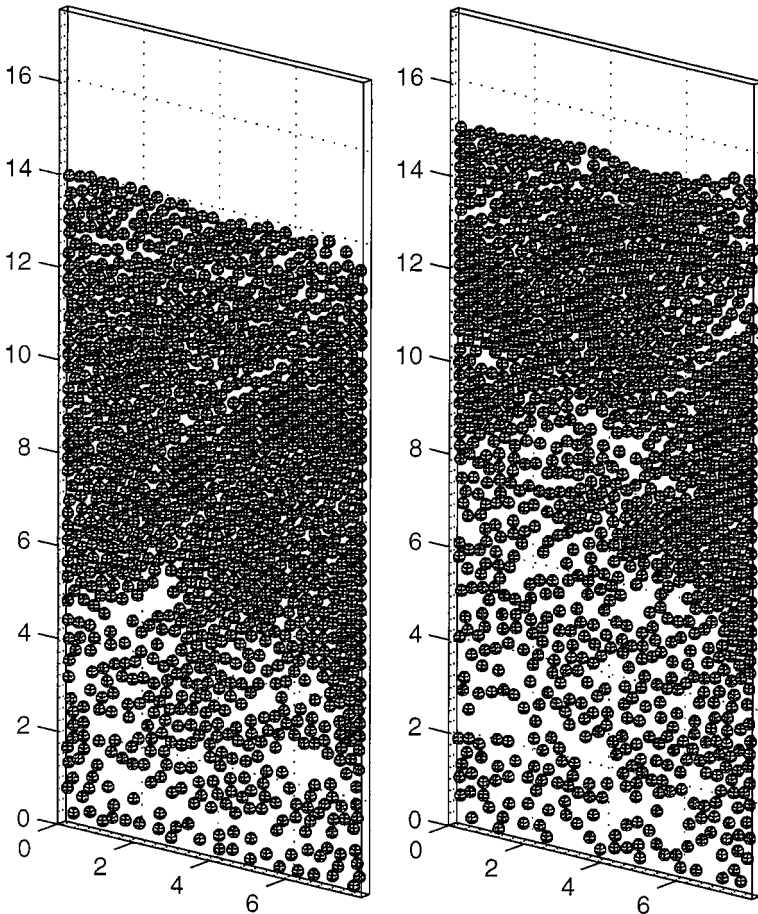


FIG. 8.41. Fluidization of 1204 spherical particles: positions of the particles at $t = 3$ and 4.5 .

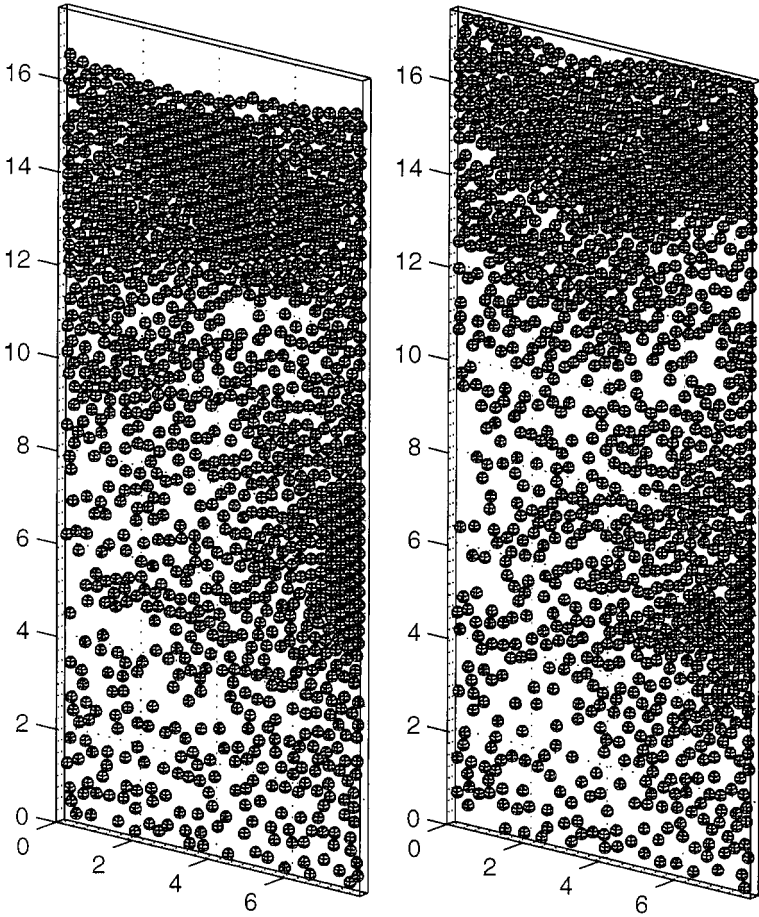


FIG. 8.42. Fluidization of 1204 spherical particles: positions of the particles at $t = 6$ and 7 .

around each particle. The initial position of the balls is shown in Fig. 8.40. After we begin pushing the balls up, we observe that the inflow creates cavities propagating among the balls in the bed. Since the inflow velocity is much higher than the critical fluidization velocity (of order 2.5 here), many balls are pushed directly to the top of the bed. Those balls at the top of the bed are stable and closely packed while the others are circling around at the bottom of the bed. These numerical results are very close to experimental ones and have been visualized in Figs. 8.40 to 8.43. In the simulation, the maximum particle Reynolds number is 1512 while the maximum averaged particle Reynolds number is 285. The computations were done on an SGI Origin 2000, using a partially parallelized code; the computational time is approximately 110 s/time step. The advection–diffusion has been treated by a least-squares/conjugate gradient.

The authors of this article are currently preparing an article specifically dedicated to the above simulations; it will contain comparisons between the results obtained by direct numerical simulation and the experimental ones measured in the laboratory of the fourth author at the University of Minnesota.

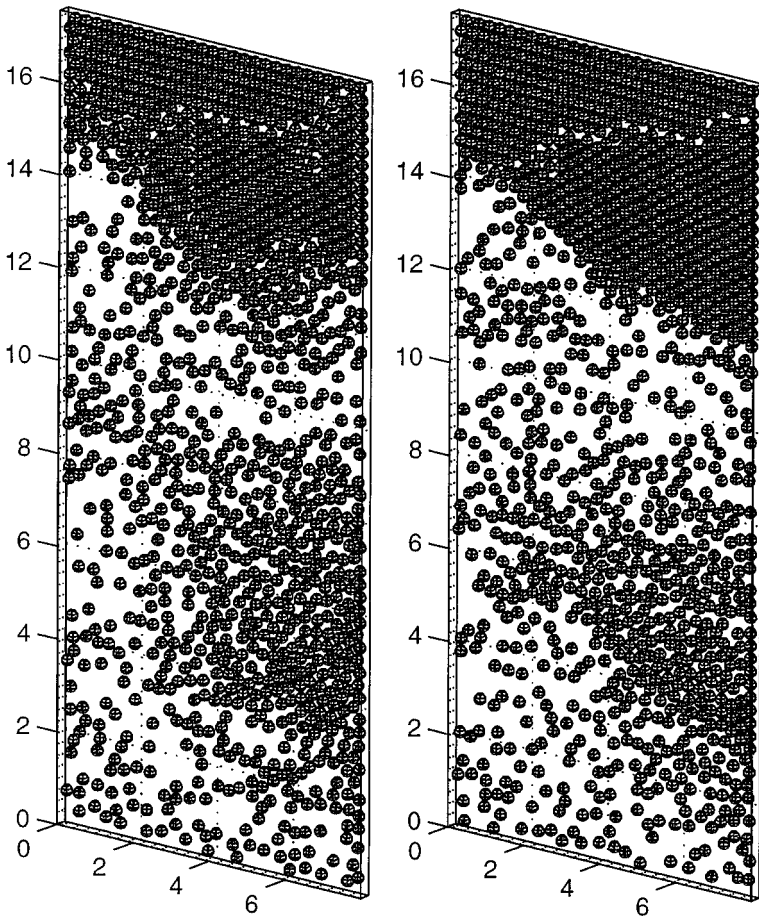


FIG. 8.43. Fluidization of 1204 spherical particles: positions of the particles at $t = 8$ and 10.

9. CONCLUSION

We have presented in this article a distributed Lagrange-multiplier-based fictitious domain methodology for the simulation of flow with moving boundaries. This novel methodology allows the *direct numerical simulation* of fairly complicated phenomena such as particulate flow, including sedimentation and fluidization. Other goals include:

- 3-D particulate flow with large numbers of particles of different sizes, shapes, and densities;
- particulate flow for viscoelastic liquids, such as Oldroyd-B.

ACKNOWLEDGMENTS

We acknowledge the helpful comments and suggestions of E. J. Dean, V. Girault, J. He, Y. Kuznetsov, Yong-Jun Lin, G. Rodin, A. Sameh, V. Sarin, and P. Singh, and also the support of the Supercomputing Institute at the University of Minnesota concerning the use of an SGI Origin 2000. We acknowledge also the support of the NSF (Grants ECS-9527123, CTS-9873236, and DMS-9973318) and Dassault Aviation. The assistance of P. Muscarello is also acknowledged.

REFERENCES

1. H. H. Hu, N. A. Patankar, and M. Y. Zhu, Direct numerical simulations of fluid–solid systems using Arbitrary-Lagrangian-Eulerian technique, *J. Comput. Phys.*, this issue.
2. R. Glowinski, T. I. Hesla, D. D. Joseph, T. W. Pan, and J. Periaux, Distributed Lagrange multiplier methods for particulate flows, in *Computational Science for the 21st Century*, edited by M. O. Bristeau, G. J. Etgen, W. Fitzgibbon, J. L. Lions, J. Périaux, and M. F. Wheeler (Wiley, Chichester, 1997), pp. 270–279.
3. R. Glowinski, T. W. Pan, T. I. Hesla, D. D. Joseph, and J. Periaux, A fictitious domain method with distributed Lagrange multipliers for the numerical simulation of particulate flow, in *Domain Decomposition Methods 10*, edited by J. Mandel, C. Farhat, and X. C. Cai (AMS, Providence, RI, 1998), pp. 121–137.
4. T. W. Pan, R. Glowinski, T. I. Hesla, D. D. Joseph, and J. Periaux, Numerical simulation of the Rayleigh–Taylor instability for particulate flow, in *Proceedings of the Tenth International Conference on Finite Elements in Fluids, January 5–8, 1998, Tucson, Arizona*, edited by M. Hafez and J. C. Heinrich, pp. 217–222.
5. R. Glowinski, T. W. Pan, T. I. Hesla, and D. D. Joseph, A distributed Lagrange multiplier/fictitious domain method for particulate flow, *Int. J. Multiphase Flow* **25**(5), 755–794 (1999).
6. R. Glowinski, T. W. Pan, T. I. Hesla, D. D. Joseph, and J. Periaux, A distributed Lagrange multiplier/fictitious domain method for flows around moving rigid bodies: Application to particulate flow, *Int. J. Numer. Meth. Fluids* **30**, 1043–1066 (1999).
7. R. Glowinski, T. W. Pan, T. I. Hesla, D. D. Joseph, and J. Periaux, A distributed Lagrange multiplier/fictitious domain method for the simulation of flows around moving rigid bodies: Application to particulate flow, *Comp. Meth. Appl. Mech. Eng.* **184**, 241–267 (2000).
8. R. Glowinski, T. W. Pan, and D. D. Joseph, Fictitious domain methods for particulate flow in two and three dimensions, in *Proceedings of the International Conference on the Mathematics of Finite Elements and their Applications (MAFELAP 99)*, edited by J. R. Whiteman, in press.
9. B. Desjardins and M. J. Esteban, On weak solution for fluid–rigid structure interaction: Compressible and incompressible models, *Arch. Rational Mech. Anal.* **146**, 59–71 (1999).
10. H. H. Hu, Direct simulation of flows of solid–liquid mixtures, *Int. J. Multiphase Flow* **22**, 335–352 (1996).
11. A. Johnson and T. Tezduyar, 3-D simulation of fluid–particle interactions with the number of particles reaching 100, *Comp. Meth. Appl. Mech. Eng.* **145**, 301–321 (1997).
12. B. Maury and R. Glowinski, Fluid–particle flow: A symmetric formulation, *C. R. Acad. Sci. Paris* **324**(1), 1079–1084 (1997).
13. C. S. Peskin, Numerical analysis of blood flow in the heart, *J. Comput. Phys.* **25**, 220–252 (1977).
14. C. S. Peskin and D. M. McQueen, Modeling prosthetic heart valves for numerical analysis of blood flow in the heart, *J. Comput. Phys.* **37**, 113–132 (1980).
15. C. S. Peskin, Lectures on mathematical aspects of physiology, *Lect. Appl. Math.* **19**, 69–107 (1981).
16. A. L. Fogelson and C. S. Peskin, A fast numerical method for solving the three-dimensional Stokes equations in the presence of suspended particles, *J. Comput. Phys.* **79**, 50–69 (1988).
17. K. Hofler, M. Muller, S. Schwarzer, and B. Wachman, Interacting particle–liquid systems, in *High Performance Computing in Science and Engineering*, edited by E. Krause and W. Jager (Springer-Verlag, Berlin, 1998), pp. 54–64.
18. N. A. Patankar, P. Singh, D. D. Joseph, R. Glowinski, and T. W. Pan, A new formulation of the distributed Lagrange multiplier/fictitious domain method for particulate flows, *Int. J. Multiphase Flow* **26**, 1509–1524 (2000).
19. Y. Achdou and Y. Kuznetsov, Algorithms for the mortar element method, in *Domain Decomposition Methods in Sciences and Engineering*, edited by R. Glowinski, J. Periaux, Z.-C. Shi, and O. Widlund (Wiley, Chichester, 1997), pp. 33–42.
20. C. L. Brooks, M. Karplus, and B. M. Pettitt, *Proteins: A Theoretical Perspective of Dynamics, Structure, and Thermodynamics* (Wiley, New York, 1988).
21. N. Kikuchi and J. T. Oden, *Contact Problems in Elasticity: A Study of Variational Inequalities and Finite Element Methods* (SIAM, Philadelphia, 1988).

22. F. Bertrand, P. A. Tanguy, and F. Thibault, A three-dimensional fictitious domain method for incompressible fluid flow problem, *Int. J. Numer. Meth. Fluids* **25**, 719–736 (1997).
23. F. Brezzi and M. Fortin, *Mixed and Hybrid Finite Element Methods* (Springer-Verlag, New York, 1991).
24. J. E. Roberts and J. M. Thomas, Mixed and hybrid methods, in *Handbook of Numerical Analysis, Vol. II*, edited by P. G. Ciarlet and J. L. Lions (North-Holland, Amsterdam, 1991) pp. 523–639.
25. V. Girault, R. Glowinski, and T. W. Pan, A fictitious-domain method with Lagrange multipliers for the Stokes problem, in *Applied Nonlinear Analysis*, edited by A. Sequeira, H. B. de Veiga, and J. H. Videman (Kluwer Academic/Plenum, New York, 1999), pp. 159–174.
26. A. J. Chorin, A numerical method for solving incompressible viscous flow problems, *J. Comput. Phys.* **2**, 12–26 (1967).
27. A. J. Chorin, On the convergence of discrete approximation to the Navier–Stokes equations, *Math. Comp.* **23**, 341–353 (1968).
28. A. J. Chorin, Numerical study of slightly viscous flow, *J. Fluid Mech.* **57**, 785–796 (1973).
29. R. Glowinski and O. Pironneau, Finite element methods for Navier–Stokes equations, *Annu. Rev. Fluid Mech.* **24**, 167–204 (1992).
30. S. Turek, *Efficient Solvers for Incompressible Flow Problems: An Algorithmic and Computational Approach* (Springer-Verlag, Berlin, 1999).
31. G. I. Marchuk, Splitting and alternating direction methods, in *Handbook of Numerical Analysis, Vol. I*, edited by P. G. Ciarlet and J. L. Lions (North-Holland, Amsterdam, 1990), pp. 197–462.
32. J. T. Beale and A. Majda, Rates of convergence for viscous splitting of the Navier–Stokes equations, *Math. Comp.* **37**, 243–260 (1981).
33. E. J. Dean and R. Glowinski, A wave equation approach to the numerical solution of the Navier–Stokes equations for incompressible viscous flow, *C. R. Acad. Sci. Paris* **325**(1), 789–791 (1997).
34. E. J. Dean, R. Glowinski, and T. W. Pan, A wave equation approach to the numerical simulation of incompressible viscous fluid flow modeled by the Navier–Stokes equations, in *Mathematical and Numerical Aspects of Wave Propagation*, edited by J. A. De Santo (SIAM, Philadelphia, 1998), pp. 65–74.
35. M. Fortin and R. Glowinski, *Augmented Lagrangian Methods* (North-Holland, Amsterdam, 1983).
36. R. Glowinski and P. Le Tallec, *Augmented Lagrangians and Operator Splitting Methods in Nonlinear Mechanics* (SIAM, Philadelphia, 1989).
37. R. Glowinski, *Numerical Methods for Nonlinear Variational Problems* (Springer-Verlag, New York, 1984).
38. O. Pironneau, *Finite Element Methods for Fluids* (Wiley, Chichester, 1989).
39. P. Parthasarathy, *Application of a Wave-like Equation Method for Newtonian and Non-Newtonian Flows*, Master thesis (Department of Mechanical Engineering, University of Houston, Houston, Texas, 1999).
40. J. Martikainen, T. Rossi, and J. Toivanen, Application of algebraic fictitious domain methods for solving the generalized Stokes problem, in *Book of Abstracts of the Third European Conference on Numerical Mathematics and Advanced Applications (ENUMATH99), Jyväskylä, Finland, July 26–30, 1999*, p. 168.
41. L. Schwartz, *Théorie des Distributions* (Herman, Paris, 1966).
42. R. Clift, J. R. Grace, and M. E. Weber, *Bubbles, Drops, and Particles*, Academic Press, New York, 1978.
43. R. Glowinski, Finite element methods for the numerical simulation of incompressible viscous flow. Introduction to the control of the Navier–Stokes equations, in *Vortex Dynamics and Vortex Methods*, edited by C. R. Anderson and C. Greengard (Am. Math. Soc., Providence, RI, 1991), pp. 219–301.
44. T. W. Pan, Numerical simulation of the motion of a ball falling in an incompressible viscous fluid, *C. R. Acad. Sci. Paris* **327**(2,b), 1035–1038 (1999).
45. G. H. Golub and C. Van Loan, *Matrix Computations* (Johns Hopkins Univ. Press, Baltimore, 1996).
46. T. W. Pan, V. Sarin, R. Glowinski, A. Sameh, and J. Periaux, A fictitious domain method with Lagrange multipliers for the numerical solution of particular flow and its parallel implementation, in *Parallel Computational Fluid Dynamics: Development and Applications of Parallel Technology*, edited by C. A. Lin, A. Ecer, N. Satofuka, P. Fox, and J. Periaux (North-Holland, Amsterdam, 1999), pp. 467–474.
47. J. B. Ritz and J. P. Caltagirone, A numerical continuous model for the hydrodynamics of fluid particle systems, *Int. J. Numer. Meth. Fluids* **30**, 1067–1090 (1999).

48. J. Feng, H. H. Hu, and D. D. Joseph, Direct simulation of initial value problems for the motion of solid bodies in a Newtonian fluid. 1. Sedimentation, *J. Fluid Mech.* **261**, 95–134 (1994).
49. A. F. Fortes, D. D. Joseph, and T. S. Lundgren, Nonlinear mechanics of fluidization of beds of spherical particles, *J. Fluid Mech.* **177**, 467–483 (1987).
50. R. R. Huilgol and N. Phan-Thien, *Fluid Mechanics of Viscoelasticity* (Elsevier, Amsterdam, 1997).
51. D. D. Joseph, *Fluid Dynamics of Viscoelastic Liquids* (Springer-Verlag, New York, 1990).
52. D. D. Joseph and Y. J. Liu, Orientation of long bodies falling in a viscoelastic liquid, *J. Rheology* **37**, 961–983 (1993).
53. H. H. Hu, D. D. Joseph, and A. F. Fortes, Experiments and direct simulation of fluid particle motions, *Int. Vid. J. Eng. Res.* **2**, 17 (1997).
54. D. P. Young, R. G. Melvin, M. B. Bieterman, F. T. Johnson, S. S. Samanth, and J. E. Bussioletti, A locally refined finite rectangular grid finite element method. Application to computational physics, *J. Comput. Phys.* **92**, 1–66 (1991).
55. M. C. Roco, *Particulate Two-Phase Flow* (Butterworth-Heinemann, Boston, 1993).